BONNER METEOROLOGISCHE ABHANDLUNGEN

Heft 84 (2018) (ISSN 0006-7156)
Herausgeber: Andreas Hense

Yen-Sen Lu

PROPAGATION OF LAND SURFACE MODEL UNCERTAINTIES IN SIMULATED TERRESTRIAL SYSTEM STATES

BONNER METEOROLOGISCHE ABHANDLUNGEN

Heft 84 (2018) (ISSN 0006-7156)
Herausgeber: Andreas Hense

Yen-Sen Lu

PROPAGATION OF LAND SURFACE MODEL UNCERTAINTIES IN SIMULATED TERRESTRIAL SYSTEM STATES

Propagation of land surface model uncertainties in simulated terrestrial system states

Dissertation
zur
Erlangung des Doktorgrades (Dr. rer. nat.)
der
Mathematisch-Naturwissenschaftlichen Fakultät
der
Rheinischen Friedrich-Wilhelms-Universität Bonn

vorgelegt von
Yen-Sen Lu
aus
Kaohsiung, Taiwan

Bonn, November, 2017

Diese Arbeit ist die ungekürzte Fassung einer der Mathematisch-Naturwissenschaftlichen Fakultät der Rheinischen Friedrich-Wilhelms-Universität Bonn im Jahr 2017 vorgelegten Dissertation von Yen-Sen Lu aus Kaohsiung, Taiwan.

This paper is the unabridged version of a dissertation thesis submitted by Yen-Sen Lu born in Kaohsiung, Taiwan to the Faculty of Mathematical and Natural Sciences of the Rheinische Friedrich-Wilhelms-Universität Bonn in 2017.

Anschrift des Verfassers: Address of the author:

Yen-Sen Lu
Meteorologisches Institut der
Universität Bonn
Auf dem Hügel 20
D-53121 Bonn

1. Gutachter: Prof. Dr. Clemens Simmer, Rheinische Friedrich-Wilhelms-Universität Bonn
2. Gutachter: Prof. Dr. Matthias Langensiepen, Rheinische Friedrich-Wilhelms-Universität Bonn

Tag der Promotion: 25. Apri 2018

Zusammenfassung

Diese Studie zeigt, wie sich Unsicherheiten in der Parametrisierung der Vegetation auf die Simulation des Erdsystems auf der regionalen Skala auswirken, und wie man diese Unsicherheiten reduzieren kann. In den üblichen Parametrisierungen werden unterschiedliche Gleichungen für die Transpirationsleitfähigkeit von Blättern sowie unterschiedliche Produkte für den Blattflächenindex (leaf area index, LAI) verwendet. Zunächst bestimmen wir die Effekte dieser Unsicherheiten auf den Zustand und die Austauschflüsse an der Landoberfläche und erweitern diese Untersuchung dann auf den Untergrund mit einem Schwerpunkt auf der Berechnug der Grundwasserhöhe.

Im ersten Teil der Studie benutzen wir das Landoberflächenmodell CLM3.5, während wir für den zweiten Teil das gekoppelte Modell ParFlow-CLM3.5 verwenden. Um die Unsicherheiten zu quantifizieren, wurden zwei Simulationen mit jeweils drei unterschiedlichen Gleichungen für die Transpirationsleitfähigkeit und zwei verschiedenen LAI Produkten durchgeführt. Die drei Gleichungen für den Transpirationsleitfähigkeit folgen dem Jarvis-Stewart Typ, dem Ball-Berry-Collatz Typ sowie dem Ball-Berry-Leuning Typ, wohingegen eines der LAI Produkte auf den MODIS LAI zurückgreift, während das andere ein einfacher dynamischer LAI ist, der von der Bodentemperatur abhängt. Die Simulationen mit CLM3.5 sind angetrieben durch meteorologische Randbedingungen für die Jahre 2012 und 2013, welche mit Beobachtungen von vier Messstellen im Rur Einzugsgebiet verglichen werden. Von den Messstellen ist eine mit Gras bewachsen, zwei sind bewirtschaftetes Ackerland und eine liegt in einem Waldgebiet. Die Simulationen mit dem gekoppelten ParFlow-CLM3.5 Modell sind für das gesamte Rur Einzugsgebiet ausgeführt worden, angetrieben von 2-D Reanalysedaten.

Die Ergebnisse der CLM3.5 Simulationen zeigen, dass die Transpiration der Vegetation, eine Kombination aus LAI und Transpirationsleitfähigkeit, den entscheidenden Faktor für die Fortpflanzung von Unsicherheiten in einem Landoberflächenmodell darstellt. Für den Fall, dass eine Ball-Berry Typ Gleichung benutzt wird, kann eine Aktualisierung der physiologischen Parameter die Simulationen im Vergleich zu Messungen verbessern. Generell funktioniert die Simulation gut für die Grasland Messstelle, während die Messstellen des Ackerlandes durch

die Bewirtschaftung und die des Waldes durch die Struktur der Baumkronen maßgeblich beeinflusst werden. Während sowohl die Wahl des LAI Produktes als auch der Typ der Gleichung für die Transpirationsleitfähigkeit große Auswirkungen auf das Ergebnis des Landoberflächenmodells haben, ist der Einfluss des LAI insgesamt geringer als der der Transpirationsleitfähigkeit. Der Jarvis-Stewart Typ zeigt die besten Ergebnisse in Bezug auf den latenten Wärmefluss, jedoch nicht bei allen Wetterlagen. Keine der Typen funktioniert zufriedenstellend für den sensiblen Wärmefluss. Sowohl der Jarwis-Stewart Typ als auch der Ball-Berry Typ nähern sich der Realität auf verschiedene Weisen mit unterschiedlichen Qualitäten an. Anstelle zu entscheiden, welches die beste Lösung ist, untersuchen wir wie wir den Beobachtungen näher kommen können indem wir Parameter und physiologische Mechanismen verbessern.

Durch die Ergebnisse mit Parflow-CLM3.5 wird klar, dass die Wasserverfügbarkeit, eine Kombination aus Bodenfeuchte und Wurzelverteilung, der hauptsächliche Faktor für Unsicherheiten der Vegetationsreaktion in Bezug auf den Untergrund und auch der Landoberfläche ist. Für das Jahr 2012 war das Rur Einzugsgebiet nicht durch die Wasserverfügbarkeit limitiert, was bedeutet, dass die Wärmeflüsse nicht vom Grundwasserspiegel abhingen. Im Jahr 2013 jedoch herrschte eine limitierte Wasserverfügbarkeit, sodass je nach Grundwasserspiegel unterschiedliche Wärmeflüsse auftraten. Diese Unterschiede waren besonders ausgeprägt für Simulationen, die den Jarvis-Stewart Typ benutzen.

Abstract

This study demonstrates how vegetation uncertainty propagates in the terrestrial system and how to reduce this uncertainty. Different stomatal conductance equations and different leaf area index input exist for solving vegetation response to land-atmospheric interactions. We investigate the effect of vegetation uncertainty on land surface firstly, and then the extension of this uncertainty to subsurface is studied.

We employ a land surface model, CLM3.5, and the coupled model, Parflow-CLM3.5, in the first and the second part of study, respectively. To quantify the uncertainty, we perform simulations with three stomatal conductance equations and the two leaf area index (LAI) input types. The three stomatal conductance equations include the Jarvis-Stewart type, the Ball-Berry-Collatz type, and the Ball-Berry-Leuning type, and the two LAI input types include the MODIS LAI and the simple dynamic LAI based on ground temperature. The simulations of CLM3.5 are driven with observed meteorological forcing data for the years 2012 and 2013, and are compared against observation at four vegetated sites in the Rur Catchment, which includes a grassland, two croplands, and a forest sites. The simulations of the coupled model Parflow-CLM3.5 are performed over the whole Rur Catchment with 2-D reanalysed weather forcing data.

The results by CLM3.5 indicate that canopy conductance, which combines stomatal conductance and LAI, is the key of vegetation uncertainty propagation in the land surface model. The employment of updated physiological parameters can improve the simulations by the Ball-Berry type stomatal conductance equations. In the four sites, the simulations are well performed at the grass site, but are interrupted by crop management and canopy structure at the crop sites and the forest site, respectively. Both stomatal conductance equations and LAI input types affect the calculation of land surface model significantly, but the stomatal conductance equations have more impact on the land surface model than LAI. The Jarvis-Stewart type performs the simulated latent heat flux better but not under all the weather conditions. However, none of the types performs simulated sensible heat flux the best. We regard the Jarvis-Stewart type and the Ball-Berry type as two types of approach, which can

both approach the real world well. Instead of judging which is the best equation, we shall investigate how to approach the real world by improving the parameterization and the physiological mechanism.

From the results by Parflow-CLM3.5, we demonstrate that the soil water limitation factor, which combines soil moisture and root distribution, is the key propagating vegetation uncertainty to the subsurface and then to the surface. The Rur Catchment is determined by the soil water limitation factor as water-unlimited condition in the year 2012 and thus the heat flux does not change with the water table depth. In the year 2013, the Rur Catchment is in a water-limited condition, and thus the heat fluxes are affected by the water table depth. The simulations by the Jarvis-Stewart type show a stronger relation of heat fluxes with water table depth between soil water-unlimited and the soil water-limited condition.

摘要

本研究展示植物的不確定性如何在地球系統中傳遞，以及如何減少此不確定性。目前有不同的植物氣孔導度方程式以及不同的葉面積指數(LAI)，借以解釋植物對地氣交互作用的反應。本研究會先探討植物不確定性對地表的影響，再探討此不確定性延申至地底的影響。

本研究分兩部份的模擬，第一部份使用地表模式 CLM3.5，第二部分使用耦合模型 Parflow-CLM3.5。為了量化不確定性，本研究使用三種不同的氣孔導度方程式以及兩種葉面積指數的輸入方式，用以進行模擬。三種氣孔導度方程式分別為 Jarvis-Stewart 方法，Ball-Berry-Collatz 方法，和 Ball-Berry-Leuning 方法。兩種葉面積指數輸入分別是 MODIS 探測器中的 LAI 資訊，與利用地層溫度的葉面積指數參數化公式(simple dynamic LAI)。CLM3.5的模擬使用在德國魯爾河(Rur，馬士河支流)流域於2012與2013量測的氣象資料，其中包括四站含植披的觀測點：一座草原、二座農地，以及一座森林。模擬的地表模式結果會與觀測值進行比較分析。耦合模型 Parflow-CLM3.5使用二維的再分析氣象資料，以模擬整個魯赫河流域。

經由 CLM3.5的結果，本研究指出結合植物氣孔導度與葉面積指數的樹冠層導度，是傳遞植物不確定性到地表行為的關鍵指數。使用進階的植物生理參數，可以提升植物氣孔傳導公式中，Ball-Berry 方法的模擬結果。在四站觀測點中，草原的模擬結果最佳，農地的模擬結果受農作行為擾動，而森林的模擬結果則受到樹冠結構的影響。

植物氣孔導度與葉面積指數都影響地表模式甚巨，而植物氣孔導度的影響更甚。Jarvis-Stewart 方法對潛熱通量的模擬結果較好，但非在所有的氣候條件下。然而，任何方法都無法最佳地模擬顯熱通量。本研究指出無論是 Jarvis-Stewart 或是 Ball-Berry 方法，都可用以模擬真實狀況。所以理應研究如何改善兩者的參數化方法或是生理機制，而非比較孰優孰劣。

經由 Parflow-CLM3.5的結果，本研究指出結合土壤濕度與根系分佈的土水限制參數，是植物不確定性傳遞至地底，再傳遞至地表的關鍵參數。魯爾河流域在2012年時，被土水限制參數判定處於濕度無限狀態，所以潛熱通量並不隨地下水位變化。在2013時，魯赫河流域處於濕度限制狀態，因此潛熱通量受地下水位影響。經 Jarvis-Stewart 方法的模擬結果顯示出，在土壤濕度限制與無限制的區間，地表熱通量與地下水位間有顯著的關係。

Dedicated to

Rui

Xu

Wen-Fei

上善若水 – 《道德經》

"The highest excellence is like that of water", Lao Tzu

Contents

Chapter 1

Introduction

Land-atmosphere interactions are important processes, which need to be included in climate and weather forecast models. The extreme heterogeneity of the land and in particular its surface makes it, however, impossible to simulate these processes following first principles. Accordingly, the relevant processes are parameterized following rather mechanistic approaches, which can only be rough approximations to the real acting processes. Over the past decades, however, these parameterizations have evolved considerably into quite comprehensive so-called land surface models (LSMs) and became prominent components in climate and weather forecast models. Different assumptions and approximations approaching the true processes have led to several different LSMs with their own strengths and weaknesses. Ensuing errors or shortcomings of the different models will result in different results e.g. for the exchange of heat energy, water vapor, and momentum, which will also be reflected in the atmospheric circulation propagate in the coupled system. It is the goal of this thesis to quantify these effects for a set of LSM components. In the following, we will introduce as a background to this study the general concepts of LSMs.

1.1 Concept of constructing a land surface model

As shown in **Figure 1.1**, a land surface model (i.e. LSM) includes several concepts to describe the real world. Each concept for a specific phenomenon is established by a scheme. For example, the hydrological scheme is used to describe the water exchange between atmosphere and land surface, and the radiative transfer scheme within the LSM is designed to describe the radiation exchange between atmosphere and land surface. A scheme can be formed by several sub-schemes. For example, the hydrological scheme consists of two sub-

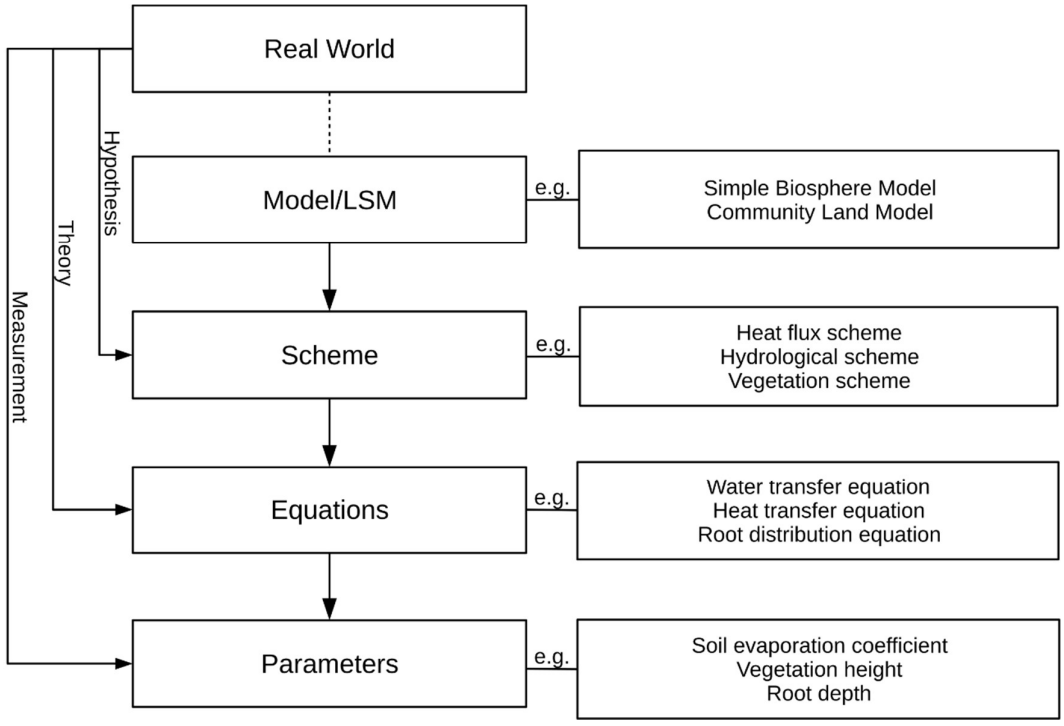

Figure 1.1. Concepts of building a model.

schemes, the water movement scheme and vegetation interception scheme. Each scheme is constructed by a set of equations based on different theories. For instance, a soil-water retention scheme is described as a function of water saturation and soil void size. Because most equations are empirical, so they contain parameters often determined from measurements. From the model design to the parameter choice, all steps lead to differences between different LSMs.

Sellers *et al*. (1997) classify LSMs into three generations by their complexity. The first generation LSM is proposed by Manabe (1969) and consists of i) the exchange of radiation between atmosphere and land surface (radiative transfer scheme), ii) the heat transport by water evaporation and temperature gradient (heat fluxes scheme), and iii) the soil water balance on the land surface (hydrological scheme) . By the inclusion of a first generation LSM into a global circulation model, researchers can capture the spatial distribution of rainfall in the mid-latitudes so that the simulations better agree with the observations. However, there is no vegetation cover and physiological behaviour (vegetation scheme) in the Manabe (1969) model. Vegetation does, however, play an important role in solar radiation interception and

local convection (Shukla & Mintz, 1982). Furthermore, the soil water movement is simplified by a "bucket model", which takes only rainfall rate and evaporation into account within a 15 cm depth of soil column. Soil moisture plays an important role in the land-atmospheric interaction, e.g. by influencing local convection (Garrett, 1982). Overall, the first generation LSMs lack a vegetation scheme and a sufficiently detailed hydrological scheme.

Based on the structure of the first generation model (Manabe, 1969), the second generation LSMs employ a physically-based hydrological and vegetation scheme (e.g. SiB (Sellers *et al.*, 1996), BATS (Dickinson *et al.*, 1993), VIC (Liang *et al.*, 1994) and LSX (Pollard & Thompson, 1995). The abbreviation of LSMs can be found in Appendix I). The hydrological scheme features a soil water movement equation instead of a "bucket model", better simulates soil moisture compared to observed soil moisture (e.g. the VIC LSM (Shao & Henderson-Sellers, 1996)). Vegetation scheme includes evaporation from leaf surfaces, water storage in the canopy, and the physiological behaviour of vegetation (transpiration). Transpiration controls not only water vapor and carbon dioxide exchange by stomata (the micro scale pores on leaves) but also the soil water extraction by roots. Vegetation schemes generally include three sub-schemes: root distribution scheme, stomatal conductance scheme, and leaf area index (LAI) scheme. Root distribution scheme is used to estimate the water uptake from the soil at the depth of root. Stomatal conductance schemes incorporate environmental factors to predict gas conductance through stomata. The LAI is used to estimate the leaf coverage of the land surface for scaling up the physical processes from the leaf scale (cm) to the canopy scale (m). By the implementation of a vegetation scheme, second generation LSMs can simulate local heat fluxes under specific land cover conditions (Shao & Henderson-Sellers, 1996). These second generation LSMs improve the heat fluxes, but the bio-geo-chemical interaction (e.g. the interaction between carbon dioxide and respiration) is not included.

The third generation LSMs (e.g. JULES (Best *et al.*, 2011), CABLE (Kowalczyk *et al.*, 2006), CoLM (Dai *et al.*, 2003), and Noah LSM(Ek *et al.*, 2003)) include the carbon cycle to simulate the exchange of carbon dioxide between atmosphere and land surface by bio-geo-chemical interaction. The carbon cycle includes photosynthesis (physiological scheme) and soil respiration (bio-geo-chemical scheme). The physiological schemes describe carbon fixation by plants while the physiological and bio-geo-chemical schemes describe carbon emission into the atmosphere. Most LSMs employ only physiological schemes to describe the carbon cycle,

some employ both. The incorporation of the carbon cycle allows to address climate change caused by increasing carbon dioxide (e.g. Berg *et al*. (2016)). Moreover, some of the third generation LSMs, e.g. CoLM, SHE (Abbott *et al.*, 1986), SiB2 (Sellers *et al.*, 1996), and Noah LSMs include a three dimensional groundwater model to provide realistic groundwater processes (e.g. McMichael *et al.*, 2006; Kollet & Maxwell, 2008; Jiang *et al.*, 2009; Tian *et al.*, 2012). By coupling with the groundwater, the interaction between atmosphere and subsurface is simulated more realistically.

A scheme describes the concept of physical processes in the real world and must be cast into equations to perform calculations. As shown in **Figure 1.1**, an equation is derived by a theory, which is built from the real world. For instance, the stomatal conductance scheme describes the relationship between stomatal conductance and the environmental factors e.g. absorbed light, humidity, carbon dioxide concentration, and soil moisture. Different theories propose different equations to realize the physical concept of a stomatal conductance scheme, such as the Jarvis' equation (1976), Ball-Woodrow-Berry's equation (1987), and Leuning's equation (1995).

Most equations are empirical; thus they contain parameters estimated from experimental data. Equations with different parameters result in different simulations. For example, the Ball-Woodrow-Berry's equation (1987) of stomatal conductance describes stomatal conductance as a function of the minimum stomatal conductance affected by the net carbon dioxide assimilation rate, the carbon dioxide concentration on the leaf, and the relative humidity. The minimum stomatal conductance can be different for different plant types (Lin *et al.*, 2015).

1.2 The complexity and uncertainty of models, schemes, and equations

A model is established by several schemes, and a scheme can be described by different equations, which are affected by different parameters. The more schemes a model employs, the higher its potential to approach to the processes in the real world. But the number of schemes is limited by computational resources and observations and/or theories required to adapt the schemes. Also different equations might be proposed to describe the same physical concept. Moreover, parameters may vary from place to place (e.g. different geography and different climate) and between plant types and soil types, which also might lead to different

opinions on and decisions for the use of certain schemes, equations, and parameters. It is important and necessary to clarify the uncertainty of the schemes, equations, and parameters.

Many LSMs are proposed since 1969, and many comparison studies are reported (Pitman *et al.*, 1999; Boone *et al.*, 2004; Best *et al.*, 2015). According to a recent comparison study (Best *et al.*, 2015), different LSMs have different advantages related to different aspects. The Manabe LSM consists of only three schemes, which are radiative transfer scheme, heat flux scheme, and hydrological scheme. CLM-CN consists of six schemes, which are radiative transfer scheme, heat flux scheme, hydrological scheme, vegetation scheme, urban scheme, and nitrogen cycle scheme (Thornton & Rosenbloom, 2005). The numbers and types of employed schemes vary due to the different approaches to the real land-atmosphere interaction. Some schemes are mature and already quite unified among LSMs (e.g. radiative transfer scheme and hydrological scheme) while others are still evolving (e.g. nitrogen cycle scheme and urban scheme). Available computational and consumption resources might limit the employment of schemes (e.g. three-dimensional hydrological scheme and dynamic vegetation scheme). Nevertheless, most sophisticated LSMs are consisted of at least radiative transfer scheme, heat flux scheme, hydrological scheme, and vegetation scheme, which are discussed in the following section.

The radiative transfer and heat flux schemes are two basic and mature schemes. In recent studies (Oleson *et al.*, 2004a; Niu *et al.*, 2011; Best *et al.*, 2011), radiative transfer schemes mainly use the two-stream radiation equations (Dickinson, 1983), and the heat flux scheme mainly adopts the equation based on similarity theory (Monin & Obukhov, 1954). In general, researchers agree on the equations employed in these two schemes. In hydrological schemes, Richards' Equation describes the soil water movement under saturated and unsaturated conditions. However, for one of the parameters in the Richards' equation, the relative hydraulic conductivity, three different soil-water retention fitting curves are proposed (Clapp & Hornberger, 1978; van Genuchten, 1980; Cosby *et al.*, 1984). Though the fitting curve proposed by Clapp & Hornberger (1978) can be calculated easily, the one proposed by van Genuchten approaches the physical processes better (Cuenca *et al.*, 1996). Radiative transfer schemes, heat flux schemes, and hydrological schemes are formulated via equations with less uncertainty, and hence studies focus on the sensitivity of their parameters to land-atmosphere interactions (Rosero *et al.*, 2009; Schwinger *et al.*, 2010; Hou *et al.*, 2012; Mai *et al.*, 2015;

Jefferson *et al.*, 2015; Cuntz *et al.*, 2016).

The radiative transfer, heat flux, and hydrological schemes follow physical concepts like energy and mass conservation, but vegetation schemes do not. As shown in **Figure 1.2** , a plant responds to environment and climate in complex ways, and hence vegetation phenology cannot be easily approached. For example, usually the vegetation height and plant leaves grow with time, but they are defined as constants in most LSMs. The roots extend or shrink, but are also regarded static in most of the current LSMs. These simulated processes do not follow the physiological behaviour of plants because the real physiological processes are difficult to approach. The complexity of physiology is difficult to formalize in schemes; hence any improvement is important.

Vegetation schemes consists of many sub-schemes such as LAI (description of leaf biomass), vegetation height (description of stem biomass), root distribution (description of root biomass), and physiological behaviours, such as photosynthesis (description of H_2O and CO_2 gas exchange) and stomatal conductance (description of gas exchange through stomatal opening). Some vegetation schemes consist of only one sub-scheme, the stomatal conductance scheme (Pollard & Thompson, 1995) while others consist of five sub-schemes (LAI, root distribution, photosynthesis, nitrogen cycle, and stomatal conductance scheme) to describe the complex interactions between vegetation, hydrological, and energy cycle (Thornton & Rosenbloom, 2005). The choice of vegetation sub-scheme depends on the scheme stability and available computational resources. The three widely accepted vegetation sub-schemes include stomatal conductance, LAI, and root distribution. According to recent studies, the accuracy of vegetation schemes is mainly controlled by the quality of the stomatal conductance and LAI sub-schemes (Martin, 1993; Arora, 2002; Pitman, 2003).

Stomatal conductance schemes control the water vapor loss through the stomatal opening (Hetherington & Woodward, 2003). As shown in **Figure 1.2**, stomata release water and heat into the atmosphere (transpiration). And thus stomata are regarded as the conductors of water and heat from vegetation into the atmosphere and an important component for discussing land-atmospheric interactions (Beerling, 2015). The stomata opening is controlled by environmental factors, such as radiation, vapor pressure, temperature, and carbon dioxide assimilation rate (photosynthesis). However, researchers have different opinions on how stomatal opening is affected by these factors and which factors should be considered. More

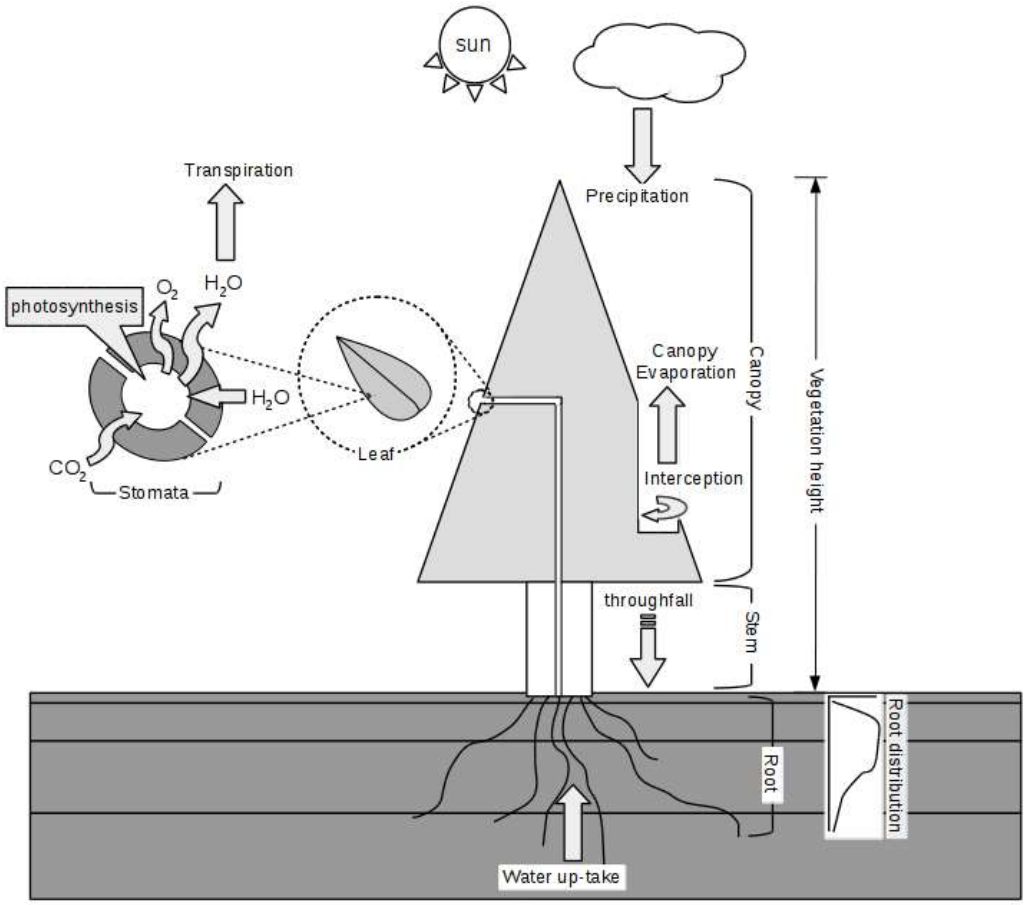

Figure 1.2. Vegetation scheme.

than forty stomatal conductance equations are proposed (Damour *et al.*, 2010). A simple stomatal conductance scheme considers only photosynthetic active radiation (PAR) (Langensiepen *et al.*, 2009) while more complete schemes include photosynthesis, relative humidity, carbon dioxide concentration, soil moisture stress, and leaf water potential (Bonan *et al.*, 2014). Two major types of stomatal conductance schemes - the Jarvis-type (J-type) and the Ball-Woodrow-Berry-type (BB-type) are mainly applied in LSMs. The J-type is a multiplicative equation, which uses environmental factors as stress functions containing empirical parameters. The BB-type accounts for effects of photosynthesis governed by gas exchange, soil moisture, and physiological reaction. These two sub-scheme types compete in the current literature, and a theoretical discussion of stomatal conductance equations is reviewed following the theory section (Section 2.4.1).

LAI quantifies the leaf coverage of the land surface and impacts radiative transfer (e.g. albedo), heat flux (e.g. transpiration and heat fluxes from leaves), and hydrology (e.g. interception of precipitation) (e.g. Rosero *et al.*, 2009; Schwinger *et al.*, 2010; Jefferson *et al.*, 2015). LAI is firstly acquired in situ and directly set as a parameter in LSMs (Running *et al.*, 1989; Shao & Henderson-Sellers, 1996). However, the on-site measured LAI values are not available on continental or global scales. Thus LAI parameterizations exist based on different hypotheses (Haxeltine *et al.*, 1996; Dickinson *et al.*, 1998; Ewert, 2004; Jiang *et al.*, 2009). Nowadays satellite measurements provide global LAI estimates at 1 km resolution about every 8 days, which are used in many LSMs (Oleson *et al.*, 2004a; Niu *et al.*, 2011). But LAI estimates from satellites have limitations. Firstly, LAI is often underestimated during winter time (Tian *et al.*, 2004; Lawrence & Chase, 2007) due to snow and cloud cover. Secondly, satellite measurements are limited by the signal saturation with increasing LAI (Brut *et al.*, 2009). Thirdly, a 1 km resolution might be not enough considering the land surface inhomogeneity. Thus simple LAI schemes and satellite-based LAI estimates are mostly used in LSMs (Levis *et al.*, 2004; Clark *et al.*, 2011; Cai *et al.*, 2014).

1.3 Coupling of LSM and groundwater model

Groundwater models calculate the surface flow on the land surface and the groundwater flow in the subsurface via continuity equations in the saturated and unsaturated zones (**Figure 1.3**). The saturated zone is where soil water fills the whole pores of soil; then water movement is driven by the hydraulic potential. The water flow in the unsaturated zone is described by soil water retention and driven by capillary forces which supply soil water from water table to the unsaturated zone (Kollet & Maxwell, 2008; Lam *et al.*, 2011; Tian *et al.*, 2012). When the water table depth is low enough to provide unlimited soil water for evaporation and transpiration, the exchange is only limited by available energy (energy limited zone, **Figure 1.3**). A water-limited zone is given, when the water table depth is deep enough to limit the provision of water from deeper layers for evaporation and transpiration at the surface. Accordingly, along valley slopes a transition zone exists between the energy limited zone in the valley and the water-limited zone on the hill-top; in between heat fluxes change with water table depth (e.g. Kollet & Maxwell, 2008).

The complex groundwater flow can be captured by a 3D groundwater model and only

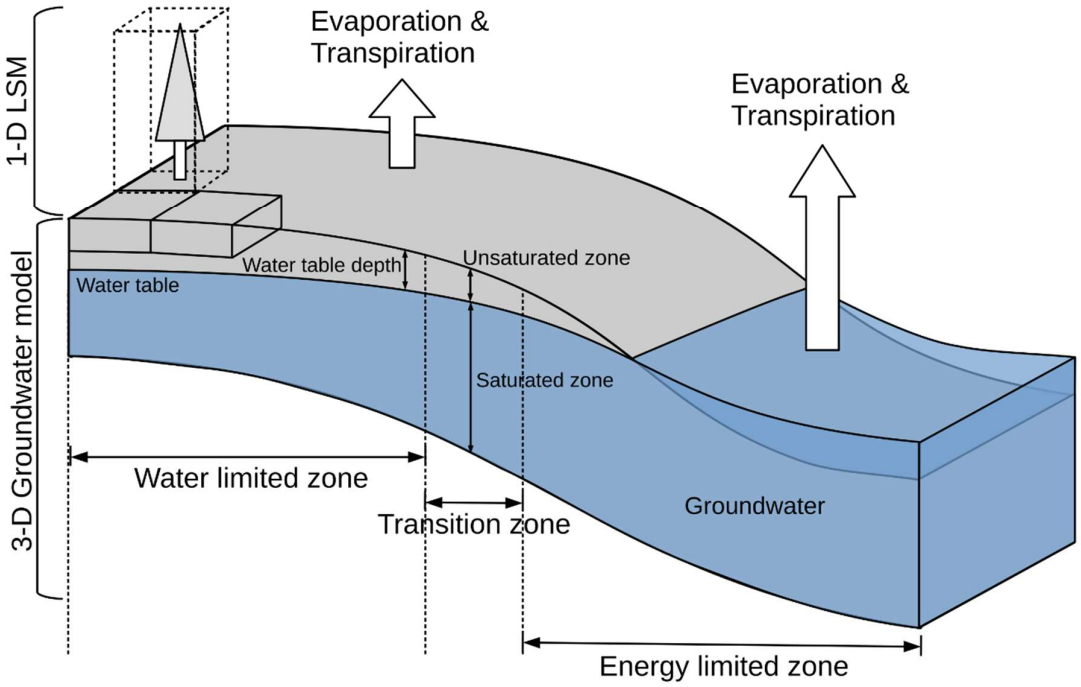

Figure 1.3. Groundwater model and coupling with LSM.

approximated by one-dimensional LSMs, which strongly simplify soil water movement. 3D-groundwater models can, however, be coupled to LSM to provide improved hydrological states of the subsurface ,(Maxwell & Condon, 2016). Since groundwater indirectly impacts precipitation (York *et al.*, 2002) and the atmospheric boundary layer development (Liang *et al.*, 1994; York *et al.*, 2002) a more realistic 3D groundwater model potentially increases the realism of the simulated terrestrial system.

1.4 Motivation and organization of the thesis

To clarify how vegetation scheme affects related land surface processes, including heat flux schemes and hydrological schemes, we simulate the heat and moisture fluxes by the LSM CLM3.5. The first part of this thesis describes uncertainties of vegetation schemes. The two vegetation sub-schemes, stomatal conductance and LAI, are considered as the main source of uncertainty. Three stomatal conductance equations, Ball-Berry-Collatz equation (Collatz *et al.*, 1991), Ball-Berry-Leuning equation (Leuning, 1995), and Jarvis-Stewart equation (Stewart,

1988), are compared. Two sets of physiological parameters are employed to understand the effect of physiological parameters on LSMs. To investigate LAI uncertainty, a simple LAI scheme is employed and compared against LAI from satellite measurement. All these schemes are implemented in the CLM (Community Land Model) LSM and simulation results are validated against observations. This study investigates which vegetation scheme can better perform in a LSM and under which conditions.

The second part of this thesis demonstrates how the uncertainty of the vegetation schemes propagates to the groundwater. Hydrological and vegetation schemes are affected by the hydrological state of the subsurface, which affects evaporation and transpiration on the land surface which both consume energy for vaporizing water. Hence, groundwater plays an important role in the subsurface-land-atmosphere interactions with two-way feedbacks between groundwater and heat fluxes.

Chapter 1 introduces the concept of LSMs and its complexity and uncertainty and motivates the analysis of uncertainties caused by components of the vegetation scheme and its feedback on groundwater flow addressed in this thesis. Chapter 2 summarizes the concepts and the theories employed in radiative transfer, heat flux, hydrological, and vegetation schemes. The stomatal conductance schemes and the LAI schemes are described in more detail as are the concept and equations of the groundwater model. Chapter 3 describes the methods and materials required to setup the LSM simulations coupled to a 1D and a 3D ground water model in this study. The first part of Chapter 3 introduces the modelling platform TerrSysMP, and in particular its components, CLM3.5 and Parflow. Two stomatal conductance schemes and a LAI scheme are explained detail, which are implemented in CLM3.5 to study their behaviour. The second part of Chapter 3 introduces the index of agreement and the Taylor diagram, which are used in this thesis to evaluate the accuracy of simulations. The third part of chapter 3 introduces the observational data required and used for the simulations. Chapter 4 presents the results concerning the vegetation scheme uncertainties in land-atmosphere interaction by the comparison of simulation results against observations. Chapter 5 presents the results of the uncertainty propagation from the vegetation schemes to subsurface-land-atmosphere interactions. Chapter 6 concludes the results of this study, and gives recommendations for future studies.

Chapter 2

The schemes in LSMs and groundwater models

The concepts and theories of four core schemes in LSMs, radiation transfer scheme, heat flux scheme, hydrological scheme, and vegetation scheme, are described from section 2.1 to Section 2.4. The vegetation sub-schemes, stomatal conductance and LAI, the impacts of which on the exchange processes are studied in this thesis, are introduced in section 2.4.1 and 2.4.2, respectively. Section 2.5 describes the concept of groundwater flow and its connection to the LSM.

2.1 Radiative transfer scheme

In the earth system, sun is the by far largest source of energy which provides the incoming shortwave radiation (incident solar radiation, $R_{sw,in}$, W m^{-2}). As shown in **Figure 2.1 (a)**, when the solar radiation reaches ground surface, $R_{sw,in}$ is partially reflected (albedo, α) as outgoing shortwave radiation ($R_{sw,out}$, W m^{-2}). Another part of the solar radiation is absorbed in the atmosphere and then partly emitted as longwave radiation towards the land surface ($R_{lw,in}$, W m^{-2}). The absorbed longwave and shortwave radiation increases the temperature of the land surface which emits longwave radiation ($R_{lw,out}$, W m^{-2}). The energy absorbed by the surface is called net radiation (R_{net}, W m^{-2}):

$$R_{net} = R_{sw,in} - R_{sw,out} + R_{lw,in} - R_{lw,out} \quad (2.1)$$

$$R_{net} = (1 - \alpha)R_{sw,in} + R_{lw,in} - R_{lw,out} \quad (2.2)$$

Based on the Stefan-Boltzmann constant (σ, W m^{-2} K^{-4}), the emission of longwave radiation follows:

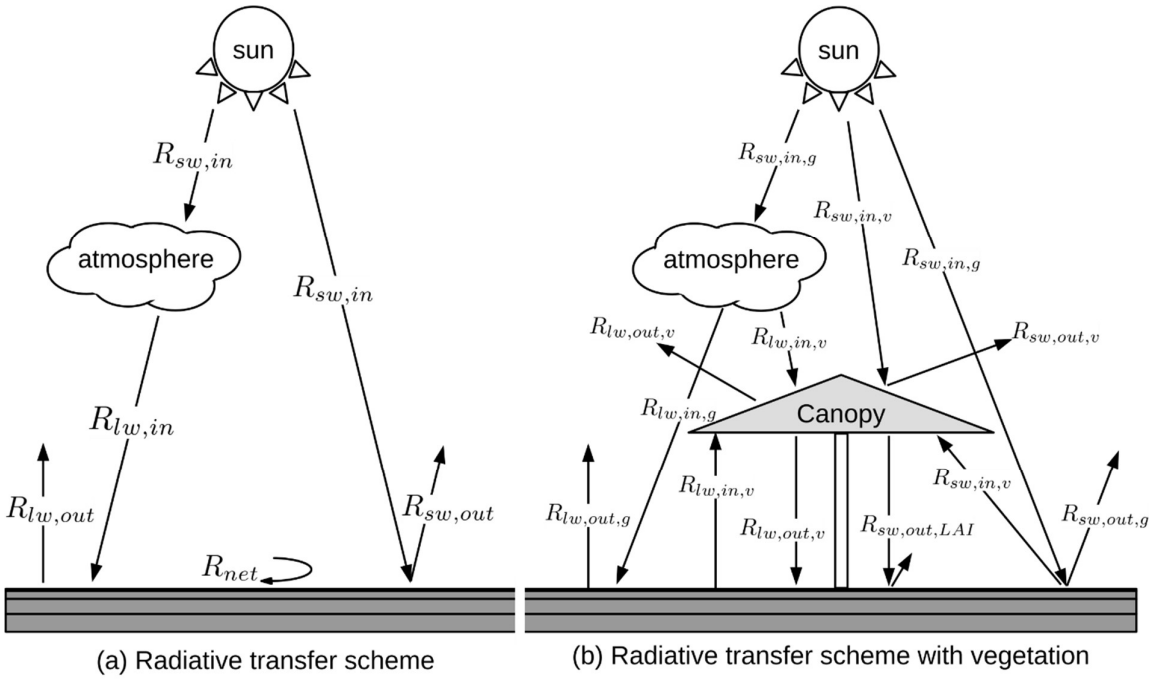

Figure 2.1. schematic of radiative transfer scheme (a) without vegetation and (b) with vegetation.

$$R_{lw,out} = \varepsilon\sigma {T_s}^4 \tag{2.3}$$

with surface emissivity ε (unitless) and surface temperature T_s (K). When the surface temperature increases, more longwave radiation emits to the atmosphere. Then the net radiation can be written as:

$$R_{net} = (1 - \alpha)R_{sw,in} + R_{lw,in} - \varepsilon\sigma {T_s}^4 \tag{2.4}$$

The radiative transfer scheme describes the path of radiation from the atmosphere to the surface, composed of soil and leaf surface.

When the vegetative canopy is considered, the interaction between vegetation and radiation becomes complex, as shown in **Figure 2.1 (b)**. The incoming shortwave radiation $R_{sw,in}$ is divided into to $R_{sw,in,g}$ and $R_{sw,in,v}$. The subscripts "*g*" and "*v*" indicate radiation without and with vegetative canopy interaction, respectively. The incoming longwave radiation $R_{lw,in}$ is also divided to $R_{lw,in,g}$ and $R_{lw,in,v}$. From the aspect of vegetation, the sum of

incoming radiation $R_{in,v}$ (i.e. $R_{sw,in,v} + R_{lw,in,v}$) consists of direct radiation from the sun and diffuse radiation from atmosphere and ground, and the part of $R_{in,v}$ adsorbed by canopy is emitted as $R_{lw,out,v}$ to the atmosphere and the ground. Part of the incoming shortwave radiation $R_{sw,in,v}$ is directly reflected back as $R_{sw,out,v}$ to the atmosphere, while another part of $R_{sw,in,v}$ is transmitted through the canopy as $R_{sw,out,LAI}$. The vegetative canopy is regarded as a medium composed of leaves. The radiative transfer involving vegetation can be calculated by the two stream approximation (Dickinson, 1983; Sellers, 1985). In this approximation, $R_{sw,out,LAI}$ exits the canopy by transmission $e^{-K(LAI)}$, where *K* is the optical depth of the direct beam per unit leaf area. The emissivity of vegetation ε_v concerned in $R_{lw,out,v}$ is expressed as:

$$\varepsilon_v = 1 - e^{-(LAI)/\bar{u}} \tag{2.5}$$

where $\bar{u}$ is the average inverse optical depth for longwave radiation. Transmission and emission through the canopy are affected by LAI; thus LAI is important for the calculations of radiative transfer with vegetation. The concept and theory of LAI is discussed in section 2.4.1.

2.2 Heat flux scheme

As shown in **Figure 2.2 (a)**, after the incoming radiation is reflected and/or emitted from the surface, the remaining net radiation (R_{net}) is converted into latent heat flux (λE), sensible heat flux (*H*), ground heat flux (*G*), and internal energy storage (*ΔQ*), expressed as:

$$R_{net} = \lambda E + H + G + \Delta Q \tag{2.6}$$

where the unit of each term is W m^{-2}. The internal energy storage ΔQ here can be assumed to be very small and is mostly neglected. The energy balance therefore is simplified to:

$$R_{net} = \lambda E + H + G \tag{2.7}$$

λ is the latent heat of vaporization water (J kg^{-1}) and *E* is the sum of all water vapor transfers (kg m^{-2} s^{-1}). λE is then the energy used to transport water from the surface to the atmosphere,

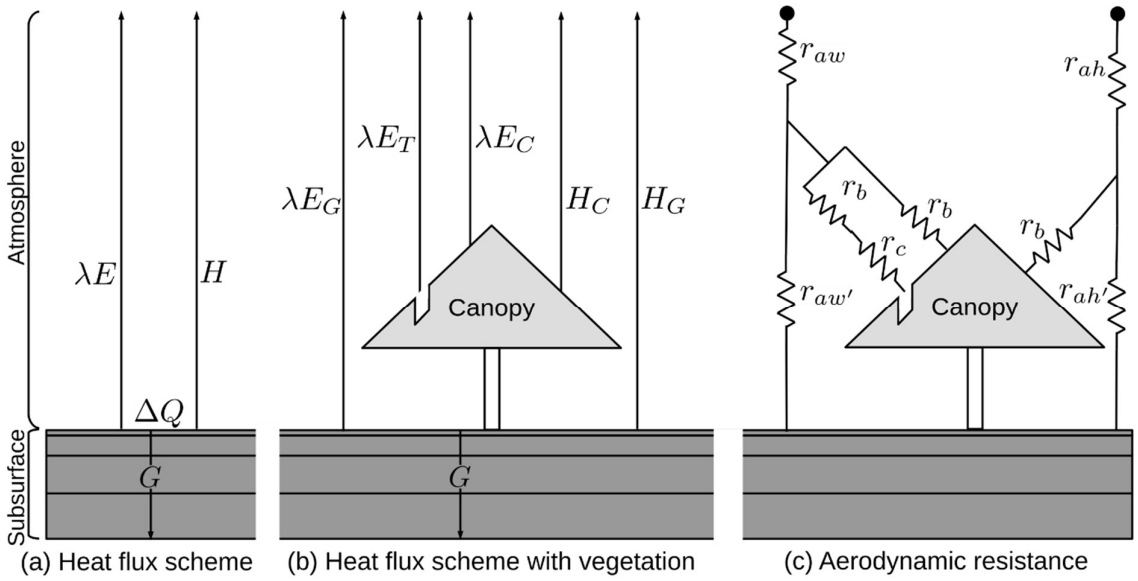

Figure 2.2. heat flux scheme (a) without vegetation, (b) with vegetation, and (c) expressed as aerodynamic resistance formulation.

including water evaporated from ground and leaf surfaces and water transpired from the roots. λE is complicated because it needs to satisfy both energy and mass (i.e. water mass) conservation simultaneously. The water vapor transfer (E) is driven by the gradient of humidity Δq (kg kg^{-1}) expressed as:

$$E = -\rho_{atm} \frac{\Delta q}{r_{aw}} \tag{2.8}$$

with the density of moisture air ρ_{atm} (kg m^{-3}) and the resistance to water vapor transfer r_{aw} (s m^{-1}). *H* is the energy transfer from the land surface to the atmosphere. H is driven by the gradient of temperature ΔT (K) and expressed as:

$$H = -\rho_{atm} C_p \frac{\Delta \mathrm{T}}{r_{ah}} \tag{2.9}$$

with the specific heat capacity of air at constant pressure C_p (J kg^{-1} K^{-1}) and the resistance to heat transfer r_{ah}. G is the energy transferred from the land surface to the subsurface due to the temperature gradient in the subsurface.

When vegetation is considered in LSMs, λE and H are separated into ground components (notified by subscript "*G*") and vegetation components (notified by subscript "*V*"). Water vapor transfer from vegetation E_V can be separated into transpiration and evaporation from the canopy (E_T and E_C). The complete equation of heat flux scheme with vegetation can thus be expressed as:

$$R_{net} = \lambda(E_G + E_T + E_C) + H_V + H_G + G \tag{2.10}$$

Two widely accepted descriptions involving λE are the Penman-Monteith equation and the aerodynamic resistance formulation. The Penman-Monteith equation describes only the latent heat flux while the aerodynamic resistance formulation solves both for latent heat flux (including $E_C, E_G, and\ E_T$) and sensible heat flux (including H_V and H_G) simultaneously.

The aerodynamic resistance formulation regards the heat fluxes as a circuit, which is driven by the water vapor gradient and the temperature gradients. R_{net} is the source of energy and energy conservation requires, that the sum of all heat fluxes is equal to R_{net}. This aerodynamic circuit can be solved following Ohm's law. Without vegetation, the aerodynamic resistances for water vapor transfer and heat transfer are r_{aw} (s m^{-1}) and r_{ah} (s m^{-1}), respectively; both determine the heat flux rates. When vegetation is considered, as shown in **Figure 2.2 (c)**, r_{aw} is divided into r_{aw} and $r_{aw'}$ ("$r_{aw'}$" is the resistance to water vapor transfer from land surface to the canopy). By the similar consideration, r_{ah} is divided to r_{ah} and $r_{ah'}$. Heat transfer from the canopy to the atmosphere is determined by the resistance of leaf boundary layer (r_b). However, water vapor transfer from the canopy is determined both by r_b and the canopy resistance r_c (the reciprocal of canopy conductance, which is related to stomatal conductance and LAI). Hence, water vapor transfer from the canopy is considered to follow two paths: evaporation from the leaves controlled by r_b and transpiration from the stomata controlled by r_c leading to

$$E_T = -\rho_{atm}\frac{(\Delta q\ )}{r_c + r_b} \tag{2.11}$$

2.3 Hydrological scheme

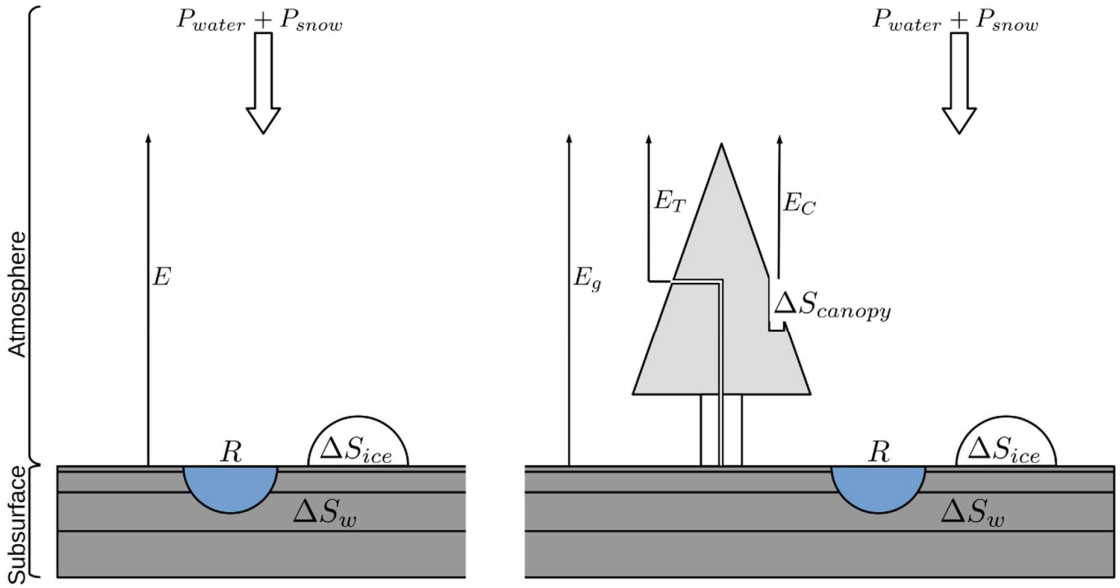

Figure 2.3. Hydrological scheme (a) without vegetation and (b) without vegetation.

In land-atmosphere interactions schemes, the water fluxes must obey mass conservation and are contained in hydrological schemes. As shown in **Figure 2.3 (a)**, the input of water on the land surface is solid or liquid precipitation ($P = P_{water.} + P_{snow.}$, kg m^{-2} s^{-1}). The output is the water vapor transfer (E) from the land surface to atmosphere by evaporation. The liquid water flows over land as runoff (R, kg m^{-2} s^{-1}) or infiltrates into the soil and increases the soil water storage (S_w, kg m^{-2}). Solid water is formed as ice content or snowpack (S_{ice}, kg m^{-2}). The water conservation on the land surface can be expressed as:

$$P = (P_{Liq.} + P_{sol.}) = E + R + \frac{\partial S_w}{\partial t} + \frac{\partial S_{ice}}{\partial t} \quad (2.12)$$

When vegetation is considered, the concept of hydrological scheme can be described as shown in **Figure 2.3 (b)**. Part of the liquid water is stored in the canopy as the interception of precipitation (S_{canopy}, kg m^{-2}). Water vapor transfer is divided into evaporation from the soil (E_G), evaporation from the canopy (E_C) and transpiration (E_T). The hydrological scheme as commonly employed in LSMs is now expressed as:

$$P = E_G + E_C + E_T + R + \frac{\partial S_w}{\partial t} + \frac{\partial S_{ice}}{\partial t} + \frac{\partial S_{canopy}}{\partial t} \quad (2.13)$$

Each term can be further described by different physical concepts. The water transfer terms (E_G, E_T, and E_C) are described by the water transfer equation (Equation 2.8). Different snow schemes are used to estimate S_{ice} and the height of the snowpack, which affect the snow coverage of vegetation. The term S_{canopy} involves different interception equations (Liu, 1997), and is generally expressed as:

$$\frac{\partial S_{canopy}}{\partial t} = q_{intr} - q_{drip} - E_c \geq 0 \quad (2.14)$$

In this equation, $q_{intr}$is the interception of precipitation, and q_{drip} is the water flow through the canopy when the water content on leaves is saturated. The interception of precipitation in CLM3.5 (Oleson *et al.*, 2004), which is employed in this thesis, is expressed as an exponential function of precipitation and LAI:

$$q_{intr} = P \cdot (1 - e^{0.5LAI}) \quad (2.15)$$

Thus LAI affects the water storage in the canopy, which further impacts the hydrological scheme.

S_w determines the water transfer into the atmosphere from ground and vegetation, and plays an important role in the heat flux and vegetation schemes. S_w can be obtained from soil water content (θ_w) driven by Darcy's equation. θ_w is defined as the volume of water (m^3) per unit volume of soil (m^3), and has the relationship with S_w as:

$$S_w = \theta_w \rho_w \Delta z_{sub} \quad (2.16)$$

with ρ_w (kg m^{-3}) liquid water density and Δz_{sub} (m) thickness of the subsurface layer. The change of soil water content with time obeys the continuity equation:

$$\frac{\partial \theta_w}{\partial t} = -\frac{\partial q}{\partial z} - q_s \tag{2.17}$$

with q (m s^{-1}) the flow rate of soil water, z (m) the gravitation potential, and q_s (s^{-1}) the sink/source term (e.g. ground evaporation (E_G), transpiration (E_T), or infiltration from surface(q_{in})). Under saturated conditions, Darcy's equation gives the flow rate of soil water (q) via the hydraulic conductivity (k, m s^{-1}) multiplied by the hydrological gradient ($\partial \psi_h / \partial z$):

$$q = -k\left(\frac{\partial \psi_h}{\partial \mathrm{z}}\right) \tag{2.18}$$

The hydraulic potential (ψ_h, m) can be expressed as $\psi_m + \psi_z$, where ψ_m and ψ_z are soil the matric and gravitation potential, respectively. With z the gravitation potential and the soil matric potential re-written as ψ, Darcy's equation becomes:

$$q = -k[\frac{\partial(\psi + z)}{\partial z}] \tag{2.19}$$

By considering the change of θ_w, Darcy's equation can be further written as:

$$q = -k(\frac{\partial \theta_w}{\partial z}\frac{\partial \psi}{\partial \theta_w} + 1) \tag{2.20}$$

The hydraulic conductivity varies with the soil moisture θ_w, which can be obtained from soil water retention curve; thus k is replaced by $k(\theta_w)$. The continuity equation of soil water can then be further expressed as:

$$\frac{\partial \theta_w}{\partial t} = \frac{\partial}{\partial z}\left[k(\theta_w)\left(\frac{\partial \theta_w}{\partial z}\frac{\partial \psi}{\partial \theta_w}\right) + 1\right] - q_s \tag{2.21}$$

Darcy's equation is applied in saturated condition but the soil is not always saturated. Buckingham (1907) derived an equation for unsaturated conditions, which was extended by Richards to three-dimensional flow (without the consideration of water compressibility):

$$\frac{\partial \theta_w}{\partial t} = \nabla \cdot [k(\theta_w)\nabla\psi] - q_s \quad (2.22)$$

This equation, known as Richards equation formulates the relationship between the change of soil water content with time and the water diffusion in subsurface.

2.4 Vegetation schemes

According to a global atmospheric simulation without vegetation (Shukla & Mintz, 1982), the ground temperature in some area would increase by 15-25 ^{o}C and the atmosphere surface pressure over the continents would decrease by 5-15 mbar. A deforestation study over the Amazon basin results in latent heat flux decreases due to less consumption of radiation by vegetation and increases of ground temperature (2-5 K) and runoff (Dickinson & Henderson-Sellers, 1988). Also Bonan (2008) and Jung (2010) stress the importance of vegetation for these processes.

Vegetation schemes include many sub-schemes, e.g. LAI (Arora, 2002), vegetation height (Garratt, 1993), stomatal conductance (Damour *et al.*, 2010), photosynthesis (Farquhar *et al.*, 2001), leaf interception (Savenije, 2004), and root distribution (Desborough, 1997). All these sub-schemes connect with the radiative transfer, heat flux, and hydrological schemes. Stomatal conductance affects the heat flux by the transpiration. LAI affects radiative transfer by transmissivity and emissivity of vegetation, the heat flux by transpiration, and hydrology by precipitation interception. The roots affect hydrology by the sink/source term. Therefore, the characteristic of vegetation sub-schemes for stomatal conductance, LAI, and roots are explained in more detail in Section 2.4.1 to Section 2.4.3.

2.4.1 Stomatal conductance scheme

A stoma is a micro-scale pore on the leaf and stem surfaces. This vegetation organ is bounded by a pair of guard cells which controls the opening and thus gas exchange. By photosynthesis, carbon dioxide gas is captured via the stomata and oxygen gas is released into the atmosphere. Stomatal openings also release water vapor into atmosphere and thus control transpiration.

The water vapor flux through stomata is described as stomatal conductance (g_s, m s^{-1}).

More than forty stomatal conductance schemes are currently used (Damour *et al.*, 2010). As mentioned in Chapter 1, two well-accepted stomatal conductance equation types are the J-type and the BB-type. According to Jarvis (1976) environmental stresses limit the maximum stomatal conductance $g_{s,max}$, which are formulated as stress functions depending on photon flux density $f(Q_p)$, leaf temperature $f(T_{leaf})$, vapor pressure deficit $f(\delta e)$, carbon dioxide concentration $f(C_a)$, and leaf water potential $f(\psi_{leaf})$. A stress function is an empirical dimensionless scalar potential function which ranges from 0 to 1. The J-type stomatal conductance g_s is described by multiplying these stress functions with the maximum stomatal conductance:

$$g_s = g_{s,max} f(Q_p) f(T_{leaf}) f(\delta e) f(C_a) f(\psi_{leaf}). \quad (2.23)$$

The stress function for photon flux density, $f(Q_p)$, is formulated as a hyperbolic function

$$f(Q_p) = \frac{c_1 c_2 (Q_p - c_3/c_1)}{c_1 + c_2 (Q_P - c_3/c_1)}. \quad (2.24)$$

When Q_p equals zero, $f(Q_p)$ approaches its minimum value designed to maintain a minimum stomatal conductance at night.

The stress function for leaf temperature, $f(T_{leaf})$, is expressed as:

$$f(T_{leaf}) = \frac{(T_{leaf} - T_{low})(T_{high} - T_{leaf})^{(T_{high} - T_0)/(T_{high} - T_{low})}}{(T_0 - T_{low})(T_{high} - T_0)^{(T_{high} - T_0)/(T_{high} - T_{low})}} \quad (2.25)$$

T_0 is the temperature when $f(T_{leaf})$ is 1. T_{low} and T_{high} indicate the temperature range within which stomata are open, i.e. when $f(T_{leaf}) \geq 0$. When the leaf temperature is at T_0, stomatal opening reaches its maximum ($f(T_{leaf}) = 1$ when $T_{leaf} = T_0$).

The stress function for water vapor pressure deficit at the leaf surface, $f(\delta e)$, is assumed to be linear:

$$f(\delta e) = 1 - c_4 \delta e. \tag{2.26}$$

Vapor pressure deficit, δe, is defined as the difference between the surrounding water vapor pressure and the saturated water vapor pressure on the leaf surface. When the surrounding air is saturated with water vapor ($\delta e = 0$), the stomatal conductance reaches its maximum ($f(\delta e) = 1$).

When carbon dioxide concentration is below 100 cm^3/m^3, the stress function of carbon dioxide concentration approaches 1; its minimum is reached at 1000 cm^3/m^3:

$$f(C_a) = \begin{cases} 1 & C_a < 100 \\ 1 - c_5 C_a & 100 < C_a < 1000 \\ c_6 & C_a > 1000 \end{cases}. \tag{2.27}$$

The leaf water potential ψ_{leaf} drives water from soil to the plant leaves; its stress function $f(\psi_{leaf})$ is formulated as a negative exponential function:

$$f(\psi_{leaf}) = 1 - e^{-c_7(\psi_{leaf} - \psi_m)} \tag{2.28}$$

At ψ_m $f(\psi_{leaf}) = 0$, which closes the stomata.

Following Jarvis (1976), different formulas of stomatal conductance are proposed. Stewart (1988) proposes a similar expression which depends on LAI:

$$g_s = g_{s,max} LAI \cdot f(R_{total}) f(T_{leaf}) f(\delta e) f(\theta_w). \tag{2.29}$$

Two stress functions for $f(Q_p)$ and $f(\psi_{leaf})$ are replaced by a stress functions for total solar radiation $f(R_{total})$ and soil water deficit $f(\theta_w)$. $f(Q_p)$ and $f(\psi_{leaf})$ are not considered by Stewart because of difficulties to estimate those. Stewart (1988) finds differences of less than -13.8% between simulated and observed water vapor fluxes.

Many other modifications of the J-type formulas are proposed by e.g. Rana *et al.* (1998) and Langensiepen *et al.* (2009). One well-accepted modification (Dickinson *et al.*, 1991) replace $L_{AI} f(R_{total})$ by $f(PAR)$, the stress function of photosynthesis active radiation:

$$f(PAR) = \frac{f + g_{s,min}/g_{s,max}}{1 + f} \tag{2.30}$$

$$f = \frac{2PAR}{R_{GL}} \tag{2.31}$$

with the limitation parameter R_{GL}, which differs between vegetation types. Another modification formulates the stress function for soil water deficit $f(\theta_w)$ as an indicator function:

$$f(\theta_w) = \begin{cases} 1 & \theta_w \geq \theta_{cr} \\ \dfrac{\theta_w - \theta_{wilt}}{\theta_{cr} - \theta_{wilt}} & \theta_{wilt} < \theta_w < \theta_{cr} \\ 0 & \theta_w \leq \theta_{wilt} \end{cases} \tag{2.32}$$

where θ_{wilt} and θ_{cr} are the wilting point and the critical point of soil water content, respectively. θ_{wilt} indicates the minimum soil water content for vegetation to live. θ_{cr} is the critical point above which stomatal conductance is maximum. Nowadays the JS-type stomatal conductance equation usually refers to the original expression of equation 2.29 including the modifications by equation 2.30-2.32, and is widely employed in LSMs, e.g. SiB (Sellers *et al.*, 1996), BATS (Dickinson *et al.*, 1993), VIC (Liang *et al.*, 1994), Noah (Ek *et al.*, 2003), and Terra LSM (Graßelt, 2009).

The J-type stomatal conductance equation does not include photosynthesis as an important bio-chemical reaction that affects transpiration by carbon dioxide concentration. Ball *et al.* (1987) propose a stomatal conductance equation varying with the photosynthesis known as the BB-type stomatal conductance equation, which is expressed with the carbon dioxide assimilation rate by photosynthesis A (mol m^{-2} s^{-1}) and the mole fraction of carbon dioxide at the leaf surface C_s (mol mol^{-1}):

$$g_s = m\frac{AH_R}{C_s} \tag{2.33}$$

with m an empirical constant and H_R relative humidity (both unitless). The unit of g_s in the BB-type equation is mol m^{-2} s^{-1}; in the JS-type equation it is m s^{-1}. In the equation first derived by Ball *et al.* (1987), A is measured experimentally. Nowadays, A in the BB-type formulations is replaced by the net carbon dioxide assimilation rate (A_{net}, µmol m^{-2} s^{-1}), which is first

proposed by Farquhar *et al.* (1980):

$$A_{net} = V_C + 0.5V_O - R_d \tag{2.34}$$

with V_C (µmol m^{-2} s^{-1}) the carboxylation rate, V_O (µmol m^{-2} s^{-1}) the oxygenation rate, and R_d (µmol m^{-2} s^{-1}) the dark respiration rate. V_C can be expressed as an indicator function:

$$V_C = \min(J_E, J_C) \tag{2.35}$$

With V_C a rate-limited step depending on the minimum value of the photosynthetic electron transport J_E (µmol m^{-2} s^{-1}) and Rubisco J_C (µmol m^{-2} s^{-1}). Both J_E and J_C depend on carbon dioxide concentration and temperature, and J_E additionally depends on the incident flux of photosynthetically active radiation.

Based on Equation 2.33, Collatz *et* al. (1991) propose another stomatal conductance equation (hereafter the BBC-type) with a minimum stomatal conductance ($g_{s,min}$, µmol m^{-2} s^{-1}):

$$g_s = g_{s,min} + m\frac{A_{net}H_R}{C_s} \tag{2.36}$$

where C_s and H_R are CO_2 concentration at the leaf surface and relative humidity, respectively. A_{net} is here calculated as:

$$A_{net} = \min(J_E, J_C, J_S) - R_d \tag{2.37}$$

with J_S (µmol m^{-2} s^{-1}) the assimilation rate of sucrose synthesis, which is proposed by Farquhar and Kirschbaum (1984). This type of stomatal conductance equation is widely used in third generation LSMs and employed e.g. in the Community Land Model (Oleson *et al.*, 2004) and NOAH-MP (Niu *et al.*, 2011).

For air humidity in the stomatal conductance equations, the JS-type uses a function of vapor pressure deficit δe, and the BBC-type uses relative humidity H_R :

$$f(\delta e) = D_0\, \delta e = D_0(\, e_{sat} - e) \tag{2.38}$$

$$H_R = \frac{e}{e_{sat}} \tag{2.39}$$

where e (kPa or kg kg^{-1}) and e_{sat} (kPa or kg kg^{-1}) are the ambient humidity and the saturated humidity, respectively. e_{sat} can be obtained by a function of temperature. D_0 is a plant species dependent parameter, thus different plants may have different responses to ambient humidity. Which one of the above dependencies is more suitable has been debated since 1936 (Anderson, 1936; Mott & Parkhurst, 1991; Aphalo & Jarvis, 1993; Monteith, 1995; Oren *et al.*, 1999; Addington *et al.*, 2004).

Since the relationship between vapor pressure deficit and stomatal conductance is widely accepted (Anderson, 1936; Aphalo & Jarvis, 1993; Oren *et al.*, 1999; Addington *et al.*, 2004), Leuning (1995) modifies the BBC-type accordingly and formulates a new stomatal conductance equation, the BBL-type, which is employed e.g. in CABLE and JULES (with simplifications):

$$g_s = g_{s,min} + m\frac{A_{net} f(\delta e)}{C_s - \Gamma} \tag{2.40}$$

The mole fraction of carbon dioxide C_s is replaced by $C_s - \Gamma$. Γ is the carbon dioxide compensation point, and A_{net} approaches 0 as C_s approaches Γ. Leuning (1995) proposes $f(\delta e)$ different from the JS-type as a hyperbolic function following Lohammar *et al.* (1980):

$$f(\delta e) = (1 + \delta e / D_0)^{-1}. \tag{2.41}$$

Both Leuning (1995) and Van Wijk et al. (2000) find that the BBL-type better suited than the BBC-type when employing the vapor pressure deficit.

Different studies have addressed the different behaviour of the three stomatal conductance formulations. Many studies compare the Jarvis-like type (e.g. the J-type and the JS-type) against the Ball-Woodrow-Berry-like type (e.g. the BB-type, the BBC-type, and the BBL-type) by comparison against observations. Niyogi & Raman (1997) suggest that the BBC-type is better than the J-type. Cox et al. (1998) shows that the BBC-type better estimates the stomatal conductance when compared against observations. However, Hoshika *et al.* (2017) concludes

that both the BBC-type and the JS-type well explain the stomatal conductance against measurement. Ronda *et al.* (2001) compare two stomatal conductance equations (the BBL-type and the JS-type) with observations from three sites (FIFA-Kansas, HAPEX-MOBILHY, and Cabauw). The BBL-type performs better than the J-type in FIFA-Kansas and HAPEX-MOBILHY, but the J-type performs better than BBL-type in Cabauw. However, by using the same observations at FIFA-Kansas, Niu *et al.* (2011) find better results by the JS-type, while Ronda *et al*. (2001) finds better results using the BBC-type). While Ronda *et al* (2001) and Niu *et al* (2011) employ the JS-type equation and the same observations, they use these formulations in different LSMs (a simplified LSM employed by Ronda *et al* (2001) and Noah-MP employed by Niu *et al* (2011)). Hence, the differences may not only result from the different stomatal conductance equations but also from the different the structures of these LSMs. Furthermore, the JS-type equations used in both studies differ in their stress functions. Ran *et al.* (2017) conclude that neither the JS-type or the BBC-type dominates the simulation results employing the PX-LSM. Thus it is challengeable to state which stomatal conductance equation performs better.

2.4.2 Leaf area index scheme

LAI represents the canopy structure and is used to up-scale the vegetation-atmosphere interaction from the leaf scale to the canopy scale (Running & Coughlan, 1988; Running *et al.*, 1989). LAI can be determined by field measurement (Chen *et al.*, 1997; Gower *et al.*, 1999; Reichenau *et al.*, 2016), satellite observations (Myneni, 2002; Garrigues *et al.*, 2008), or by modelling (Haxeltine *et al.*, 1996; Dickinson *et al.*, 1998; Ewert, 2004).

The measurement of LAI in the field is an intensive work (Jonckheere *et al.*, 2004). Satellite data, such as the Advanced Very High Radiometer (AVHRR) and the Moderate Resolution Imaging Spectroradiometer (MODIS), can provide temporally and spatially uniform data, but are limited by environmental factors and the quality of the measurement devices. Hence, the dynamic LAI scheme is an alternative. Before satellite data led to acceptable results, many studies estimate LAI by dynamic LAI schemes. Dickinson *et* al. (1993) use soil temperature to estimate the LAI. Haxeltine *et* al. (1996) simulate LAI derived from plant growth from the

combined carbon and water cycle. Dickinson *et* al. (1998) propose a LAI scheme derived as plant growth with stress functions depending on carbon dioxide assimilation, drought, and temperature. Kergoat (1998) use a relationship between LAI and the hydrological state. Crop growth schemes consider plant growth via photosynthesis to estimate LAI (Yin *et al.*, 2000). Ewert (2004) estimates LAI by utilizing the connection between LAI and plant growth related to carbon dioxide concentration. LAI can be also derived from a complex dynamic scheme of vegetation growth with the carbon and nitrogen cycles (Sitch *et al.*, 2003).

None of the discussed dynamic LAI schemes is well-accepted. Some schemes are restricted to specific plant types (Yin *et al.*, 2000); some schemes are even published without validation against observations (Haxeltine *et al.*, 1996; Kergoat, 1998; Ewert, 2004). Dynamic schemes may better approach reality but are difficult to implement in current LSM because of missing information (Levis *et al.*, 2004; Thornton & Rosenbloom, 2005). Thus the LAI scheme proposed by Dickinson *et al.* (1993) is utilized in this thesis:

$$LAI = LAI^{min} + F_{sea}(LAI^{max} - LAI^{min}) \tag{2.42}$$

$$F_{sea} = 1 - 0.0016\left(298.0 - T_g\right)^2 \tag{2.43}$$

with LAI^{min} (m^2 m^{-2}) the minimum LAI, LAI^{max} (m^2 m^{-2}) the maximum LAI, and F_{sea} a seasonal stress function based on soil temperature (T_g) at 0.2m depth and constrained between 0 and 1. At T_g = 298.0 K, LAI growth is maximum (LAI^{max}). When the soil temperature is too high or too low, LAI approaches LAI^{max}. L_{AI}^{max} and LAI^{max} are estimated from observations.

2.4.3 Root scheme

The root scheme connects the whole soil(subsurface)-vegetation-atmosphere interaction. Roots take up water and transport it to the upper plants, where it is transpired via the stomata. Roots sense the soil water content and may affect the stomatal opening (Steduto & Hsiao, 1998; Pitman, 2003; Addington *et al.*, 2004; Krishnan *et al.*, 2006). Hence, root schemes simulate water uptake water from the soil via a root density distribution in subsurface and use

soil water as a limitation function.

The root distribution varies with depth and determine where soil water can be extracted. Some studies (Sellers *et al.*, 1986; Dickinson *et al.*, 1993) assume that the root distribution is homogeneous down to a certain depth (z_h); thus the maximum amount of water available for transpiration is the soil water content within z_h. Some advanced studies (Oleson *et al.*, 2004a; Niu *et al.*, 2011) assume that the root density decreases with increasing depth. In the present study the root distribution r_i of the *i*-th subsurface layer is expressed with root distribution parameters $r_{root,a}$ and $r_{root,b}$ as:

$$r_i = 0.5(e^{-r_{root,a} \cdot z_{h,i-1}} + e^{-r_{root,b} \cdot z_{h,i-1}} + e^{-r_{root,a} \cdot z_{h,i}} + e^{-r_{root,b} \cdot z_{h,i}}) \quad (2.44)$$

$$r_i = 0.5(e^{-r_{root,a} \cdot z_{h,i-1}} + e^{-r_{root,b} \cdot z_{h,i-1}}) \quad (2.45)$$

where $r_{root,a}$ and $r_{root,b}$ differ between plant types with $z_{h,i}$ the depth at the *i*-th layer. Equation 2.45 is used from the first layer to the second last layer, and Equation 2.46 is used at the last (maximum 10) layer (i_{last}). The water uptake $e_{T,i}$ (kg m^{-2} s^{-1}) from transpiration (E_T) at *i*-th layer is the calculated as:

$$e_{T,i} = E_T \cdot r_i \quad (2.46)$$

The stress function for soil water depends on the soil water content θ_w sensed by roots. Different stress functions for soil water are proposed (Niu *et al.*, 2011). Manabe (1969) proposed the first stress function for soil water, which is then applied by MIT LSM (Entekhabi & Eagleson, 1989):

$$f(\theta_w) = \frac{\theta_w - \theta_{wilt}}{0.75(\theta_{fc} - \theta_{wilt})} \quad (2.47)$$

with θ_{fc} the soil water content at field capacity. When the soil is dry ($\theta_w = \theta_{wilt}$), stomata close ($f(\theta_w) = 0$) following the well-accepted stress function in Equation 2.32 by Noilhan & Planton (1989). The stress function for soil water $f(\theta_w)$ is further replaced by the soil water limitation factor β_t, which considers that the stress function of soil water differs with depth:

$$\beta_t = \sum_{i=1}^{i_{last}} f(\theta_{w,i}) \cdot r_i \tag{2.48}$$

where $f(\theta_{w,i})$ is the stress function of soil water ($\theta_{w,i}$) in the *i*-th layer. In this thesis, β_t employs Equation 2.32 for the stress function of soil water and Equations 2.44 and 2.45 for the root distribution.

2.5 Groundwater model

A groundwater model calculates the three-dimensional soil water movement in the subsurface and may include an overland flow equation, which describes the water flow when land surface is fully saturated or when rainfall rate exceeds the infiltration rate. Overland flow can be considered as the change of water ponding ψ_s(m) on the land surface with time t(s), and is expressed as a continuity equation:

$$\frac{\partial \psi_s}{\partial t} = \nabla \vec{v} \psi_s + q_r + q_e \tag{2.49}$$

with q_e (m s^{-1}) the water exchange rate through the land surface, and q_r (m s^{-1}) the precipitation as sink terms. The flow velocity of water $\vec{v}$ (m s^{-1}) controls the outflow of water in the system and is affected by the roughness of land surface. $\vec{v}$ can be described by different concepts; one well-accepted concept is Manning's equation:

$$\vec{v} = \frac{\sqrt{S_f}}{n} \psi_s^{2/3} \tag{2.50}$$

where S_f (dimensionless) is the frictional slope and n ($m^{-1/3}$ s) is the Manning's coefficient.

The subsurface flow is described by Richards' equation (Richards, 1931). Richards' equation without the consideration of water released from aquifer is shown in Equation 2.22. The water released from aquifer with the change of the hydraulic potential ψ_h (m) is given by:

$$S_s \theta_s(\psi_h) \frac{\partial \psi_h}{\partial t} \tag{2.51}$$

with S_s (m^{-1}) the specific storage coefficient, θ_s (dimensionless) the degree of saturation i.e. the soil water content in the pores (ϕ, dimensionless). The soil water content θ_W in Equation 2.22 can be obtained by $\theta_w = \theta_s(\psi_h)\phi$. Richards' equation with the consideration of water compressibility can be expressed as:

$$S_s \theta_s(\psi_h) \frac{\partial \psi_h}{\partial t} + \frac{\partial(\theta_s(\psi_h) \cdot \phi)}{\partial t} = \nabla \cdot q + q_s \tag{2.52}$$

with q (m s^{-1}) the soil water flow rate and q_s (s^{-1}) the sink/source term, which consists of transpiration (E_T), ground evaporation (E_G), and infiltration (q_{in}). q can be expressed as:

$$q = -k_s k_r(\psi_h) \nabla(\psi_h - z) \tag{2.53}$$

where k_s (m s^{-1}) and k_r (dimensionless) are the saturated hydraulic conductivity and the relative hydraulic conductivity, respectively. The relative hydraulic conductivity can be obtained from soil water retention curves (Clapp & Hornberger, 1978; van Genuchten, 1980). z is the depth with $z = 0$ the land surface.

A groundwater model solves the above partial differential equations by the finite element or finite difference method. To represent the heterogeneity of the subsurface the modelling domain is usually discretized into cubic or triangular grid elements. The boundary condition includes the water exchange rate through land surface q_e and the lateral flow at the boundaries.

Figure 2.4 shows the coupling of a LSM and groundwater model including the sink/source term q_s and the hydrological terms (soil water content θ_w and hydraulic potential ψ_h). The sink/source term q_s includes transpiration E_T, ground evaporation E_G, and infiltration q_{in} in LSM, and is an input parameter to groundwater model. By Richards' Equation, soil water content and hydraulic potential are obtained by using the sink/source term q_s from LSM. The LSM uses the soil water content and hydraulic potential calculated by the groundwater model

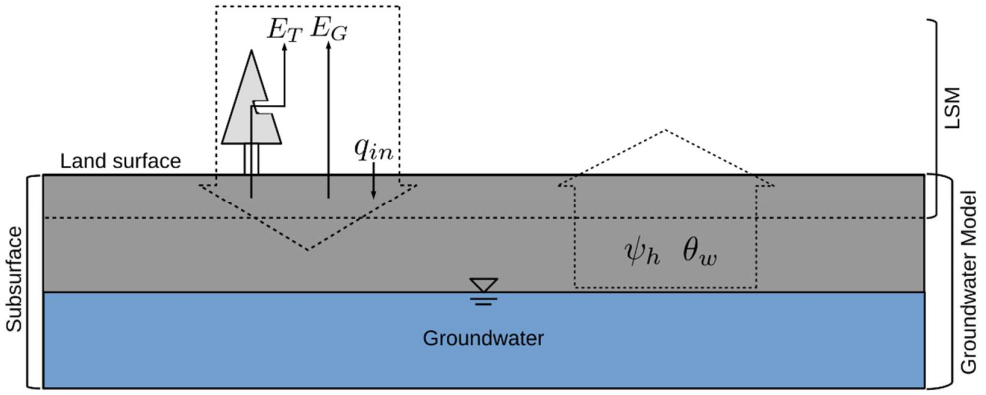

Figure 2.4. The coupling of groundwater model and LSM. E_T, E_G, q_{in} are the transpiration, ground evaporation, and infiltration, respectively. ψ_h is the hydraulic potential, and θ_w is the soil water content.

to calculate transpiration and ground evaporation. As discussed in Chapter 1, the soil water content and the hydraulic potential in a one-dimensional LSM can be improved by the three-dimensional groundwater model. Thus the groundwater and land-atmosphere are coupled and allow for two-way feedbacks between groundwater flow and the heat fluxes (Kollet & Maxwell, 2008; Maxwell & Condon, 2016).

Chapter 3

Method and material

This chapter introduces the numerical experiments performed in this study with the regional Earth system model platform TerrSysMP, which is introduced in Section 3.1 . The LSM (CLM3.5) and the coupled model LSM with the groundwater model (CLM3.5 and Parflow) are introduced in Section 3.2 and Section 3.3 , respectively. Additional vegetation sub-schemes are implemented in CLM3.5, which is introduced in Section 3.4 . Section 3.5 describes the methods to evaluate the simulations. Study location and observations are described in Section 3.6 .

3.1 Modelling platform: TerrSysMP

The Terrestrial System Modelling Platform (TerrSysMP) (Shrestha *et al.*, 2014; Gasper *et al.*, 2014; Simmer *et al.*, 2015) is a soil-vegetation-atmosphere simulation platform developed by the Transregional Collaborative Research Centre 32. This model platform has three components: the three-dimensional groundwater model Parflow (Jones & Woodward, 2001; Maxwell & Miller, 2005; Kollet & Maxwell, 2008), the Community Land Model version 3.5 (CLM3.5) (Oleson *et al.*, 2004), and the atmospheric model COnsortium for Small scale MOdelling (COSMO), which is a non-hydrostatic limited-area atmospheric prediction model (Steppeler *et al.*, 2003; Baldauf *et al.*, 2011). These three components are coupled through an external coupler, the Ocean Atmosphere Sea Ice Coupling framework (OASIS) (Valcke, 2013), which exchanges data of fluxes and state variables through upscaling and downscaling . Thus, OASIS can connect different components with different spatial and temporal resolution.

CLM3.5 is utilized to investigate the land-atmospheric interaction, and Parflow is utilized to investigate the dynamic groundwater flow. To study the interaction between the dynamic

groundwater and heat fluxes, the coupled surface-subsurface mode of TerrSysMP (Parflow-CLM3.5) is employed. In this coupled mode, CLM3.5 provides water vapor transfer and infiltration as sink/source terms of Richards' Equation in Parflow, and Parflow provides the hydrological state (i.e. soil water content and hydraulic potential) to calculate the hydrological terms (e.g. stress function of soil water, transpiration, and ground evaporation) in CLM3.5.

All simulations are performed in the high performance compute cluster "CLUMA" at the Meteorological Institute, University of Bonn. Both the simulation of CLM3.5 and PF-CLM3.5 employ the model setup from Shrestha *et al.* (2014). The criteria for terminating model spin-up for CLM3.5 are set to 0.1 (W m^{-2}) for energy fluxes (Yang *et al.*, 1995). The criteria of model spin-up for Parflow is set to 0.1% for the soil water content(Rahman *et al.*, 2014).

3.2 Land surface model: CLM3.5

CLM3.5 is a third generation LSM based on the development of CoLM, which is modified from the Bonan-LSM (Bonan, 1996), BATS (Dickinson *et al.*, 1993), and IAP94 (Dai & Zeng, 1997). According to the results of PILPS (the Project for Intercomparison of Land-surface Parameterization Schemes), the employment of common land surface processes was suggested, and utilized in many LSMs, including CLM3.5 (Shao & Henderson-Sellers, 1996; Pitman *et al.*, 1999).

Figure 3.1 illustrates the structure of CLM3.5 and the necessary input data. CLM3.5 in this thesis is applied at four locations (discussed in Section 3.6) with discretization into ten exponential-distributed soil layers. Weather forcing data are the time dependent variables (hourly time step), including incoming shortwave radiation, air temperature, precipitation, atmospheric pressure, wind speed and specific humidity provided by the observations from TERENO and TR32 research groups (H. Post and A. Klosterhalfen, by personal communication; Graf *et al.* (2014)). The incoming longwave radiation in this thesis is calculated by an equation, which depends on atmospheric vapor pressure and air temperature. The land surface data include the vegetative and geographical information. The longitude and latitude are used to calculate the sunlit or shaded vegetative leaves in the radiative transfer scheme. Soil properties are the percentage of sand content (%sand) and percentage of clay content (%clay), which are required for the calculation of the soil water movement in the hydrological scheme and for the

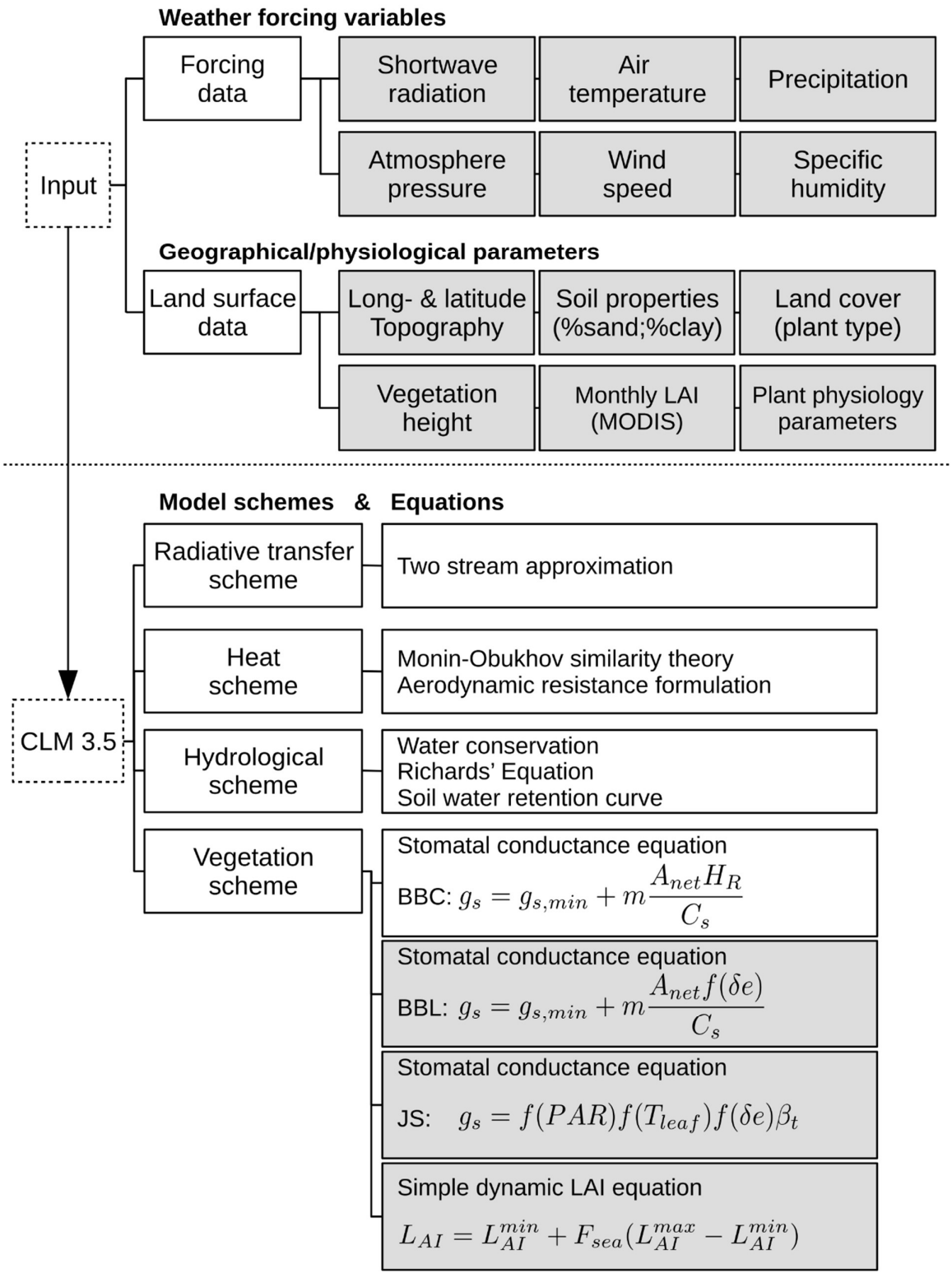

Figure 3.1. The structure of CLM3.5 and the related input data. The grey box shows the user specific or modified part of CLM3.5.

height, LAI, and plant physiology) differ between plant types. Vegetation height and LAI are dynamic and vary with the month.

CLM3.5 includes a radiative transfer scheme, a heat flux scheme, a hydrological scheme, thermal conductivity in the heat flux scheme. Vegetation parameters (land cover, vegetation and a vegetation scheme. Radiative transfer scheme follows the energy conservation (Equation 2.4) via the two-stream approximation (Dickinson, 1983; Sellers *et al.*, 1986). The calculated net radiation is utilized in heat flux scheme. The heat flux scheme employs the Monin-Obukhov similarity theory to calculate the aerodynamic resistance, which is used to estimate the water vapor transfer (Equation 2.8) and heat transfer (Equation 2.9) between surface and atmosphere (Monin & Obukhov, 1954). Equation 2.10 is used to solve the energy balance on the land surface for vegetation and ground. The ground heat flux is calculated by the energy transfer equation, which adopts the Kersten number to estimate the thermal conductivity of subsurface.

The hydrological scheme is based on the water balance equation (Equation 2.14) and the one-dimensional Darcy's Equation (Equation 2.21) to estimate the soil water content and hydraulic potential. The hydraulic conductivity varying with soil water content is estimated from the soil water retention curve from Clapp and Hornberger (1978). The water vapor transfer (E_T, E_C and E_G) are calculated by a heat flux scheme and employed in the water balance equation. The storage of canopy water is calculated by Equation 2.15. The vegetation scheme includes three stomatal conductance equations (the BBC-type, the BBL-type, and the JS-type), two LAI input types (the predefined MODIS LAI and the simple dynamic LAI), and one root distribution equation. The BBC-type stomatal conductance equation (Equation 2.36) is the default equation in CLM3.5, which adopts the net carbon dioxide assimilation rate from Collatz *et al.* (1991) (Equation 2.37). We implement codes for the BBL-type and the JS-type stomatal conductance equations in CLM3.5 (Section 3.4.1). The source and an analysis of MODIS LAI data are discussed in Section 3.6, including the simple dynamic LAI following Equation 2.42. The root distribution employs Equations 2.44 and 2.45, and the parameters of different plant types are adapted from Zeng (2001). The water uptake from the subsurface is estimated via Equation 2.46, and the stress function for soil water adopts the soil water limitation factor (Equation 2.48).

Table 3.1. The simulation modes of CLM3.5.

CLM3.5	BBC-type	BBL-type	JS-type
MODIS LAI / Updated physiological parameters	BBC-MO-U	BBL-MO-U	-
TLAI / Updated physiological parameters	BBC-TL-U	BBL-TL-U	-
MODIS LAI / Original physiological parameters	BBC-MO-O	BBL-MO-O	JS-MO-O’
TLAI / Original physiological parameters	BBC-TL-O	BBL-TL-O	JS-TL-O’

In this thesis, we quantify the uncertainty of vegetation scheme in the LSM on the exchange fluxes. Here we focus on the physiological parameters, the stomatal conductance equations, and the LAI input types. Ten simulation modes are designed and executed as listed in **Table 3.1**. To investigate the uncertainty caused by the physiological parameters, two parameters are employed: the updated physiological parameter set (noted as “U”) and the original physiological parameter set (noted as “O”). The original parameter set is provided by CLM3.5 and the updated physiological parameter set, plant-specific physiological parameters, are provided by Sulis *et al*. (2015). The updated physiological parameter set only applies on the BB-type equations. The JS-type and the BB-type equations employs different parameter sets; thus the update physiological parameters are not able to be employed by the JS-type. Two stomatal conductance equations (the BBC-type and the BBL-type) and two LAI input types (the MODIS LAI, noted as “MO” and simple dynamic LAI, noted as “TL”) are employed. Therefore, eight simulation modes, BBC-MO-U/O, BBL-MO-U/O, BBC-TL-U/O, and BBL-TL-U/O are performed for the investigation of the effects of the physiological parameter uncertainty on the exchange fluxes. The observed heat fluxes are used to evaluate the simulations in Section 4.1.

To investigate the uncertainty caused by the vegetation scheme, three stomatal conductance equations (the BBC-type, the BBL-type, and the JS-type) and two LAI input types (MODIS LAI and the simple dynamic LAI equation) are employed. The simple dynamic LAI equation are marked as “TL” and named as TLAI in the following. The BB-type stomatal

conductance equations employ the original physiological parameters because the updated physiological parameter set is not available for every plant type. The JS-type equation adopts the parameters from Noah-MP (Niu *et al.*, 2011) marked as "O'". Therefore, six simulation modes (BBC-MO-O, BBL-MO-O, JS-MO-O' BBC-TL-O, BBL-TL-O, and JS-TL-O') are performed to the investigation of the effects of the vegetation scheme uncertainty. The observed heat fluxes and soil moisture are used to evaluate the simulations, and results are shown in Section 4.1, 4.3, and 4.4

3.3 Groundwater model: Parflow

Parflow is a three-dimensional groundwater model developed by Ashby and Falgout (1996) at Lawrence Livermore National Laboratory. The Parflow code is parallelized to allow for execution on HPC infrastructures. Parflow can be used to simulate fluid flows and chemical migration in the subsurface via Richards' Equation using the soil water retention curve of van Genuchten (1980) to describe the unsaturated and saturated fluid flow. The release of water volume in aquifer is included in the calculations to better represent water storage in the subsurface. Overland flow is included by Kollet and Maxwell (2006) to provide an upper boundary condition and solved by the overland flow continuity equation (Equation 2.50) and the Manning's Equation (Equation 2.51).

Figure 3.2 illustrates structure and required input data of Parflow (in the lower part), and the coupling between Parflow and CLM3.5 (named as PF-CLM3.5 model). The horizontal resolution of Parflow is set to 500 m by 500 m. In the vertical the model is divided into thirty layers exponentially distributed in depth for the first ten layers, then a constant layer depth of 1.35 m is used. The weather forcing input for PF-CLM3.5 is different from the input for CLM3.5 because it is driven by two-dimensional weather forcing data from hourly analyses provided by the German Weather Service (Deutsche Wetterdienst). The land surface of PF-CLM3.5 is the same as CLM3.5, except that two-dimensional fields are used as required for the execution of the 3D Parflow code. Two-dimensional surface data (slopes and Manning's coefficient) are required to calculate overland flow, and three-dimensional subsurface data (porosity, saturated hydraulic conductivity, specific storage, the soil water retention curve parameters) are required to solve the three-dimensional Richards' equation. The whole groundwater

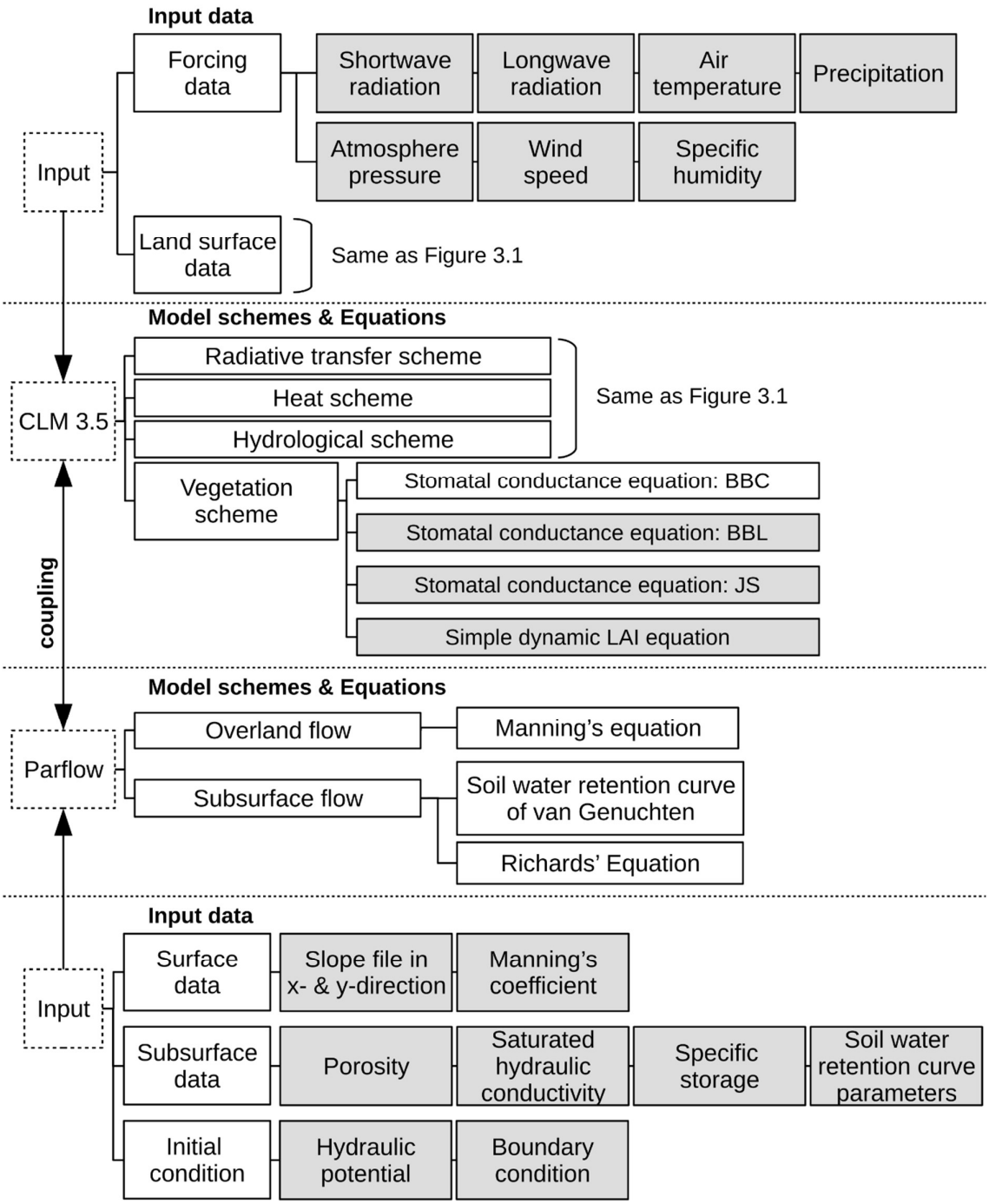

Figure 3.2. The structure of Parflow and the coupling between CLM3.5 and Parflow.

model can be considered as a box, and each side of this box requires a boundary condition. In this thesis, the top boundary condition is provided by the overland flow, and the lateral and bottom boundary condition is set to be no-flux.

The calculations of PF-CLM3.5 are performed for the Rur catchment with realistic land surface and subsurface conditions and two-dimensional weather forcing data. To investigate how the uncertainties of vegetation scheme propagate to the groundwater, the same six simulation modes for vegetation scheme uncertainty in CLM3.5 are employed for the PF-CLM3.5 model. The calculation results are shown in Chapter 5.

3.4 Implementation of vegetation sub-schemes

Two additional stomatal conductance equations and one simple dynamic LAI equation coded in FORTRAN90 are implemented in CLM3.5 and described in Section 3.4.1 and 3.4.2, respectively.

3.4.1 Implementation of the stomatal conductance equations

We implement two additional stomatal conductance equations, the BBL-type (Equation 2.40) and the JS-type (Modified Equation 2.29), as optional sub-routines in the original codes of CLM3.5. **Figure 3.3** illustrates the structure of stomatal conductance code in CLM3.5. The calculation for the BBC- and the BBL-type require computing the water vapor pressure inside the stomata and in the air. The calculation of net carbon dioxide concentration rate is the same for the BBC- and the BBL-type, only e_s and r_s , respectively, have to be used. The implementation of the JS-type requires a complete new coding of the stomatal conductance code. If the JS-type is chosen, the physiological parameters (O') are required for calculating the stress functions ($f(PAR)$, $f(T_{leaf})$, $f(\delta e)$, and β_t). To avoid code instabilities, the stomatal resistance has an upper bound of 20000 (sm^{-1}).

The stress function for leaf temperature $f(T_{leaf})$ (Equation 2.25) in the JS-type is replaced

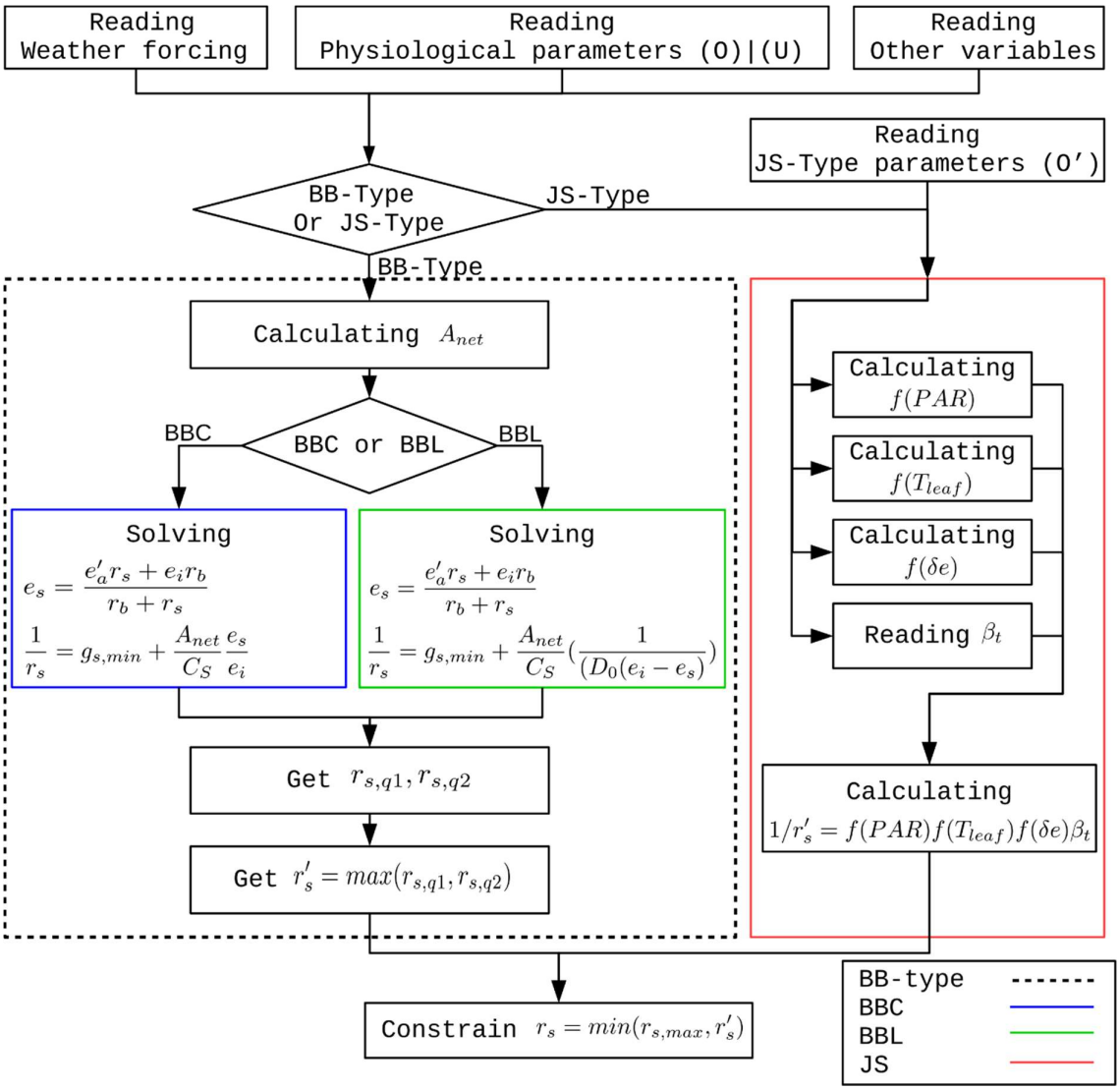

Figure 3.3. schematic of implemented BBL and JS codes in CLM3.5.

by the seasonal stress function F_{sea} (Equation 2.43). The soil temperature T_g in the equation for F_{sea} is replaced by the leaf temperature T_{leaf}, which is constrained to 298±25 K. When T_{leaf} is at 298 K, $f(T_{leaf}) = 1$. This replacement is based on the quadratic function of Dickinson *et al.* (1991), which is as a well-accepted simpler form of Equation 2.25 (Noilhan & Planton, 1989; Jacquemin & Noilhan, 1990; Dickinson *et al.*, 1993b; Niu *et al.*, 2011). The stress function for the vapor pressure deficit $f(\delta e)$ (Equation 2.26) and for the soil water stress

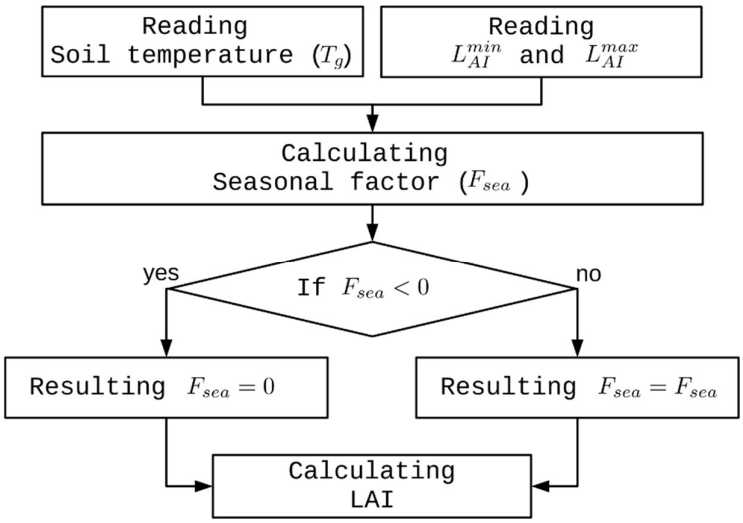

Figure 3.4. Schematic of TLAI code in CLM3.5.

deficit $f(\theta_w)$ (Equation 2.32) in the JS-type are replaced by Equation 2.38 (Leuning, 1995) and Equation 2.48 (Niu *et al.*, 2011), respectively. These replacements are often used in LSMs (Kowalczyk *et al.*, 2006; Niu *et al.*, 2011; Best *et al.*, 2011; Kauwe *et al.*, 2015).

3.4.2 Implementation of a simple dynamic LAI

The code structure of the simple dynamic LAI is based on Equation 2.42 and Equation 2.43 with soil temperature, maximum LAI and minimum LAI is illustrated in **Figure 3.4**. The implemented code determines seasonal factor form the input parameters and soil temperature. The LAI is calculated when $F_{sea} < 0$. The soil temperature at 1.04 m (7th soil layer) changes slowly with the season and is used in Equation 2.43. The maximum and minimum LAI of each plant type following the land cover classification of MODIS are the 90 and 10 percentile of the yearly averaged MODIS LAI over 10 years, respectively (for MODIS LAI see Section 3.6 .

3.5 Validation methods

The simulations with CLM3.5 are evaluated with observations using the index of agreement and Taylor diagram. The index of agreement quantifies the resemblance of the simulation results with observations as a single index. Taylor diagram visualizes and compares multiple

simulation results simultaneously.

The Index of Agreement

The Index of Agreement (IoA) (Legates & McCabe, 1999) quantifies the accuracy of simulated results against observed data:

$$IoA = \frac{\sum_{t=1}^{N}(O_t - \bar{O})^2 - \sum_{t=1}^{N}(P_t - O_t)^2}{\sum_{t=1}^{N}(O_t - \bar{O})^2} \quad (3.1)$$

$\bar{O}$ indicates the averaged observations. P_t and O_t indicate the actual values of simulations and observations at time step t, which is hourly in this thesis. When IoA equals 1, each simulated value P_t is exactly the same as its observational counterpart O_t. IoA > 0 indicates some skill while IoA < 0 indicates a bad performance of the simulations.

Taylor diagram

Taylor diagrams (Taylor, 2001) employs a polar graph to illustrate the relationship between simulations and observations (**Figure 3.5**). The radius of the plot is scaled with the ratio of the standard deviation of the simulations with respect to the observations. The angle on the plot is scaled by the correlation between observations and simulations. Thus, each comparison is

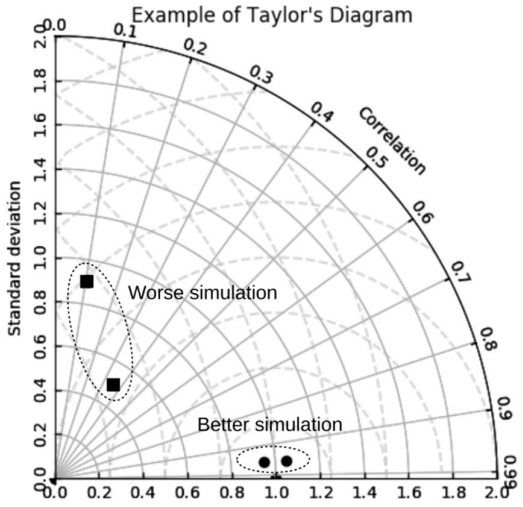

Figure 3.5. An example of Taylor diagram.

quantified by two values, which define one point on the Taylor diagram; thus multiple comparisons can be easily compared. The observations, with which simulations are compared are indicted by a triangle at relative standard derivation and correlation equal to 1.

3.6 Study location and input data

Our study locations are in the Rur catchment (**Figure 3.6**) at the western border of Germany for which observations are provided by the SFB/TR32 project (Vereecken *et al.*, 2010; Simmer *et al.*, 2015). The northern part is a plain area dominated by agriculture, while the mountainous southern part is dominated by forest and grassland. The four observation sites used in this thesis are Selhausen (SE), Merzenhausen (MZ), Rollesbroich (RO), and Wüstebach (WU), which are dominated by crops (Potato in 2012 and winter wheat in 2013), crops (winter wheat), grassland (C3 grass), and needle-leaf evergreen forest (Pinus), respectively. Crop is harvested in specific month at the SE and MZ sites, and grass is mown two to three times per year at the RO site. The vegetation height is dynamic at these three sites but static at the WU site which is covered with mature forest. The weather data at the SE, MZ, and RO sites are measured at the respective sites. The weather data at the WU site is incomplete and thus substituted by the observations at the weather station Schöneseiffen, which is 3.5 KM away from the WU site and described by Graf *et al. (2014).* In this thesis, we compare simulations

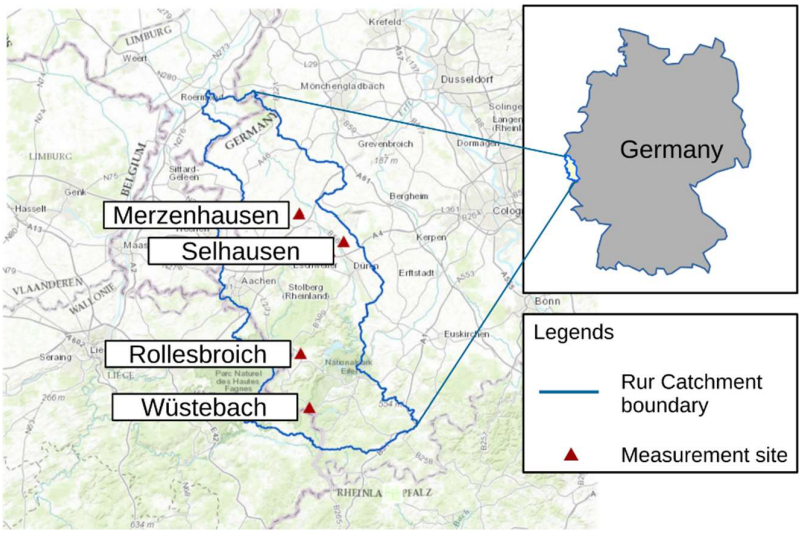

Figure 3.6. Location of the Rur catchment and the four measurement sites (SE, MZ, RO, and WU) (map source: TR32 web GIS (http://www.tr32db.uni-koeln.de/webgis3/)).

for the years 2012 and 2013.

Heat fluxes at the sites are measured by eddy covariance (EC) fluxes stations. Observations include net radiation, latent heat flux, sensible heat flux, ground heat fluxes, soil water content, and soil temperature in 30 minutes time step. Soil moisture observations are acquired hourly from a wireless network at the depths of 5, 20, and 50 cm (RO and WU) and from a soil probe (Hydra Probe II) attached to EC-flux station at 2 cm depth (SE and MZ). The observed heat fluxes and soil moisture are used for validating the model performance. Realistic land surface, subsurface, and meteorological forcing data are used to drive TerrSysMP.

Soil properties are provided from two sources: the digital soil map of the world from Food and Agriculture Organization of the United Nations (FAO), and the subsurface permeability information from Gleeson *et al.* (2011). The digital soil map has a better horizontal resolution (2500 m) than the subsurface permeability information map (>5000 m), but only support an effective depth of 100 to 150 cm. The Digital Soil Map covers 2.5 m soil depth, which corresponds to all ten soil layers in CLM3.5 and the upper ten soil layers in Parflow.

MODIS LAI, re-analyzed from the MODIS product (MCD15A2), has a temporal resolution of eight days and a spatial resolution of 1 km. In the MODIS product, each grid element (1 km by 1 km) is assigned a LAI value. Each grid element is also assigned a plant type based on the land cover condition map from MODIS Land Cover Dynamic Data (MCD12Q2). The grids of MCD15A2 and MCD12Q2 do not match; hence a re-mapping is performed to assign each grid a LAI value and a land cover condition. During the winter time, the MODIS LAI of evergreen trees is too low due to albedo of snow and thick clouds, while evergreen plants maintain high LAI during the winter time. Hence, the MODIS LAI of needle-leaf and broad-leaf trees are corrected by following Tian *et al*. (2004) and Lawrence and Chase (2007). The monthly average MODIS LAI curve is used as the input in CLM3.5 and PF-CLM3.5.

Chapter 4

Impact of vegetation uncertainties on LSM

The effect of physiological parameters from different authors on stomatal conductance is discussed in Section 4.1. The simulated stomatal conductance and canopy conductance are discussed in Section 4.2. Then the simulation results with the three stomatal conductance equations and the two LAI input types are compared against observed heat fluxes and soil moisture in Section 4.3 and 4.4, respectively.

4.1 Evaluation of the effects of different physiological parameters

4.1.1 Effect of different physiological parameters on stomatal conductance

Two sets of physiological parameters, the original physiological parameter (O) and the updated physiological parameter sets (U), are used. **Figure 4.1** compares the simulated hourly stomatal resistance (r_s) and stomatal conductance (g_s) from both parameter sets. The units of the BB-type stomatal conductance are μmol m^{-2} s^{-1}, while the units of the JS-type stomatal conductance are m s^{-1} (see Section 2.4.1). The units of the BB-types stomatal conductance in the results are converted to m s^{-1} by the ideal gas equation in the CLM3.5 code. In **Figure 4.1 (a)**, r_s values are shown as monthly results from January to December. Net radiation ranges from -100 to 700 W m^{-2} between night and day. r_s decreases with increasing R_{net} and approaches its minimum when R_{net} is larger than 100 W m^{-2}. The minimum r_s(O) is at 500 s m^{-1} while the minimum r_s(U) is at 200 s m^{-1}. g_s increases with R_{net} (**Figure 4.1 (b)**). g_s is shown only for January, April, July, and October to demonstrate its seasonal change. In July, g_s(O) reaches its maximum at about 0.008 ms^{-1} and then slightly decreases with a further

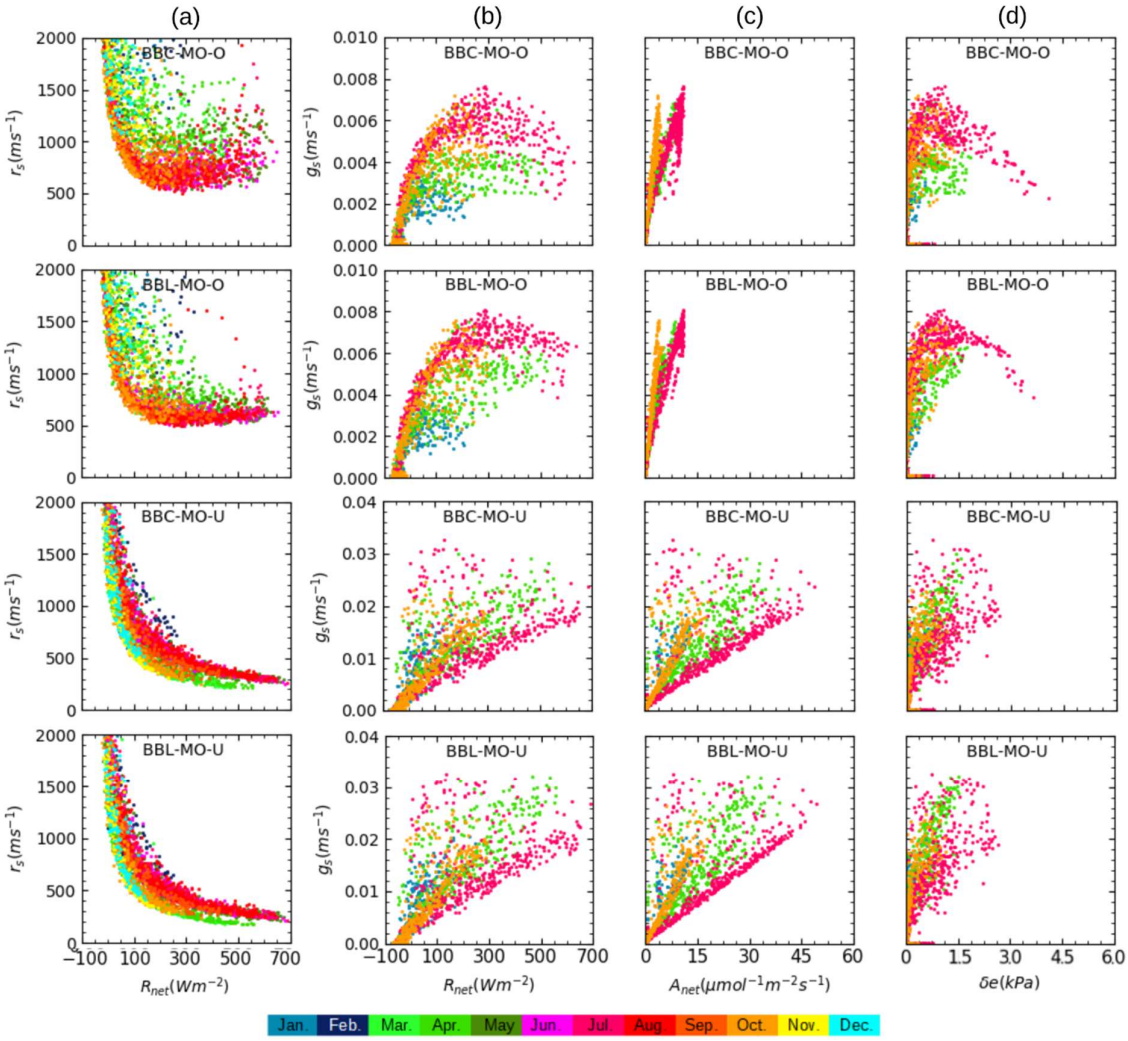

Figure 4.1. Hourly simulated stomatal resistance against net radiation (a), stomatal conductance against net radiation (b), net CO_2 assimilation rate against net radiation (c), and humidity deficit against net radiation (d) at the MZ site for the year 2012.

increase of R_{net} consistent with the observed stomatal behaviour. g_s (U) approaches a maximum of about 0.03 ms^{-1} with increasing R_{net} and are closer to observed stomatal conductance values (Granier *et al.*, 2000; Li *et al.*, 2005). g_s(O) is larger in summer and autumn and smaller in spring and winter. For g_s(U) such clear seasonal changes are not observed.

In Equation 2.36 (BBC) and 2.40 (BBL), g_s is proportional to A_{net}. As shown in **Figure 4.1 (c)**, g_s increases as A_{net} increases. Both, the maximum of A_{net}(O) and of A_{net}(U) are larger in July than in January because photosynthesis is stronger during the growth season. A_{net}(O) and A_{net}(U) reach the maximum of around 10 µmol m^{-2} s^{-1} and around 50 µmol m^{-2} s^{-1} in July,

respectively.

During night time, the humidity deficit is very small, and stomatal conductance approaches zero. With increasing incoming solar radiation, stomatal conductance first increases as the humidity deficit increases. With further increases of the humidity deficit stomatal conductance decreases again. This behaviour is found in **Figure 4.1 (d)** for g_s(O) in the summer time but not for g_s(U). The unclear behaviour of g_s(U) against humidity deficit in summer time is similar to the results in **Figure 4.1 (b)**.

The behaviour of g_s(TL) is similar to the behaviour of g_s(MO), and thus these results are not shown. The behaviour of g_s(O) is described better than g_s(U) since the behaviour of g_s(O) against R_{net} and A_{net} are closer to observation and theory (Jarvis, 1976; Wang & Leuning, 1998). Overall, the different physiological parameter sets lead to quite different results of g_s but are insignificantly different between the different BB-type stomatal conductance equations.

4.1.2 Impact of different physiological parameters on model performance

Table 4.1. IoA of the simulated results obtained from simulations with the BBC-type and the BBL-type stomatal conductance equations with the original physiological parameters (O) and the updated physiological parameter sets (U) at the Merzenhausen (MZ) site for the year 2012..

	R_{net}	λE	H	T_g
BBC-MO-O	0.72	0.04	0.12	0.91
BBL-MO-O	0.72	0.14	0.07	0.91
BBC-MO-U	0.84	0.41	-0.10	0.91
BBL-MO-U	0.84	0.43	-0.13	0.91
BBC-TL-O	0.73	0.26	0.19	0.93
BBL-TL-O	0.73	0.34	0.12	0.93
BBC-TL-U	0.84	0.46	0.13	0.94
BBL-TL-U	0.84	0.48	0.09	0.94

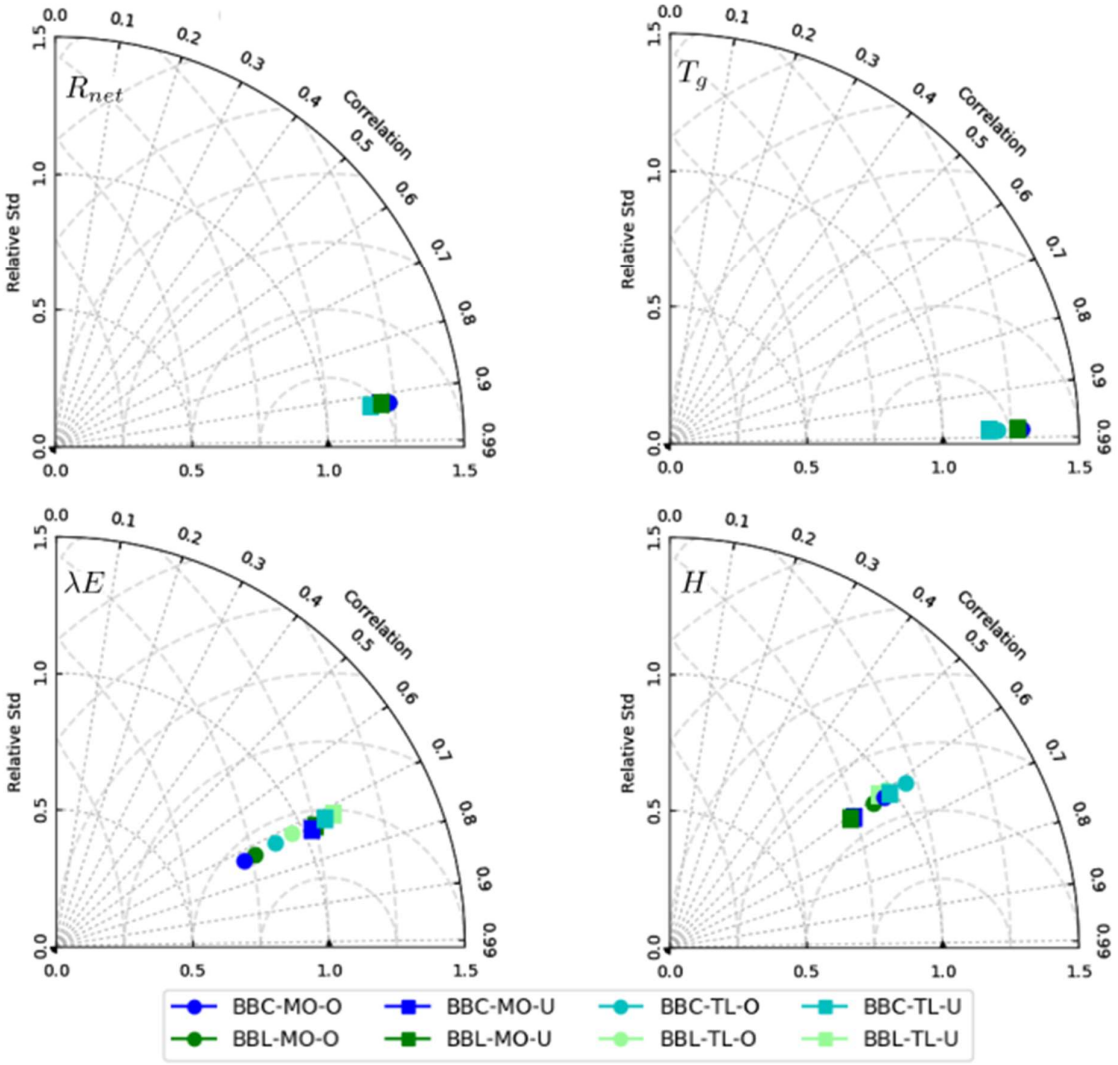

Figure 4.2. The Taylor diagram of the simulated results by the BBC-type and the BBL-type stomatal conductance equations with the original physiological parameter set (O) and the updated physiological parameter set (U) at MZ site for the year 2012. Net radiation, ground temperature, latent heat flux, and sensible heat flux results are calculated from hourly data.

The predicted net radiation (R_{net}), latent heat flux (λE), sensible heat flux (H), and ground temperature (T_g) are compared against observations using the index of agreement (IoA) and Taylor diagrams (**Table 4.1** and **Figure 4.2**). The IoA for T_g are highly independent of the chosen physiological parameter sets or stomatal conductance equations. The Taylor diagrams show similar results. The IoA of R_{net} is somewhat lower for the original (O) compared to the updated parameter set (U) and not affected by different stomatal conductance equations, as expected.

The small differences are also evident from the Taylor diagrams. The latent heat fluxes are much better reproduced by the simulations with the updated parameter set according to the IoA. This is also reflected by the Taylor diagram, where the relative standard deviations increase for the updated parameter set. And this holds for both the BBC-type and the BBL-type stomatal conductance equations. These results are consistent with Sulis *et al.* (2015), who also observe that H(U) are underestimated during the night time, which is also observed in our results (see IoA and the Taylor diagrams).

The simulations of parameter uncertainty are performed at MZ and SE sites in 2012 and 2013. The results of g_s have similar behaviour to the results at MZ site in 2012. The results of IoA and Taylor diagram show the improvement by employing updated parameter set. Therefore, those results are not shown redundantly. The results at SE site in 2012 is excluded since it was planted with potatoes, for which no updated physiological parameter set is yet available. The results at MZ and SE sites in 2012 and 2013 show a comprehensive evidence of the improvement for the latent heat flux by the updated physiological parameter set.

4.2 Evaluation of different stomatal conductance equations and different LAI inputs

In the following we present LSM simulations at the four measurement sites (SE, MZ, RO, and WU) for the years 2012 and 2013. The simulations with the BB-type equations are performed with the original physiological parameter set because updated physiological parameter set is not available for C3 grass (RO site) and evergreen needle-leaf forest (WU site). The results at the grass site Rollesbroich (RO) is firstly discussed assuming a constant vegetation cover. The results at MZ site (winter wheat) and SE site (potato) include a partly human-managed vegetative cover including seeding, irrigation, harvesting, and fertilization. At the forested Wüstebach site (WU) a constant vegetation cover is assumed.

4.2.1 Difference between stomatal conductance equations

In the following, the suffixes (BBC), (BBL), and (JS) mark the employed stomatal conductance equations. According to Equations 2.36 and 2.40 g_s(BBC) and g_s(BBL) depend on a given

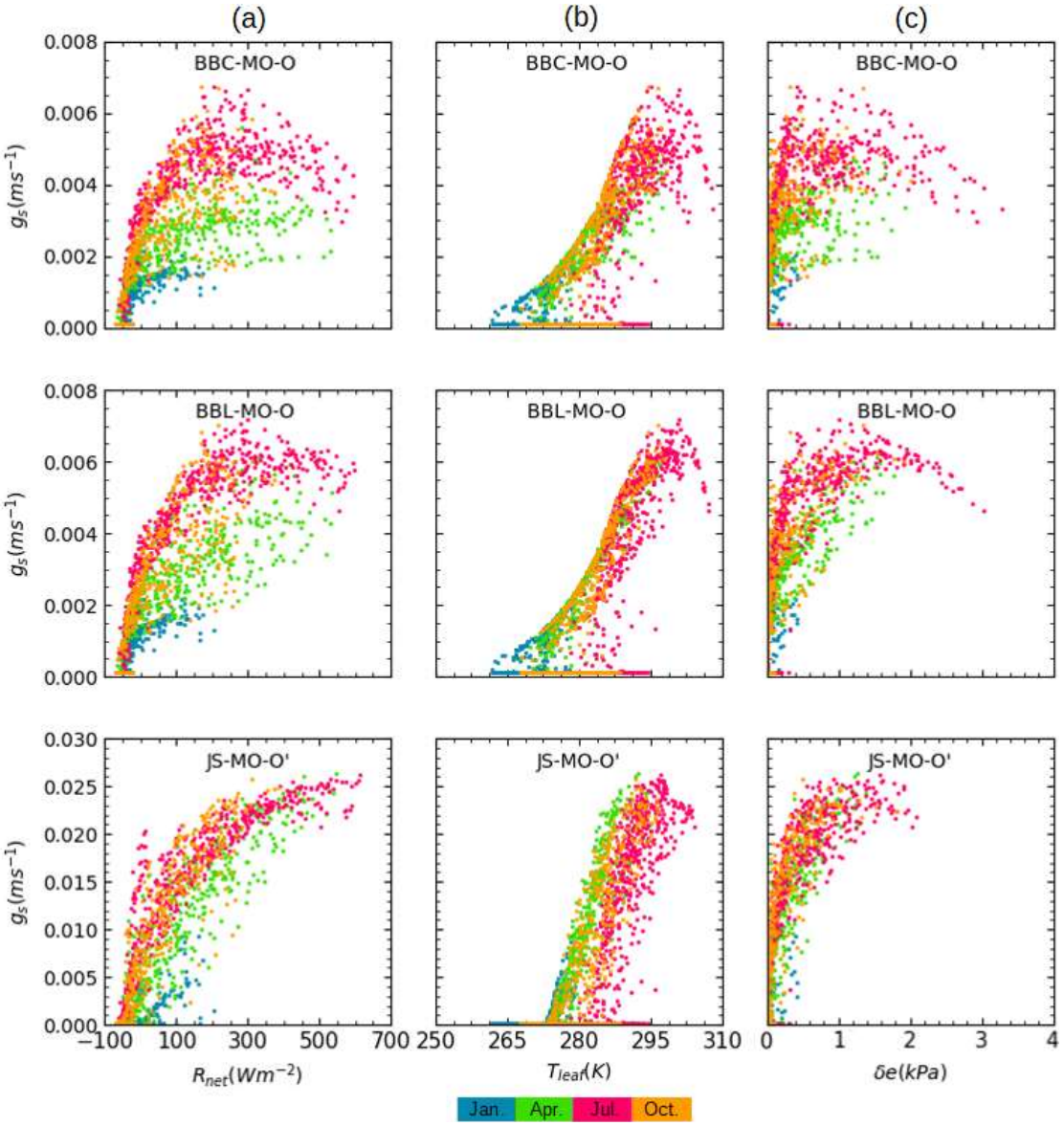

Figure 4.3. Hourly stomatal conductance (g_s) against (a) net radiation, (b) leaf temperature and (c) humidity deficit at the grassed Rollesbroich site (RO) for the year 2012. Three stomatal conductance equations (the BBC-type, the BBL-type, and the JS-type) with MODIS LAI data are compare against each other.

$g_{s,min}$ and increase mainly by $A_{net}H_R$ and $A_{net}f(\delta e)$, respectively (**Figure 4.1 (c)**). g_s(JS) is based on a given $g_{s,max}$ and reduced by stress functions (Equation 2.29). Accordingly, the maxima of g_s(BBC) and g_s(BBL) are variable while the maximum of g_s(JS) is predefined. The maxima of g_s(BBC) and g_s(BBL) are 0.007 ms^{-1} and thus much lower than the predefined

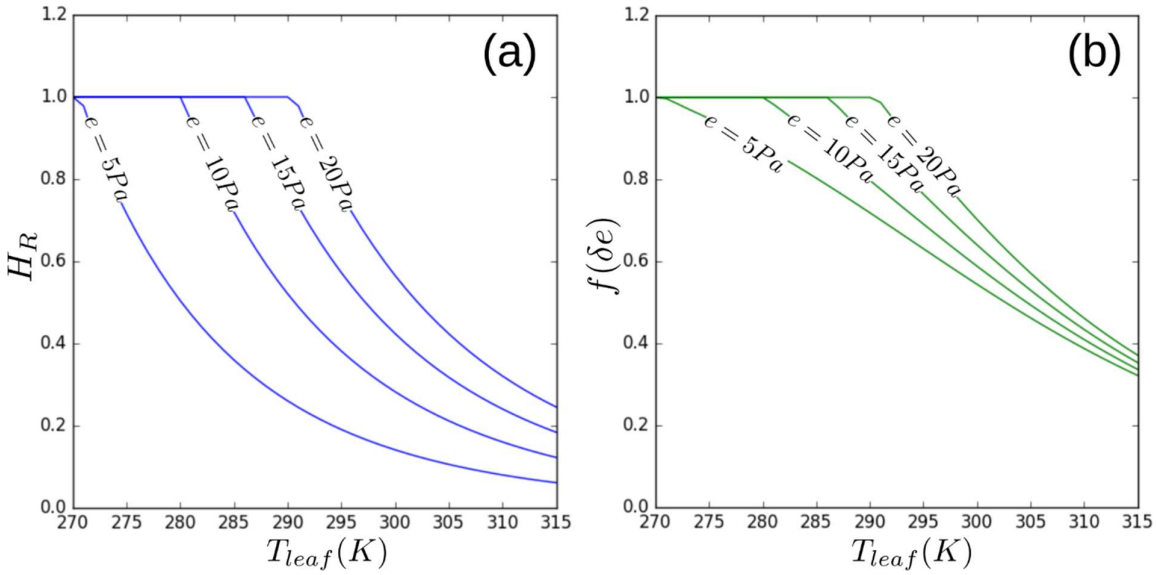

Figure 4.4. (a) Relative humidity (H_R) and (b) function of vapor pressure deficit ($f(\delta e)$) against leaf temperature for different vapor pressures (from 5 Pa to 20 Pa).

maximum g_s(JS) of 0.026 ms^{-1} (**Figure 4.3**). According to the observed stomatal conductance from Van Wijk *et al.* (2000), Granier *et al.* (2000), and Li *et al.* (2005) the maximum g_s(JS) better fits the observation than the maxima of g_s(BBC) and g_s(BBL). g_s(BBC) and g_s(BBL) depend on A_{net} which is controlled by photosynthesis and affected by PAR (absorbed photosynthetically active radiation) and leaf temperature, which vary with season. Hence g_s(BBC) and g_s(BBL) show seasonal variations as observed in **Figure 4.3**.

The difference between the BBC- and BBL-type equations is the impact of humidity on stomatal conductance; they employ relative humidity H_R(Eq. 2.39) or vapor pressure deficit function $f(\delta e)$(Eq. 2.38), respectively. The behaviour of H_R and $f(\delta e)$ are shown in **Figure 4.4**. Both decrease with increasing leaf temperature, which leads to similar stomatal conductance (**Figure 4.3)**. H_R decreases, however, more rapidly with increasing leaf temperature than $f(\delta e)$. Therefore, g_s(BBC) decreases faster with leaf temperature than g_s(BBL) (**Figure 4.3 (b))**. Since the theoretical concept of the JS-type equations is different from the one of the BB-type type equations, g_s(JS) more strongly differ from g_s(BBC) and g_s(BBL). The maximum A_{net} is achieved at 298 K in the BB-types, as is the stress function for leaf temperature (Section 3.4.1) in the JS-type. Thus g_s is maximum at 298K in all three stomatal conductance equations

(**Figure 4.3 (b)**). In the JS-type equation, the simulated stomatal conductance is zero (no conductance) when the leaf temperature is below 273 K or over 323 K.

As mentioned in Section 4.1 the relationship between incoming solar radiation and humidity deficit affects the behaviour of stomatal conductance; hence during summer g_s decreases after a maximum for the BB-type equations (**Figure 4.3 (c)**), which is not prominent for g_s(JS).

Both SE and MZ sites are located in a crop plane with higher air temperatures and less humidity compared to the grassland RO site located in a hillier area. Therefore, SE and MZ sites have larger humidity deficits. Following **Figure 4.4**, the difference between H_R and $f(\delta e)$ is larger in drier or hotter condition. Hence the differences between g_s(BBC) and g_s(BBL) is larger at the MZ and SE sites than that at RO site despite their similar characteristics. g_s at the forested WU site (evergreen needle-leaf forest) is also similar to the RO site but smaller. The maxima of g_s(BBC), g_s(BBC), and g_s(JS) are 0.005 ms^{-1}, 0.006 ms^{-1}, and 0.01 ms^{-1}, respectively. The differences between g_s for the different vegetation types is most prominent when the grass site (Stewart & Verma, 1992; Ronda *et al.*, 2001) is compared to the forest site (Stewart, 1988). Because the behaviours of g_s at SE, MZ, and WU sites are similar to the behaviour of g_s at RO site, the results at SE, MZ, and WU sites are not shown. The simulations with the six simulation modes are also performed in 2013 and show similar results (not shown).

4.2.2 Canopy conductance

Vegetation affects the land-atmospheric interaction by the whole canopy, and hence canopy conductance g_c, which depends on stomatal conductance and LAI ($g_c = g_s \cdot L_{AI}$), is investigate (Dickinson *et al.*, 1991). Two LAI inputs, MODIS and TLAI, are employed for comparison. MODIS provides LAI data for every 8-days from which a monthly mean LAI is estimated. **Figure 4.5** compares the LAI from MODIS with the simulated TLAI against in-situ measured LAI, however for only four months (from 2nd of May to 26th of August in 2016) by TR32 (unpublished data from A. Graf). No in-situ measured grass LAI exist for 2012, unfortunately. **Figure 4.6** illustrates the results for canopy conductance g_c against net radiation R_{net}, leaf temperature T_{leaf}, and humidity deficit δe calculated by the BBL- and the JS-type equations. Because the results employing the BBC- and BBL-type equations are similar,

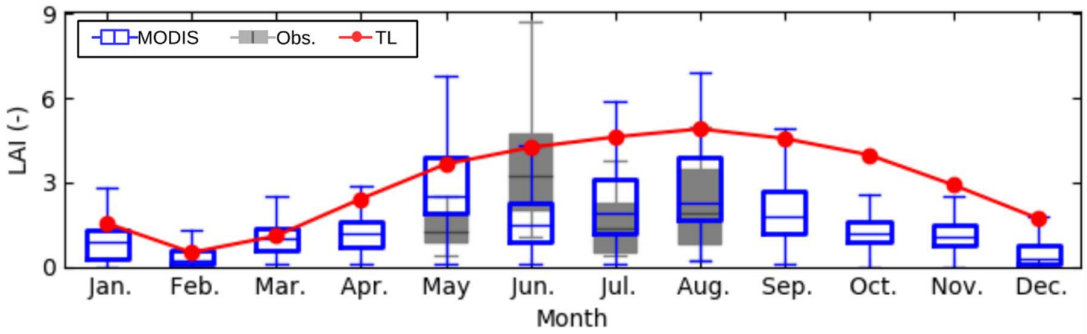

Figure 4.5. The blue boxplot shows monthly LAI from MODIS at the grass site Rollesbroich in 2012. The red line shows monthly TLAI at the same site in 2012. The grey boxplots show the in-situ measured LAI at that site in 2016. The middle line in the boxplot is the average of the LAI and the upper box and lower box boundaries represent the 25 and 75 percentiles of LAI, respectively.

only the BBL-results are shown. As shown in **Figure 4.5 (a)**, The values of TLAI are about twice of the MODIS LAI; thus g_c(BBL-TL) and g_c(JS-TL) are also about twice of g_c(BBL-MO) and g_c(JS-MO), respectively. g_c (JS) plotted against R_{net} shows a clear seasonality because of the seasonality of the LAI (**Figure 4.6 (a)**), which is similar for g_c(BBC) and g_c(BBL). g_c against T_{leaf} and δe is behaves similar to the results for g_s. Hence, the LAI generates the seasonal effects on canopy conductance, and the stomatal conductance determines the behaviour.

The vegetation types at the crop sites Selhausen (SE) and Merzenhausen (MZ) and at the C3 grass site Rollesbroich (RO) have similar physiological parameters and accordingly lead to similar results for g_c. However, winter wheat at MZ and potatoes at SE were harvested in August and September, respectively, as shown in **Figure 4.7 (a)**. Since the areas of the measurement sites are around 300 x 300 m and the resolution of MODIS LAI being much coarser (1 km by 1 km) the in-situ observed rapid LAI reduction cannot be observed by the satellite. Thus we modified the MODIS LAI is to 0.6 after harvesting following *Shrestha et al.* (2015). The drop is, however smoothed to occur over two months to avoid instabilities of the code (**Figure 4.7 (b)**). Thus the g_c(MO) decreases rapidly in October (**Figure 4.8**). The MODIS LAI at SE site is modified by the same method, leading to results similar to the MZ site.

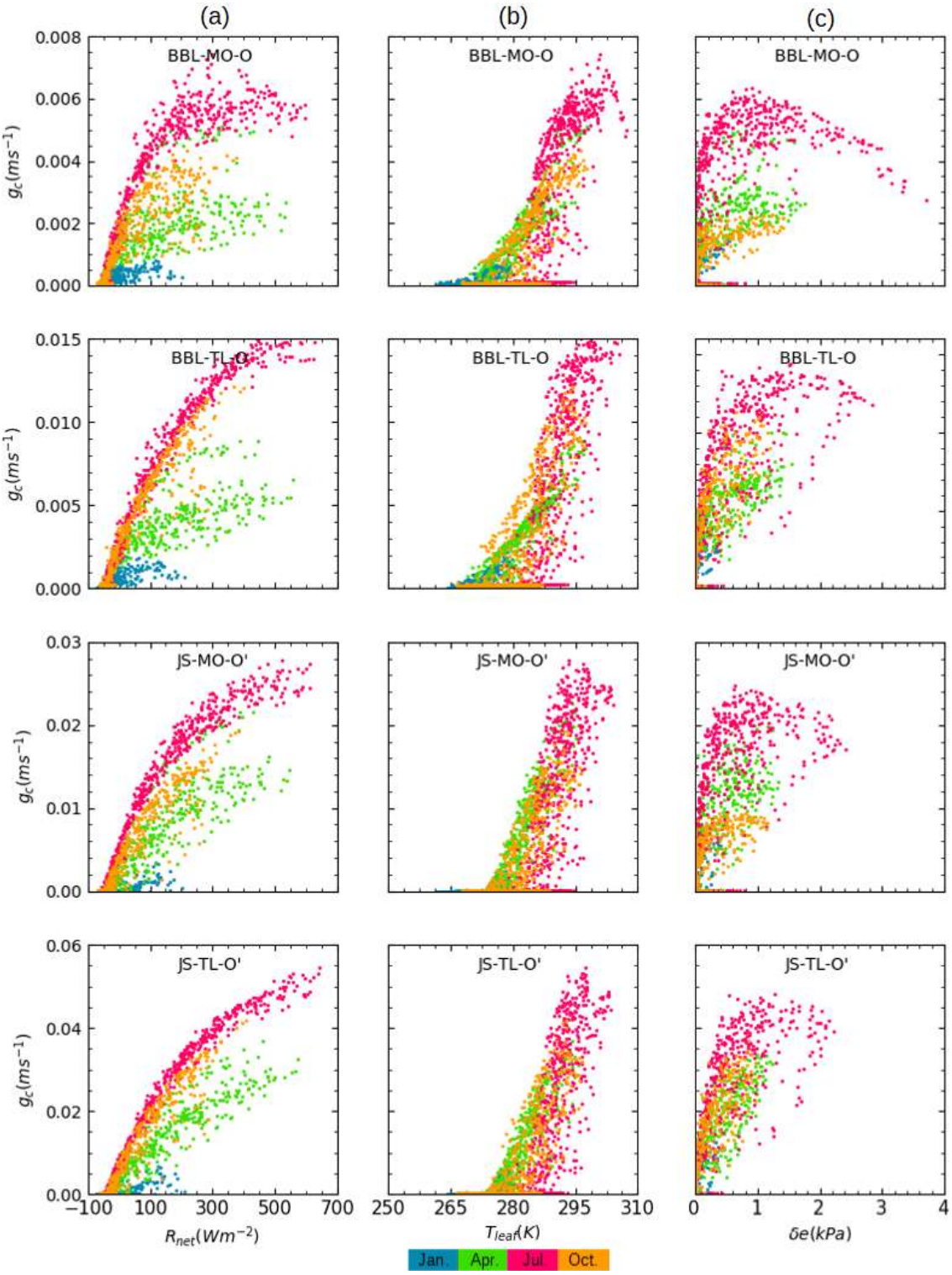

Figure 4.6. Hourly canopy conductance (g_c) against (a) net radiation, (b) leaf temperature and (c) humidity deficit at the Rollesbroich (RO) grassland site for the year2012. Two stomatal conductance equations (the BBL-type, and the JS-type) with two LAI input types (MODIS LAI and TLAI) are employed and compared.

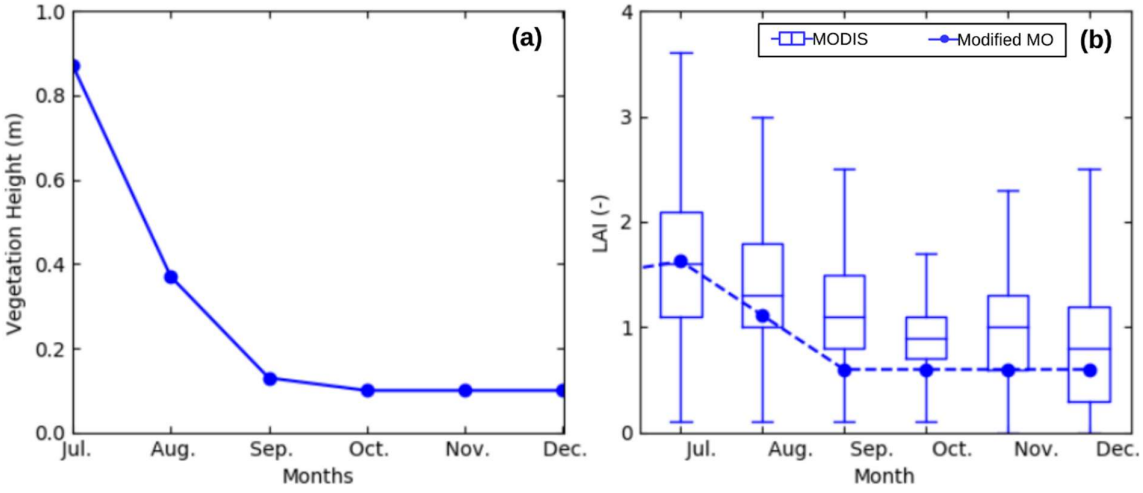

Figure 4.7. (a) Monthly average vegetation height of winter wheat from measurement at the MZ site in 2012. (b) The boxplot shows the MODIS LAI and the dashed line shows the modified LAI at the crop site in 2012.

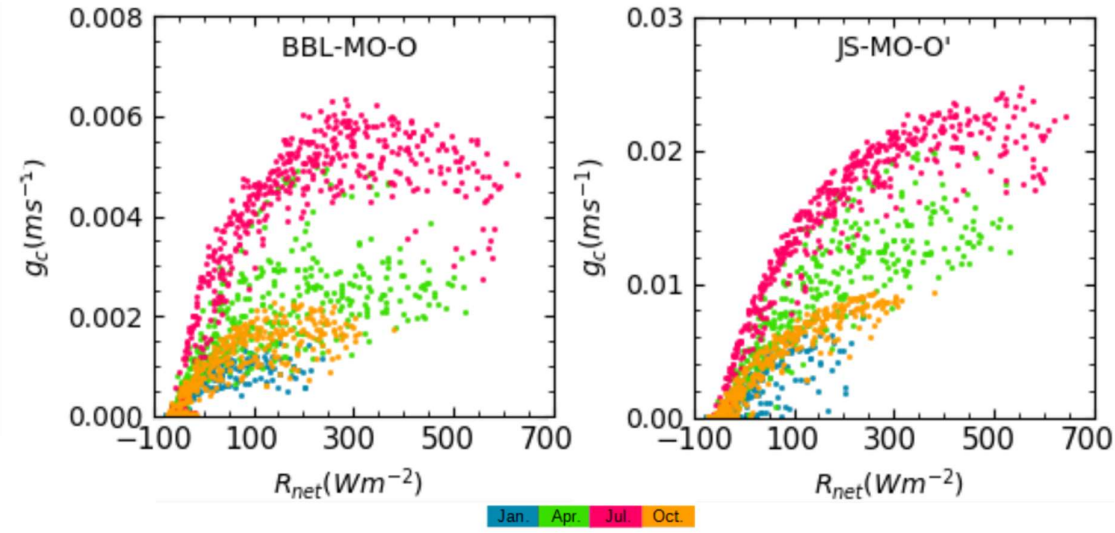

Figure 4.8. Hourly canopy conductance (g_c) against net radiation at the MZ site, 2012. Two stomatal conductance equations (the BBL-type, and the JS-type) with MODIS LAI are employed and compared against each other.

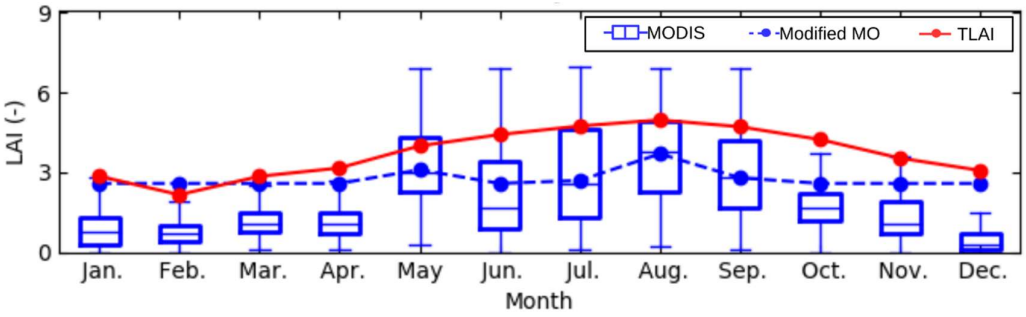

Figure 4.9. The blue boxplots show monthly MODIS LAI at the evergreen needle-leaf tree site Wüstebach in 2012. The middle line in the boxplot is the average of MODIS LAI and the upper box and lower box represents 25 and 75 percentile of MODIS LAI, respectively. The red line with dots shows the monthly TLAI.

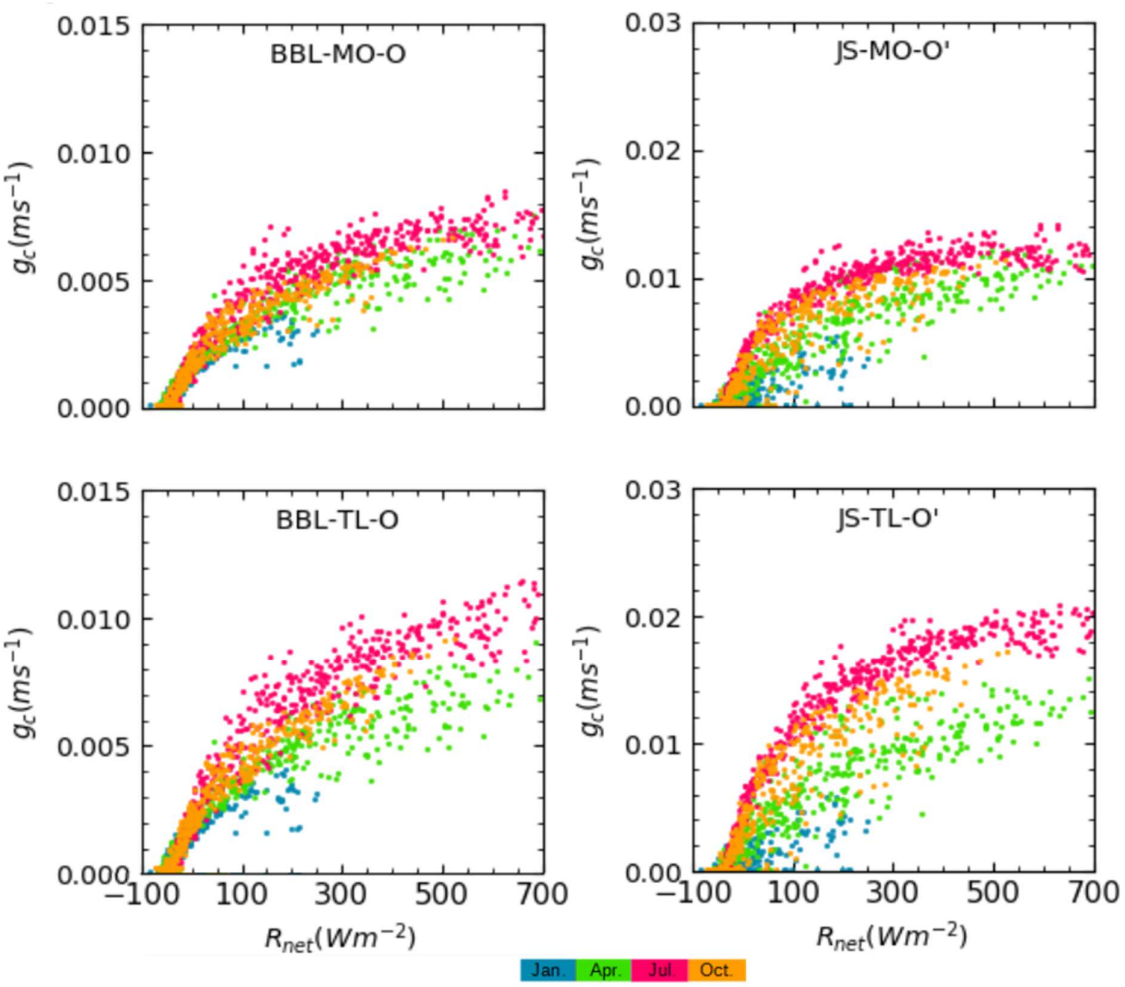

Figure 4.10. Hourly canopy conductance (g_c) against net radiation at the forested Wüstebach (WU) site in 2012. Two stomatal conductance equations (the BBL-type, and the JS-type) with two LAI input types (MODIS LAI and TLAI) are employed and compared.

At the forested Wüstebach site, the MODIS LAI is also modified due to the underestimation by satellite measurement (see discussion in Section 3.6 When the monthly average MODIS LAI is below 70% of the maximum monthly average (in August), the LAI value is modified to 70% of the maximum monthly average MODIS LAI (Tian *et al.*, 2004; Lawrence & Chase, 2007) (**Figure 4.9**). The amplitude of TLAI is larger than that of the modified MODIS LAI, and hence the seasonality of g_c(TL) is larger than that of g_c(MO) (**Figure 4.10**). Generally, the behaviour of g_c at the WU site is similar to that at RO site, but has a lower seasonality.

4.3 Effects of different vegetation schemes on states and fluxes of the land surface

In this section, we investigate how the different implemented vegetation subschemes in CLM3.5 affect the LSM simulations, i.e. the exchange fluxes of latent heat and sensible heat, net radiation, Bowen ratio, and the ground temperature, and how the simulations compare to observations. The results at the Rollesbroich grassland site (RO) are discussed first followed by the crop sites Merzenhausen and Selhausen (MZ, SE), and the forest site Wüstebach (WU).

4.3.1 Results for the Rollesbroich grassland site

The general annual cycle of latent heat flux (λE) simulated by the different stomatal conductance equations and the different LAI input types is similar compared with the observations, but absolute values can be very different (**Figure 4.11 (a)**). The results for λE from the Jarvis-Steward model with dynamic LAI evolution based on the ground temperature (JS-TL) is closest to the observed values λE(OBS). The six simulation modes differ during day time (stomata opening) and approach each other during night time (stomata closing) (**Figure 4.11 (b)**). The total latent heat flux is consists of transpiration λE_T, the latent heat flux from intercepted water λE_C, and the latent heat flux from the ground λE_G; λE is mainly dominated by λE_T (**Figure 4.11 c-e**). According to Equation 2.8, λE is inversely proportional to aerodynamic resistances to r_c and r_b. λE is most strongly affected by λE_T, and λE_T is affected by canopy resistance r_c, which is the reciprocal of canopy conductance g_c; thus λE is dominated by g_c, which is affected by different stomatal conductance equations and the LAI

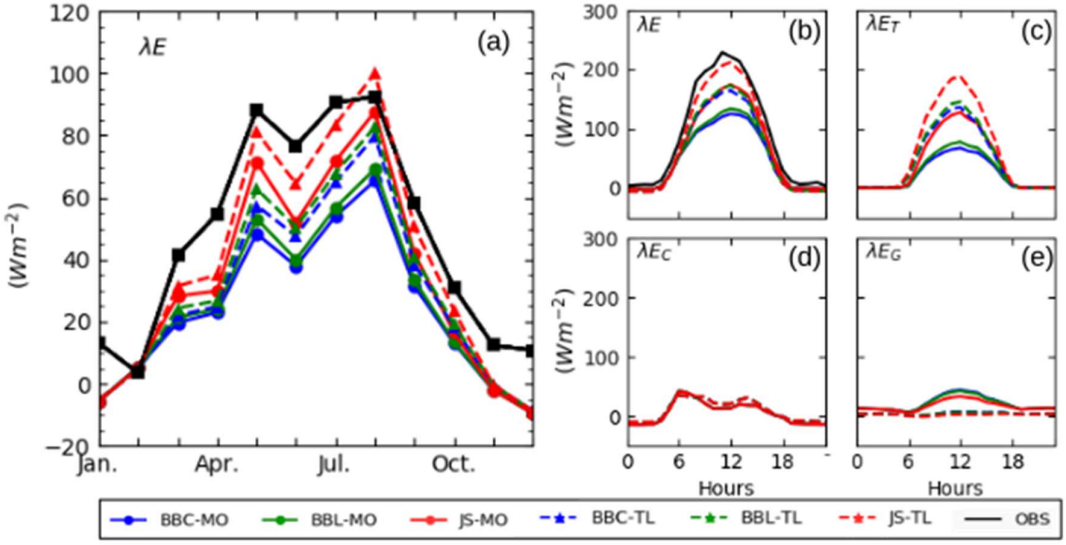

Figure 4.11. (a) The monthly average curves and (b) average daily cycles of latent heat flux from simulations and observation (OBS) at the Rollesbroich grassland site for the year 2012. The average July daily cycles of (c) transpiration λE_T, (d) latent heat of intercepted water from the canopy λE_C, and (e) latent heat flux on the ground λE_G are shown on the right-hand side sub-plots.

(**Figure 4.11 (c)**). The higher values of λE_T (JS-TL) are produced by the higher g_c (JS-TL) following from its higher stomatal conductance and LAI,. λE_C is calculated as the amount of water evaporated from leaves through the leaf boundary layer resistance (r_b). According to Equation 2.14 and Equation 2.15, E_C is affected by the water storage in canopy (S_{canopy}), which is affected by LAI, and hence λE_C is affected by LAI. This phenomenon can be observed in **Figure 4.11 (d)**. λE_G is determined by the resistance to water vapor (r_{aw}). According to aerodynamic resistance theory (**Figure 2.2 (c)**), r_{aw} is affected by r_c under the same energy input condition (i.e. the same incoming solar radiation). Therefore, λE_G is significantly affected by g_c (**Figure 4.11 (e)**).

The simulated sensible heat fluxes are also affected by the stomatal conductance equations and LAI input types, but the stomatal conductance equations dominate the simulation results (**Figure 4.12 (a)**). The general behaviour of sensible heat fluxes predicted by six simulation modes are similar to each other, but the values are different. Among the results predicted by

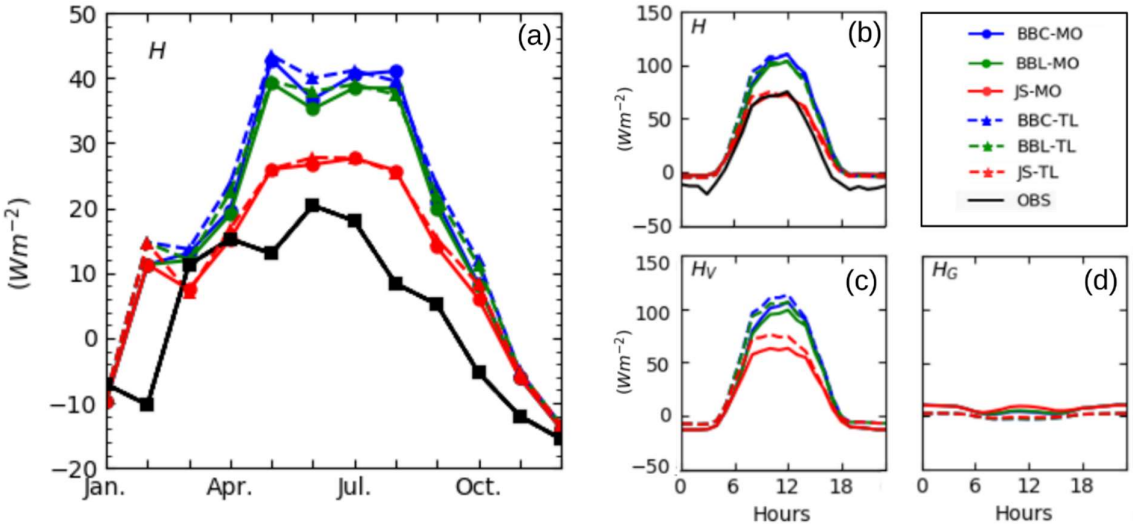

Figure 4.12. (a) The monthly average curves and (b) average daily cycles of sensible heat flux from simulations and observation (OBS) at the Rollesbroich grassland site for the year 2012. The average July daily cycles of (c) sensible heat flux on vegetative cover H_V , and (d) sensible heat flux on the ground H_G are shown on the right-hand side sub-plots.

six simulation modes, H(JS-MO) and H(JS-TL) are the closest to the H(OBS). In the daily cycles results (**Figure 4.12 (b)**), the H(JS-MO) and H(JS-TL) are very close to H(OBS) during day time, but the sensible heat fluxes predicted by all six simulation modes are overestimated at night time, which causes the overestimation of the monthly average sensible heat fluxes in **Figure 4.12 (a)** also observed by Sulis *et al.* (2015). The sensible heat flux consists of the sensible heat fluxes from the vegetation H_V (**Figure 4.12 (c)**) and from the ground H_G **Figure 4.12 (d)**), and is dominated by H_V. By Equation 2.9, H_V is affected by the temperature difference ΔT_V between leaf and air temperature ($\Delta T_V = T_{leaf} - T_{air}$) shown in **Figure 4.13 (c)**. The temperature difference influences the value and the direction of H_V. According to **Figure 4.13 (c)**, H_V is toward the atmosphere (ΔT_V is positive) over day time, and towards the vegetation (ΔT_V is negative) in the night time. The value of H_V is different for the different simulation modes. H_G is affected by the temperature difference ΔT_G between ground and air temperature ($\Delta T_G = T_g - T_{air}$) as shown in **Figure 4.13 (b)**. The observed ground temperature shows that air temperature is lower than ground temperature in the night time but higher in the daytime. In July the simulated ground temperature is always higher than air temperature

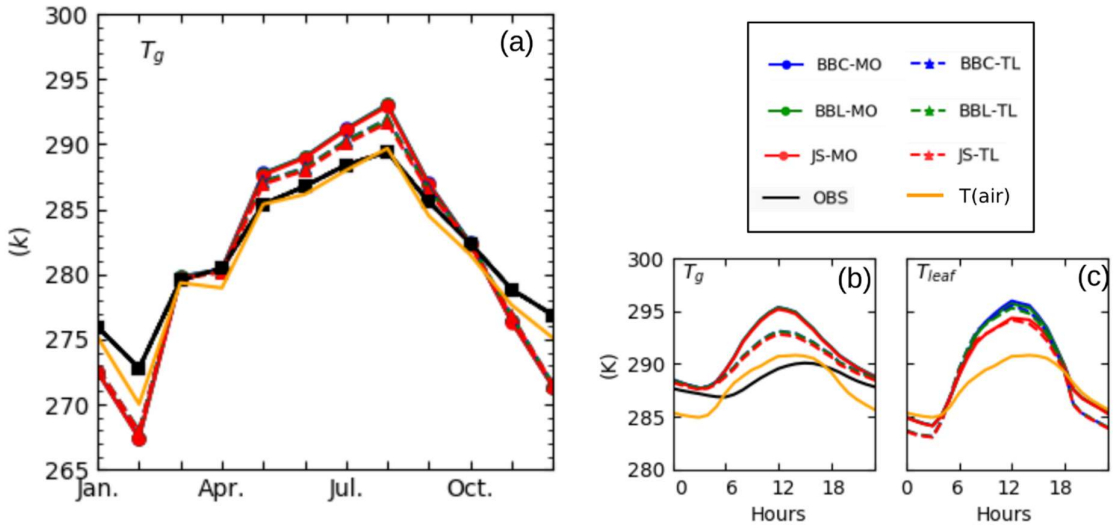

Figure 4.13. (a) The monthly average curves of ground temperature from simulations and observation (OBS) at the Rollesbroich grassland site for the year 2012. The average July daily cycles of (b) ground temperature, and (c) leaf temperature are shown on the right-hand side sub-plots.

(ΔT_G is positive) thus H_G is always directed toward the atmosphere. The simulated H_V and H_G are affected by the LAI. H_V(TL) is larger than H_V(MO), but H_G(TL) is smaller than H_G(MO) since larger vegetation cover consumes more energy for vegetation components e.g. λE_T, λE_C and H_V. Hence LAI affects H_V and H_G but not its sum.

The ground temperature is mainly affected by the LAI input types in the monthly (**Figure 4.13 (a)**) and daily cycles (**Figure 4.13 (b)**). T_g(TL) is lower than T_g(MO), especially during late spring and summer time (**Figure 4.13 (a)**). With more vegetative cover, less radiation can reach the ground (**Figure 2.1 (b)**). Hence the predicted ground temperature is inversely proportional to the predicted value of LAI. The similar effect of vegetative canopy on ground temperature is observed by Shukla & Mintz (1982).

The ground heat is not shown because of its relatively small amplitude between -20 to 30 W m^{-2}. Differences between six simulation modes are even smaller; thus uncertainties of vegetation scheme do not affect ground heat flux significantly. Hence, the net radiation mainly consists of latent and sensible heat flux (**Figure 4.14 (a)**). The behaviour of net radiation results from the six simulation modes are similar, and also similar to observation, and barely depends on the employed stomatal conductance equations. As discussed in Section 2.1, LAI affects net

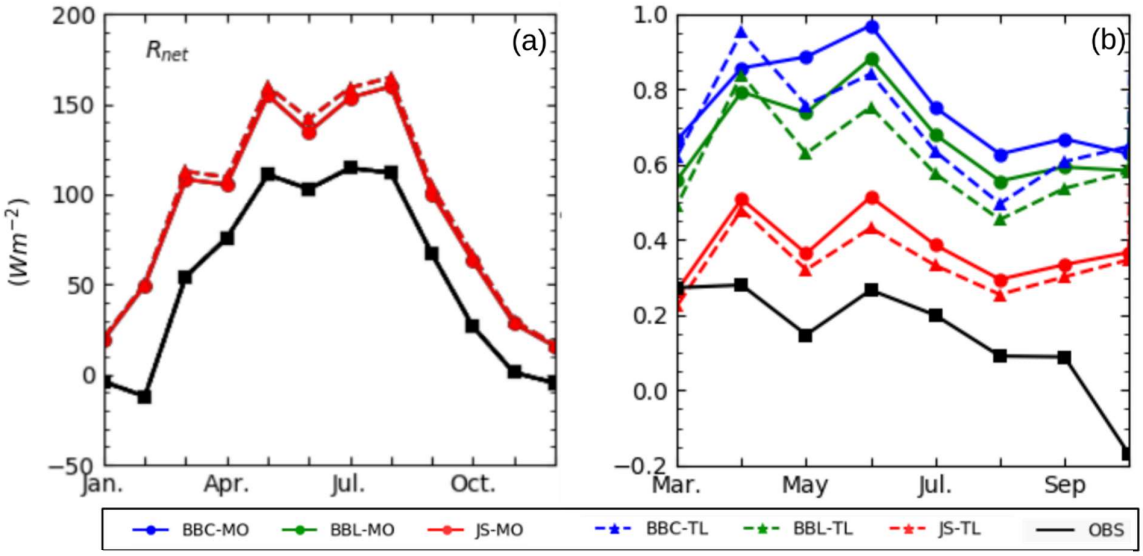

Figure 4.14. The monthly average of (a) net radiation and (b) Bowen Ratio at RO site in 2012. The calculation resutls with six simulation modes and observation data are shown. For Bowen Ratio only values range from -0.2 to 1.0 are shown.

radiation by the canopy emission and transmission. The results in **Figure 4.14 (a)** show the tiny effects of LAI on net radiation. The simulated net radiation employing MODIS LAI (MO) is closest to the observations.

The Bowen ratio is the ratio of sensible heat flux to latent heat flux; values less than 1 indicate that there is sufficient soil moisture to evaporate. From January to February and from November to December, the Bowen Ratio is very large due to the small latent heat fluxes at the RO site; hence we only consider the Bowen Ratio only between March and October (**Figure 4.14 (b)**). The observations show that the RO site is in a wet condition, and the simulated Bowen Ratio by the JS-type equations and TLAI are closest to observation. The BBC- and the BBL-type simulations result in Bowen Ratios close to 1 (semi-arid condition) from April to June, quite far of the observations.

The results of index of agreement (**Table 4.2**) show that both net radiation and ground temperature are very close to the observations (IoA = 0.80~0.87) for all vegetation schemes, and JS-TL performs best with 0.86 and 0.62 for latent heat and sensible heat flux, respectively. The IoA for the sensible heat flux ranges between 0.58 and 0.62, while for the latent heat flux IoA ranges from 0.28 to 0.86. TLAI improves the latent heat flux, but only slightly the sensible

heat flux. Thus different stomatal conductivity equations and LAI input impact more the latent than the sensible heat flux. The Taylor diagrams (**Figure 4.15**) show similar correlation coefficients between the different modes but different relative standard deviations. The JS-MO mode is closest to the observation for latent heat flux, for sensible heat flux the JS-TL mode is the closest.

Table 4.2. IoA of the calculation results with six simulation modes at RO site, 2012

	R_{net}	λE	H	T_g
BBC-MO-O	0.87	0.28	0.58	0.80
BBL-MO-O	0.87	0.46	0.60	0.80
JS-MO-O'	0.87	0.81	0.57	0.80
BBC-TL-O	0.86	0.72	0.61	0.83
BBL-TL-O	0.86	0.77	0.62	0.83
JS-TL-O'	0.86	0.86	0.62	0.83

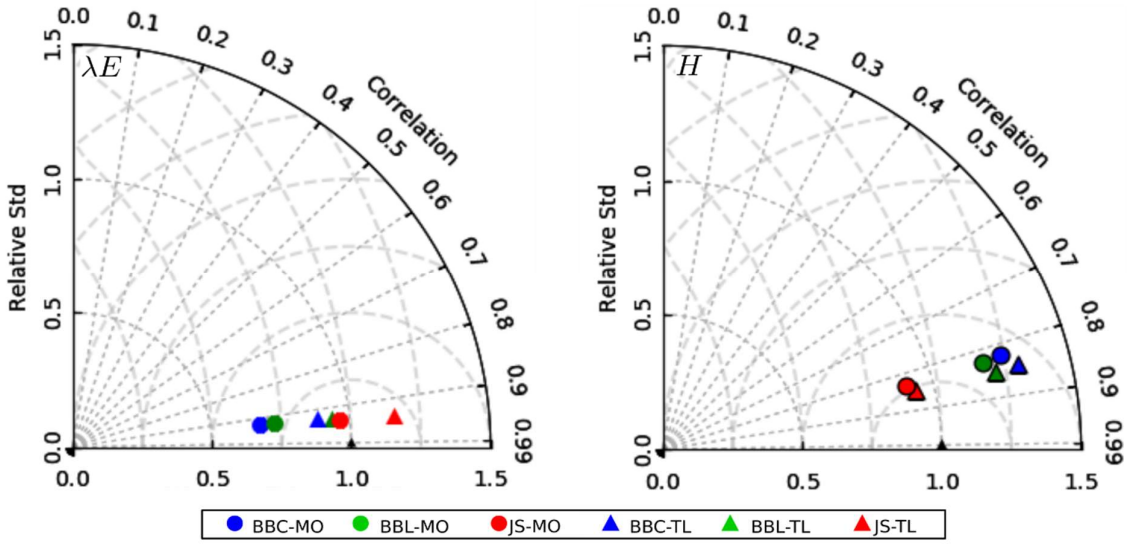

Figure 4.15. The Taylor Diagram shows the yearly statistical results of latent heat, and sensible heat fluxes with six simulation modes at RO site in 2012. The results are calculated from hourly data in one year.

4.3.2 Results for the crop sites Merzenhausen and Selhausen

The simulated latent heat fluxes at the crop sites Merzenhausen (MZ) and Selhausen (SE) sites are shown in **Figure 4.17** and **Figure 4.16**, respectively. Similar to the RO site latent heat is dominated by transpiration E_T, which is affected by canopy conductance g_c. Before harvest time, the simulated latent heat fluxes compare well with the observations. Winter wheat at Merzenhausen is mature in July, turns yellow, and transpiration is reduced. With harvesting in August the latent heat flux decreases rapidly. The potatoes were seeded in May and harvested in September at the Selhausen site. Potatoes wilt in August before harvesting and the observed latent heat flux starts to decrease. While at both crop sites the observed latent heat fluxes decrease rapidly during harvesting, the simulated latent heat fluxes do not because the LAI according to MODIS LAI and the simple LAI model TLAI do not show this decrease (see discussion in Section 4.2.2). Overall, the JS-TL simulation mode performs best latent heat flux both at MZ and SE sites.

Sensible heat fluxes are also affected by harvesting and seeding at both sites (**Figure 4.18 (a)** and **Figure 4.19 (a)**). The observation are missing between August to October at MZ site and between January to April at SE site (**Figure 4.18 (c)** and **Figure 4.19 (c)**). The soil surface in Selhausen is bare before seeding the potatoes in May and after harvesting in September. Without vegetative cover, the temperature gradient increases and hence sensible heat flux increases in July to August at the MZ site and in May and August to September at the SE site. The sensible heat flux starts to increase before harvesting because the crop leaves start to wilt. The LAI employed in the simulation does not response to harvesting nor seeding and hence the simulated sensible heat fluxes do not increase as rapidly as observed. Similar to the results at RO site, the simulated sensible heat flux is dominated by the sensible heat flux on vegetative cover H_V (**Figure 4.18 (c)** and **Figure 4.19 (c)**), and the sensible heat flux from the ground H_G is small (**Figure 4.18 (d)** and **Figure 4.19 (d)**). In the monthly average daily cycles results, the simulated sensible heat flux is also overestimated during night time (**Figure 4.18 (b)** and **Figure 4.19 (b)**), which cause the overestimated sensible heat flux in the monthly averaged results (**Figure 4.18 (a)** and **Figure 4.19 (a)**). From April to June, the observed sensible heat flux at the MZ site decreases and even below 0 W m^{-2} in May (**Figure 4.18 (a)**). The daily cycles in May are shown to investigate the reason (**Figure 4.18 (b)**). The observed sensible heat flux starts to

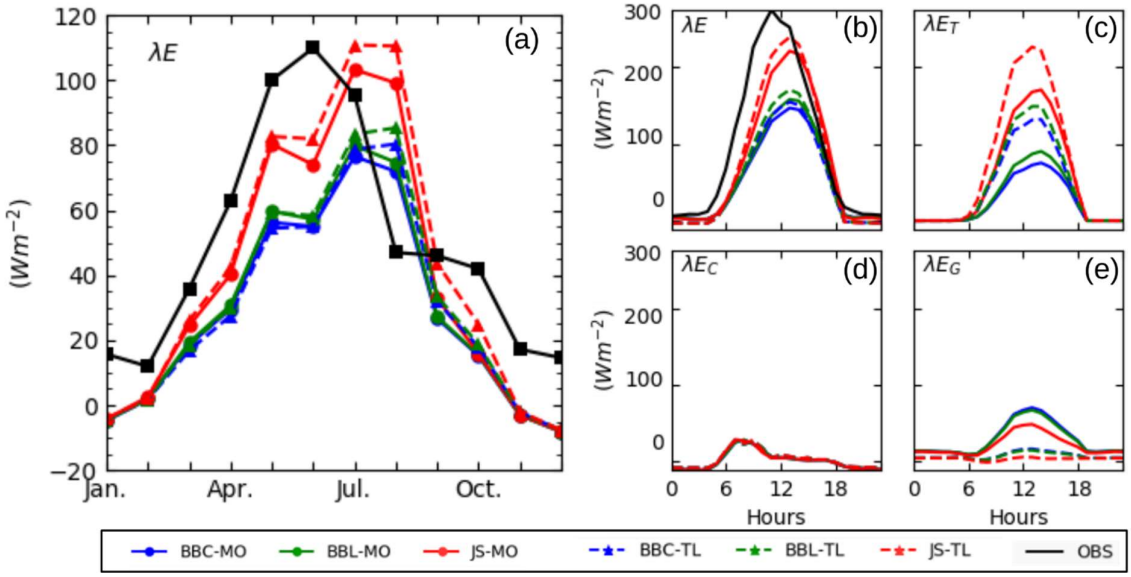

Figure 4.16 (a) The monthly average curves and (b) average daily cycles of latent heat flux from simulations and observation (OBS) at the Merzenhausen crop site for the year 2012. The average May daily cycles of (c) transpiration λE_T, (d) latent heat of intercepted water from the canopy λE_C, and (e) latent heat flux on the ground λE_G are shown on the right-hand side sub-plots.

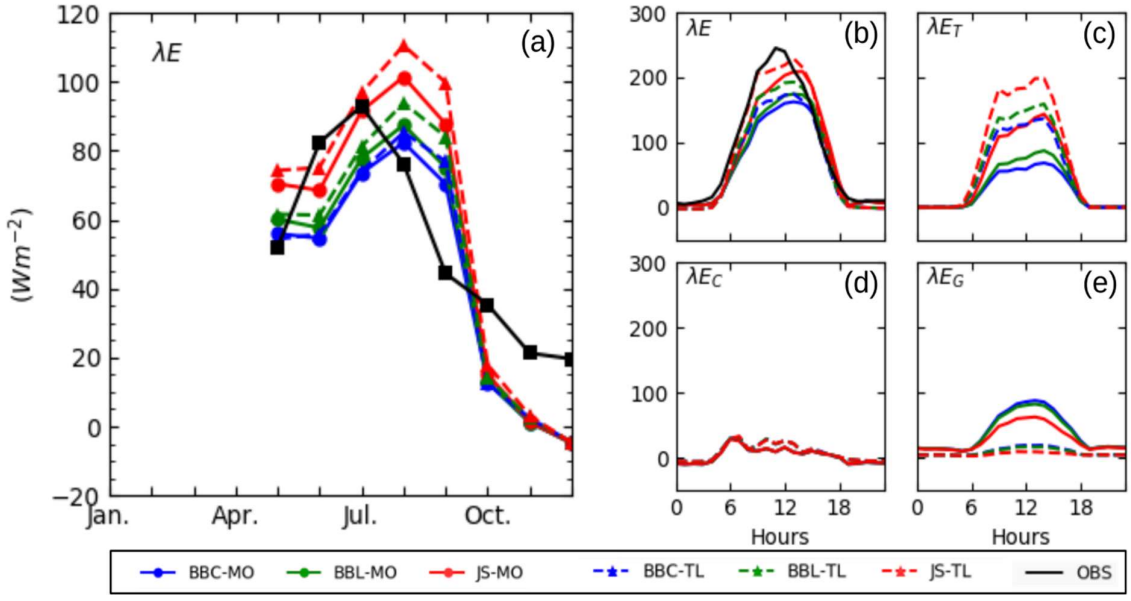

Figure 4.17. (a) The monthly average curves and (b) average daily cycles of latent heat flux from simulations and observation (OBS) at the Selhausen crop site for the year 2012. The average July daily cycles of (c) transpiration λE_T, (d) latent heat of intercepted water from the canopy λE_C, and (e) latent heat flux on the ground λE_G are shown on the right-hand side sub-plots.

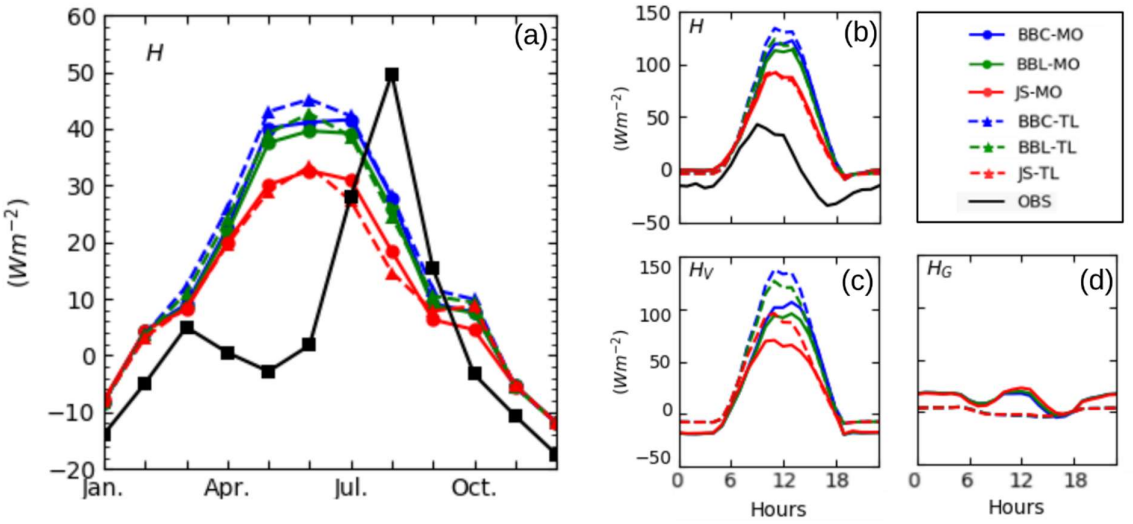

Figure 4.18. (a) The monthly average curves and (b) average daily cycles of sensible heat flux from simulations and observation (OBS) at the Merzenhausen crop site for the year 2012. The average May daily cycles of (c) sensible heat flux on vegetative cover H_V , and (d) sensible heat flux on the ground H_G are shown on the right-hand side sub-plots.

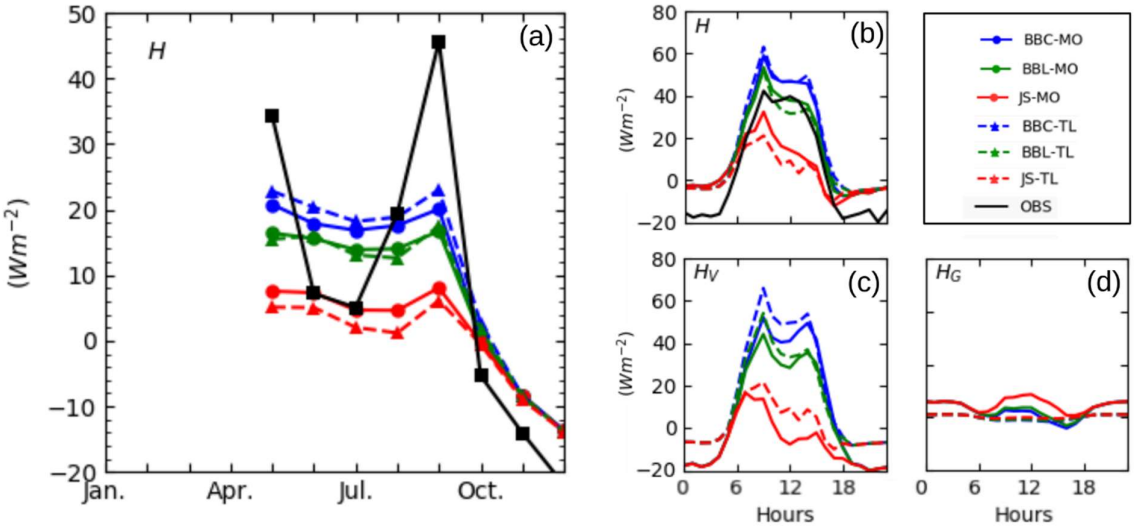

Figure 4.19. (a) The monthly average curves and (b) average daily cycles of sensible heat flux from simulations and observation (OBS) at the Selhausen crop site for the year 2012. The average July daily cycles of (c) sensible heat flux on vegetative cover H_V , and (d) sensible heat flux on the ground H_G are shown on the right-hand side sub-plots.

be negative from thirteen o'clock in May. However, the observed temperature gradient close to the ground is positive between twelve and fifteen o'clock , and is negative else (**Figure 4.20 (b)**). The low sensible heat flux might be caused by the oasis effect, which causes the flow of dry and warm air from the surrounding bared soil area to the vegetative area. The greening winter wheat is surrounding by other crops, which is still in the condition of bare soil. Therefore, the latent heat flux is much stronger than sensible heat flux in May, and the evaporative cooling on leaf surface may cause the less sensible heat flux.

The simulated ground temperature in monthly average is similar to the observations at both sites (**Figure 4.20 (a)** and **Figure 4.21 (a)**). The ground temperature is also mainly affected by the different LAI input types **Figure 4.20 (b)** and **Figure 4.21 (b)**), but the difference resulting from different stomatal conductance equations are not significant. When higher vegetative cover (i.e. higher LAI) is predicted by TLAI, the simulated ground temperature is lower during day time and higher at night. Vegetative cover keeps lower ground temperatures during the day and warmer temperatures during the night (Barradas & Fanjul, 1986).

The behaviour of simulated net radiation is similar to the observation, but the values are different from the observed values (**Figure 4.22 (a)** and **Figure 4.23 (a)**). The results vary insignificantly between the different simulation modes. The observed Bowen Ratio indicates that the crop sites are dry before seeding and after harvesting, and wet during the growth season (**Figure 4.22 (b)** and **Figure 4.23 (b)**), which is not captured by the simulations. During the growth season, the observed Bowen Ratio is captured at the SE site by the JS simulation mode but not at the MZ site.

At both crop sites, the IoA values (**Table 4.3**) indicate that net radiation and ground temperature are well reproduced by all simulations. Simulated latent heat and sensible heat fluxes are less well reproduced by the simulations mainly because of the missing land management (seeding and harvesting); hence their IoA values are also calculated without the affected months. At the MZ site, the latent heat flux differs more between the simulation modes than the sensible heat flux, with the JS-TL simulation mode performing the best. The BBC-TL simulation mode performs the best, but still not very good, for the sensible heat flux.

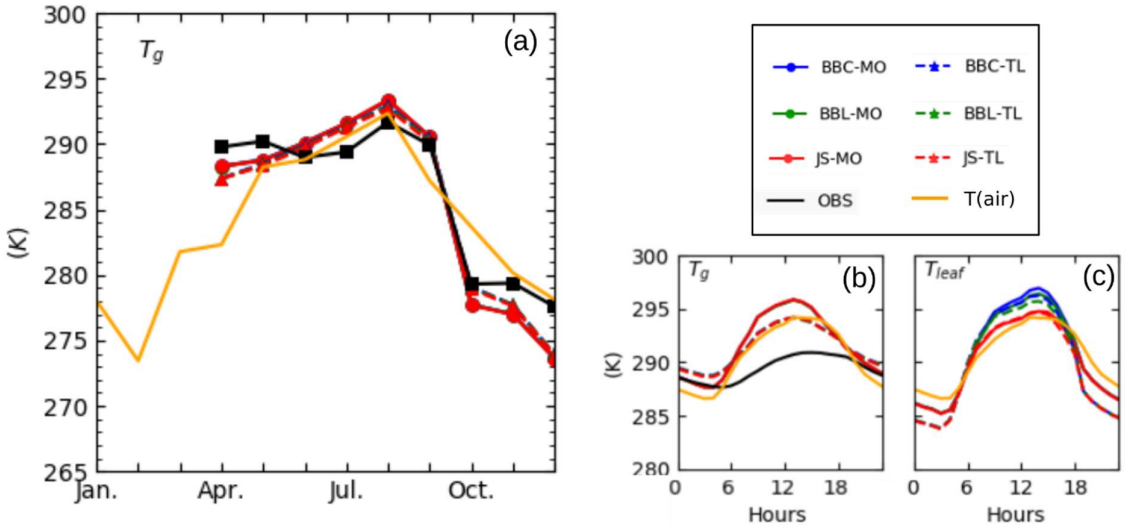

Figure 4.20. (a) The monthly average curves of ground temperature from simulations and observation (OBS) at the Selhausen crop site for the year 2012. The average July daily cycles of (b) ground temperature, and (c) leaf temperature are shown on the right-hand side sub-plots.

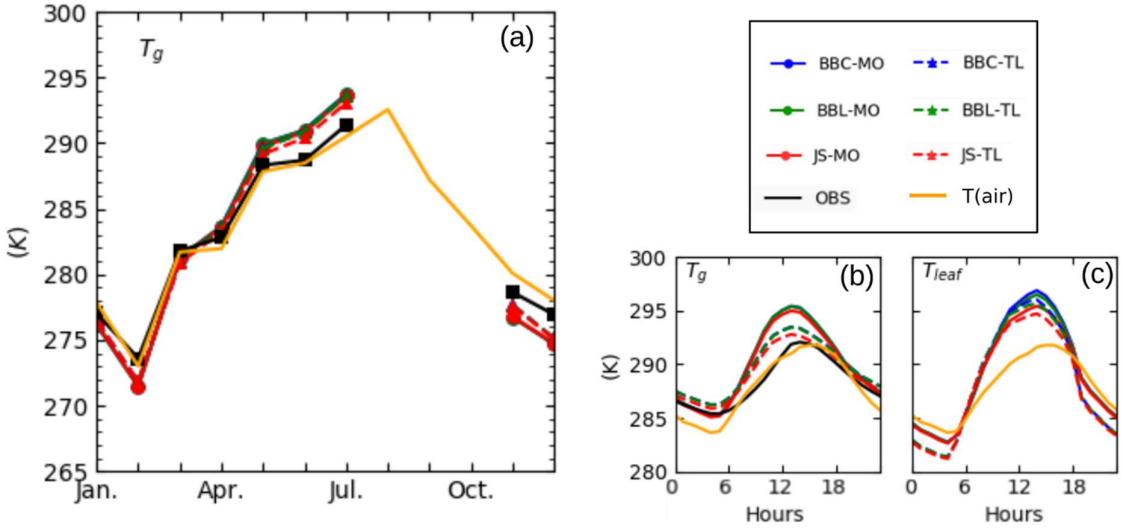

Figure 4.21. (a) The monthly average curves of ground temperature from simulations and observation (OBS) at the Merzenhausen crop site for the year 2012. The average May daily cycles of (b) ground temperature, and (c) leaf temperature are shown on the right-hand side sub-plots.

The BB-type performs better latent heat flux by employing updated physiological parameter set (**Table 4.1**), which is close to the results of the JS-type. However, the accuracy of sensible heat flux decreases (**Table 4.1**). The latent heat flux is better reproduced by the simulations at the SE site and differs not much between the simulation modes, without the management periods the JS-TL simulation mode performs best. For the sensible heat flux the BBC-TL simulation mode performs best with or without the months of management periods. According to the Taylor diagrams (**Figure 4.24**) the different simulation modes mainly differ by their standard deviation. At the MZ site BBC-TL and BBL-TL perform better for both latent heat and sensible heat fluxes, but the results by different simulation modes are close to each other. The results employing BBC-MO and BBL-MO simulation modes are improved by employing updated physiological parameter set, which is close to the best. But the results employing BBC-TL and BBL-TL simulation modes are not improved significantly (**Figure 4.24**). At the SE site BBL-TL and BBL-MO/TL perform better for latent heat and sensible heat fluxes, respectively.

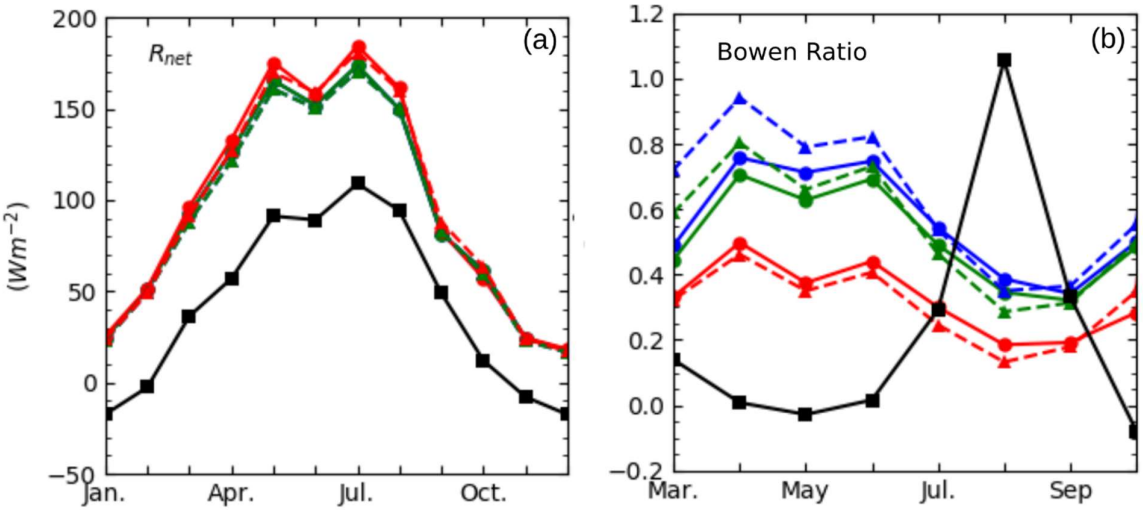

Figure 4.22. The monthly average of (a) net radiation and (b) Bowen Ratio at MZ site in 2012. Six simulation modes and observation data are shown. For Bowen Ratio only value range from 0 to 1.2 is shown.

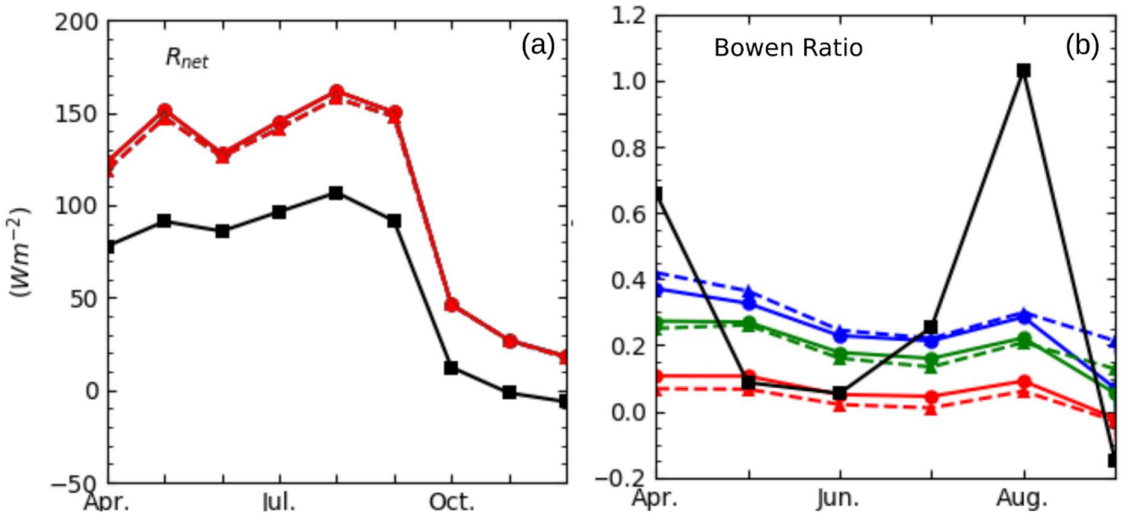

Figure 4.23. The monthly average of (a) net radiation and (b) Bowen Ratio at SE site in 2012. Six simulation modes and observation data are shown. For Bowen Ratio only value range from 0 to 1.2 is shown.

Table 4.3. Index of agreement of net radiation, latent heat, sensible heat and ground temperature by six simulation modes at MZ and SE sites in 2012. The yearly results are calculated with hourly data. The results without artificial interruption exclude [a] July and August, [b] between April to August, and [c] May, August and September.

		R_{net}	λE		H		T_g
MZ Site	*BBC-MO-O*	0.72	0.04	-0.23[a]	0.12	0.15[b]	0.91
	BBL-MO-O	0.72	0.14	-0.05[a]	0.07	0.13[b]	0.91
	JS-MO-O'	0.70	0.46	0.51[a]	-0.22	-0.01[b]	0.91
	BBC-TL-O	0.73	0.26	0.08[a]	0.19	0.31[b]	0.93
	BBL-TL-O	0.73	0.34	0.26[a]	0.12	0.27[b]	0.93
	JS-TL-O'	0.71	0.53	0.65[a]	-0.21	0.14[b]	0.94
SE Site	*BBC-MO-O*	0.87	0.68	0.58[c]	0.47	0.51[c]	0.88
	BBL-MO-O	0.87	0.70	0.67[c]	0.24	0.48[c]	0.88
	JS-MO-O'	0.87	0.72	0.79[c]	-1.48	-0.08[c]	0.88
	BBC-TL-O	0.88	0.73	0.70[c]	0.50	0.51[c]	0.89
	BBL-TL-O	0.88	0.73	0.78[c]	0.11	0.47[c]	0.89
	JS-TL-O'	0.88	0.71	0.83[c]	-2.81	-0.56[c]	0.89

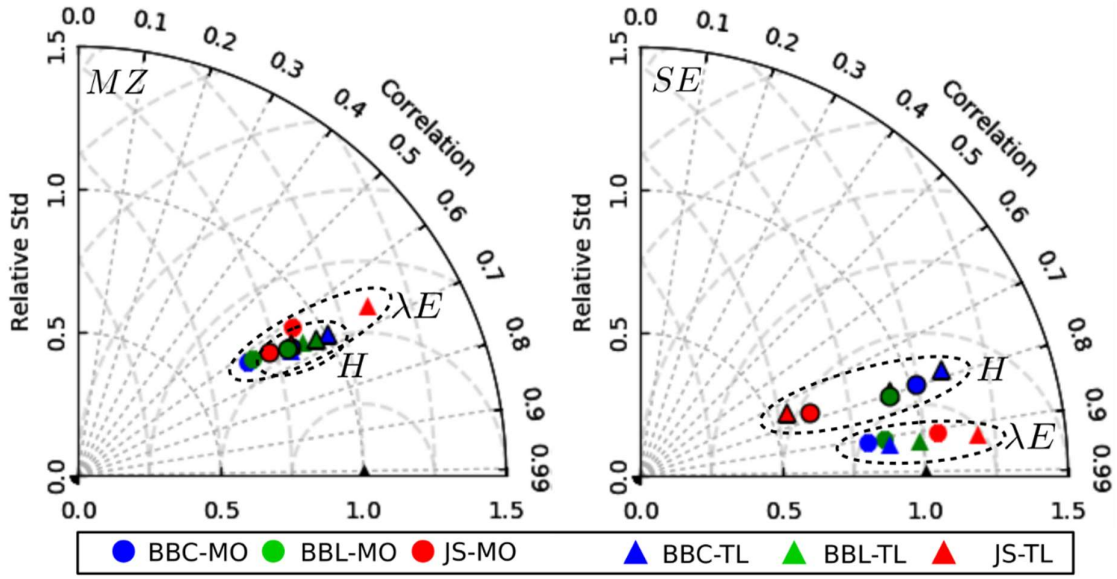

Figure 4.24. The Taylor Diagram shows the yearly statistical results of latent heat, and sensible heat fluxes with six simulation modes at MZ and SE sites in 2012. The results are calculated from hourly data in one year. The months of artificial interruption is excluded in these diagrams.

4.3.3 Results for the forested Wüstebach site

The simulated latent heat fluxes by the JS- and BBL-type are closer to the observation than the BBC-type **(Figure 4.25 (a))**. As for the other sites the latent heat flux is also dominated by transpiration λE_T (**Figure 4.25 (b)**) and thus by g_c. Due to the large LAI for forest (**Figure 4.9**) incoming solar radiation is strongly reduced leading to a very low λE_G The better simulation mode can not be distinguished from the monthly plots (**Figure 4.25 (a)** and **Figure 4.25 (b)**).

By both annual cycle and the July average daily cycle (**Figure 4.26 (a)** and **(b)**), the predicted sensible heat flux by the JS-TL mode performs best. The sensible heat flux is also dominated by the sensible heat flux from the vegetative cover H_V (**Figure 4.26 (c)**). Because the large LAI (**Figure 4.5** and **Figure 4.9**), less incoming solar radiation reaches the ground leading to lower ground temperatures at the WU site compared to the other sites (**Figure 4.13 (b)** and **Figure 4.26 (b)**) and thus a smaller H_G (**Figure 4.26 (d)**) and a smaller ground temperature change between day and night.

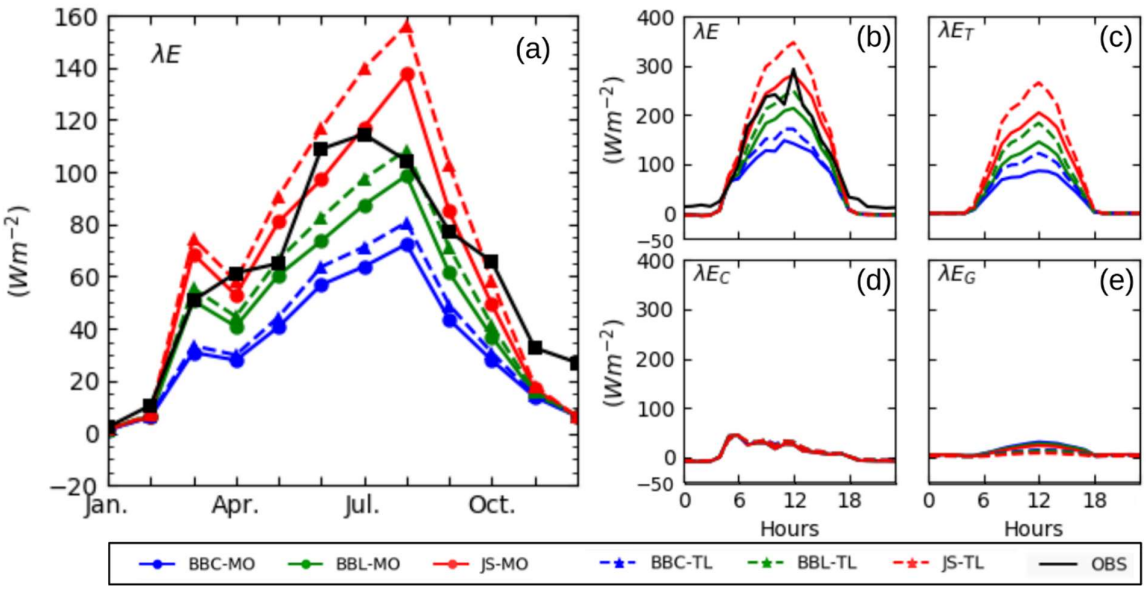

Figure 4.25. (a) The monthly average curves and (b) average daily cycles of latent heat flux from simulations and observation (OBS) at the forested Wüstebach site for the year 2012. The average July daily cycles of (c) transpiration λE_T, (d) latent heat of intercepted water from the canopy λE_C, and (e) latent heat flux on the ground λE_G are shown on the right-hand side sub-plots.

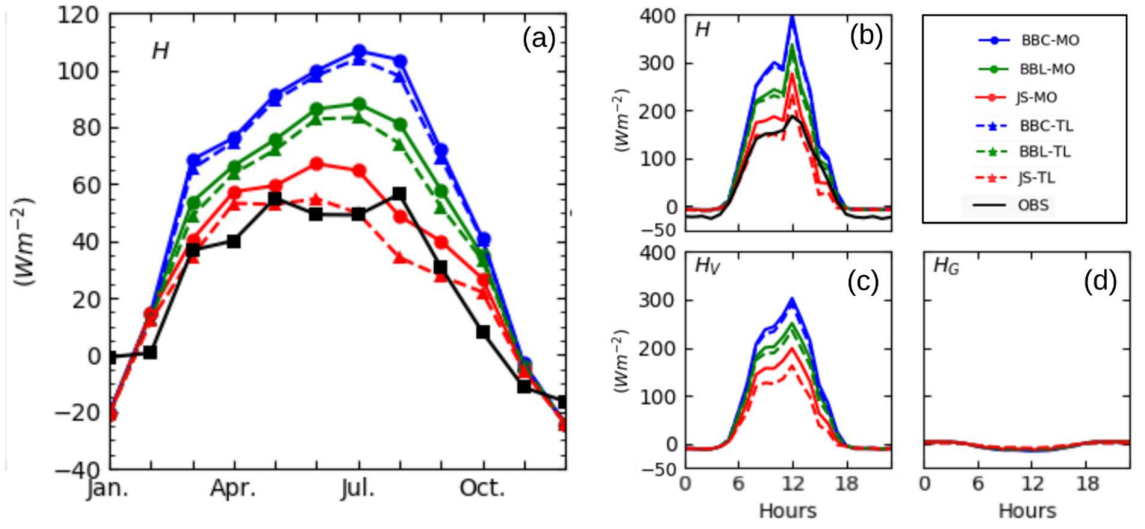

Figure 4.26. (a) The monthly average curves and (b) average daily cycles of sensible heat flux from simulations and observation (OBS) at the forested Wüstebach site for the year 2012. The average July daily cycles of (c) sensible heat flux on vegetative cover H_V , and (d) sensible heat flux from the ground H_G are shown on the right-hand side sub-plots.

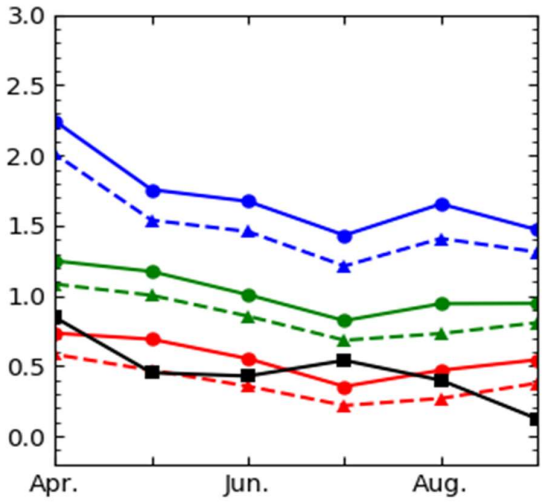

Figure 4.27. The monthly average of Bowen ratio at the WU site in 2012. Six simulation modes and observation data sets are shown. For the Bowen ratio only the value range from 0 to 3.0 is shown.

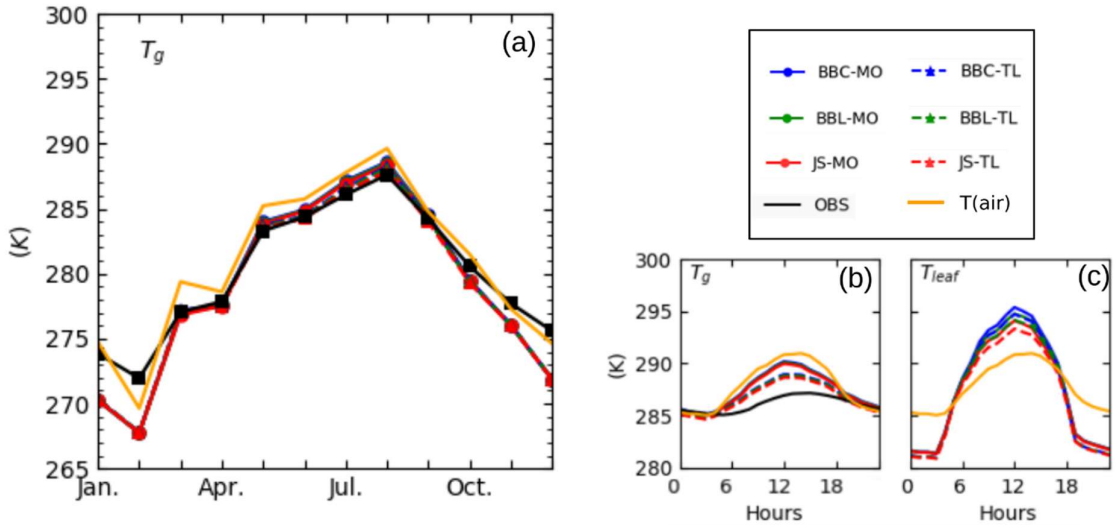

Figure 4.28. (a) The monthly average curves of ground temperature from simulations and observation (OBS) at the forested Wüstebach site for the year 2012. The average July daily cycles of (b) ground temperature, and (c) leaf temperature are shown on the right-hand side sub-plots.

All simulated ground temperatures are close to the observed ground temperature (**Figure 4.28 (a)** and **(b)**) and mainly affected by the LAI input type (**Figure 4.28 (b)**). Net radiation measurements are not available at the WU site. The observed Bowen Ratio indicates that the WU site is in a wet condition (**Figure 4.27**), which is best reproduced by the JS-type equations.

Ground temperatures at the WU site are well reproduced by all simulations according to the IoA (**Table 4.4**). The simulated sensible heat flux is as reliable as the simulated latent heat flux. The BBL-type equations better simulate the latent heat flux and the JS-type equation better simulate the sensible heat fluxes The different LAI input types do not strongly affect the simulation. According to the Taylor diagram (**Figure 4.29**) the simulations mainly differ in the standard deviations for latent and sensible heat flux. The BB-type equations better reproduce the latent heat fluxes while the sensible heat fluxes are better reproduced by the JS-type equation.

Table 4.4. IoA of the calculation results with six simulation modes at WU site, 2012. The net radiation is not shown due to the lack of observation.

	R_{net}	λE	H	T_g
BBC-MO-O	-	0.50	0.14	0.84
BBL-MO-O	-	0.57	0.41	0.84
JS-MO-O'	-	0.43	0.49	0.84
BBC-TL-O	-	0.56	0.21	0.84
BBL-TL-O	-	0.56	0.46	0.84
JS-TL-O'	-	0.18	0.46	0.84

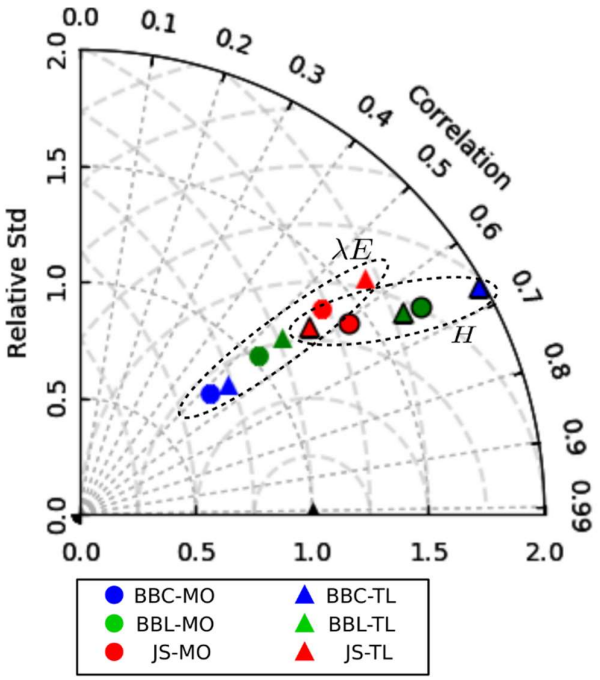

Figure 4.29. The Taylor diagram shows the yearly statistical results of latent heat, and sensible heat fluxes with six simulation modes at WU site in 2012. The results are calculated from hourly data in one year.

4.4 Results for soil moisture

The daily average results of simulated soil water content (θ_w) by the six simulation modes are shown in **Figure 4.30**, and are compared against the observation at the four sites including daily precipitation. During precipitation the observed soil moisture increases rapidly. This also happens in the simulations, but the variation is much smaller. The results of **Figure 4.30** shows that the uncertainty of vegetation scheme also propagates to the soil moisture. Soil water content is affected by g_s and LAI via Equation 2.13. In Equation 2.13, the S_w is affected by the change of θ_w (Equation 2.16). E_T is affected by g_c (as discussion in Section 4.3), and canopy storage S_{canopy} is affected by LAI via Equation 2.14 and 2.15. By these connections, the uncertainty of vegetation propagates to not only the surface heat fluxes but also the subsurface flow.

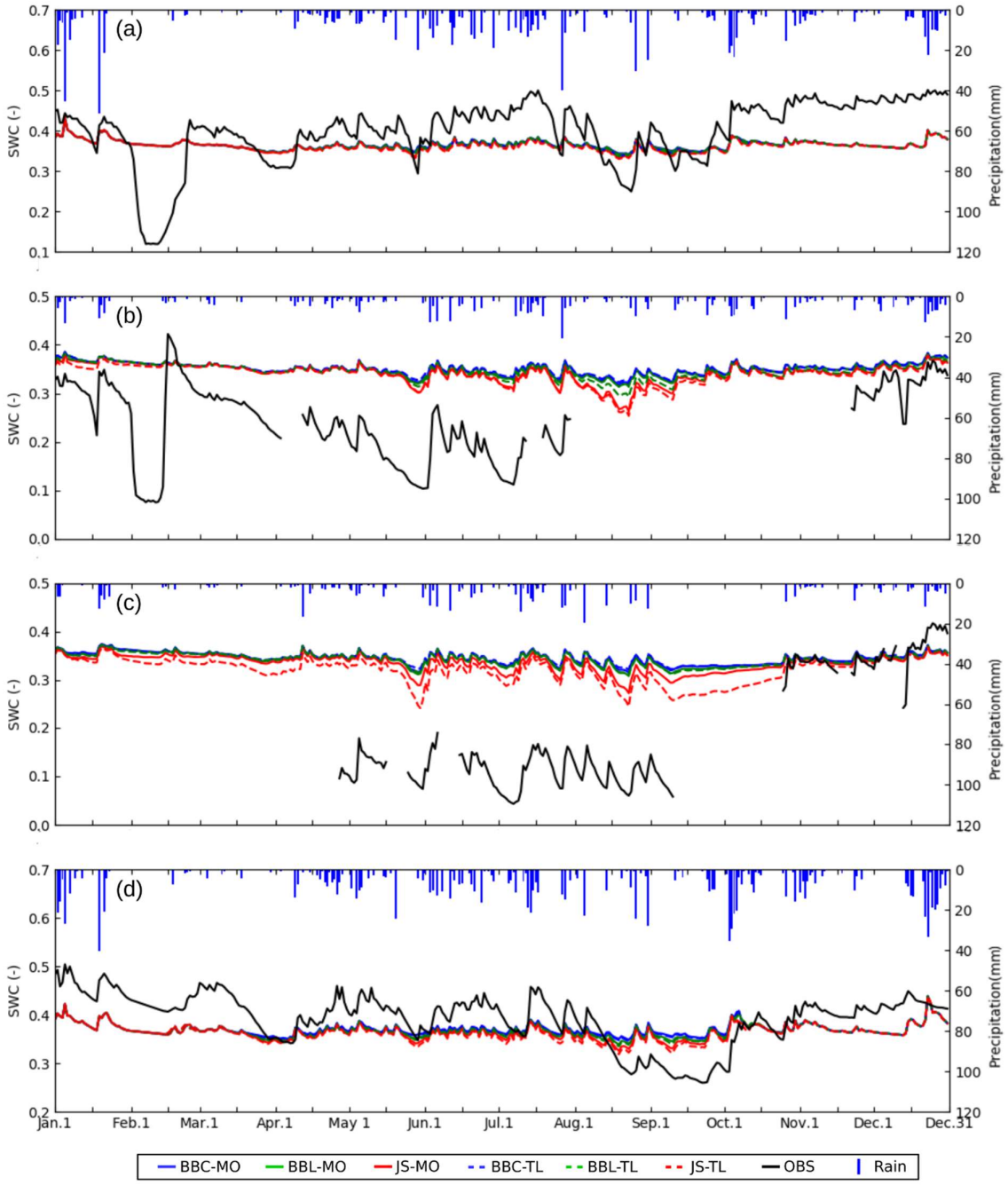

Figure 4.30. The daily average results of simulated soil water content (SWC) by six simulation modes are compared against the observation (OBS) at (a) RO site, (b) MZ site, (c) SE site, and (d) WU site at the top 2 to 5 cm depth soil. The daily accumulative precipitation is also shown.

4.5 Discussion

Firstly, in this chapter, we study how physiological parameter sets affect land-atmospheric interactions. The effects of both the original and updated physiological parameter sets are compared, which suggest the use of the updated ones (Sulis *et al.*, 2015). The employment of both parameter sets produce comparably good simulated ground temperature and net radiation. The updated parameter set leads to largely improved latent heat flux predictions at the expense of slightly deteriorated sensible heat flux predictions. This phenomenon is also found by Ronda *et al.* (2001) and Sulis *et al.* (2014) as the compensation error, which affects the accuracy of latent heat and sensible heat fluxes simultaneously. The differences between the results from the BBC- and the BBL-type equations are comparatively small. The parameters of net CO_2 assimilation rate and its form can be improved in the BB-type. Many studies observe and hypothesize that the net CO_2 assimilation rate decreases with the decrease in soil moisture, i.e. the drought effect on photosynthesis (Leuning, 1995; Niyogi & Raman, 1997; Cox *et al.*, 1998; Hoshika *et al.*, 2017). This demonstrate that the inclusion of soil moisture stress on photosynthesis does not always improve the prediction of latent heat flux. The drought effect on photosynthesis is important but may not be mature until this point. The drought effect on photosynthesis is minimized in our results because the observed soil water content is in a wet condition at all four sites. Based on the two reasons mentioned, we do not include soil moisture effect on our BB-type equation.

Secondly, we study how different simulation modes affect the heat fluxes, ground temperature, and soil moisture. Our results show that there are no significant differences between the simulated net radiation and ground temperatures in the six simulation modes. Ronda *et al.* (2004) also show that net radiation is not affected by using different stomatal conductance equations. The simulations of soil moisture do not differ much either, although clear bias is observed between the simulations and the observations. As expected, however, latent heat flux varies significantly between the simulation modes, with comparatively small repercussions for the simulation of the sensible heat flux. Many studies also found that energy heat fluxes are sensitive to the LAI and stomatal conductance in the LSM (Shao & Henderson-Sellers, 1996; Hou *et al.*, 2012; Jefferson *et al.*, 2015; Cuntz *et al.*, 2016).

Different site conditions reproduce different results and uncertainty. The results are the most clear-cut for the grass site in Rollesbroich, while more variable results are obtained for

the crop sites in Selhausen and Merzenhausen, where sowing and harvesting of winter wheat and potatoes are not sufficiently accurately reproduced by the two LAI simulation modes. At the forested Wüstebach site, the BBL and JS simulations modes result in quite similar values of the IoA of around 0.5 for both turbulent fluxes, which is almost independent of the LAI input. The simulation at the forest site is not performed as well as at the grass site due to the interruption of the canopy structure, which is also observed by Ran *et al.* (2017). The Monin-Obukhov similarity theory, employed in LSMs, is mainly validated by the flat and homogeneous site (Foken, 2006), and therefore the complex structure of a forest site causes more uncertainty than low-vegetation sites. At the four sites, the JS-type formulation performs somewhat better than the BBL-type formulation, but not under all weather conditions.

The Taylor diagrams, which visually identify the model performance, show that the uncertainty of vegetation schemes affects the standard deviation rather than the correlation. That is, the magnitude of heat fluxes is affected more than the behaviour. The BBL-type and JS-type show a better simulation performance of heat fluxes. The JS-type reproduces better results at the grass site, and the BBL-type produces better results at the crop site. At the forest site, the JS-type and the BBL-type perform better for latent heat flux and sensible heat flux, respectively. Generally, the simple dynamic LAI also performs better than MODIS LAI. The simple dynamic LAI reanalyses the statistical results from MODIS LAI by soil temperature, hence the reanalysed MODIS LAI may produce a more accurate LAI curve. The satellite data MODIS LAI is influenced by cloud blockage, albedo from snow (Tian *et al.*, 2004; Lawrence & Chase, 2007) and device limitation (Brut *et al.*, 2009). The simple dynamic LAI also has uncertainty, e.g. the loss of dynamic response to the climate (Arora, 2002). Nevertheless, each method, whether by MODIS LAI or simple dynamic LAI, has its own limitations in the resulting LAI curve. Thus, it is difficult to judge which method can reproduce reliable LAI.

The IoA, as a measure of the compliance of the simulations with the observations (IoA=1 for exact compliance and IoA=0 for no skill) varies for latent heat fluxes between the worst and best result from 0.39 to 0.86; for sensible heat fluxes, the IoA ranges between 0.05 to 0.32. In general, the JS-type coupled with the simple dynamic LAI (JS TL) performs best for latent heat flux, while none of the six modes consistently performs best for sensible heat flux due to the compensation error.

The JS-type equation can be viewed as two parts: the maximum stomatal conductance and the stress functions, which are both based on the fitting from observations and experiments. The maximum stomatal conductance determines the peak latent heat flux, and the behaviour of stomata is determined by stress functions. In our results, the calculated latent heat flux by the JS-type agrees with that found in the observation (IoA = 0.39 ~ 0.86), and means that the two parts of fitting by JS-type can perform latent heat flux for the environmental condition in the Rur catchment. At the same soybean cropland, Ran *et al.* (2017) calibrated and calculated with their PX-LSM, and performed good latent heat flux using the JS-type equation. Niu *et al.* (2011) developed the Naoh-MP LSM according to the validation against observation at a C4 grassland (Chen *et al*., 1997), and they also performed a good simulation of latent heat flux by the JS-type equation at the same grassland. The difference between the simulation conditions and the validation conditions affects the performance of latent heat flux by the JS-type. Ronda *et al.* (2004) employed the JS-type equation without the response to humidity and temperature, which revealed a poor performance for C4 grassland and soybean cropland. The reliability of stress function fitting affects the response of stomata to environmental factors. From the studies mentioned, different stress functions and parameters are employed in the JS-type equation and result in different performances of latent heat flux. Therefore, the JS-type equation can be regarded as a dynamic equation based on parameterization.

The BB-type equation can be regarded as a stomatal conductance equation based on the mechanism between stomata opening and photosynthesis, which is calculated by the net CO_2 assimilation rate. The net CO_2 assimilation rate mechanism, based on the C3 photosynthesis-path by Farquhar *et al.* (1980), is improved by integrating the sucrose synthesis (Collatz *et al.*, 1991) and then by adding the C4 photosynthesis-path (Collatz *et al.*, 1992). Dai *et al.* (2003) and Ran *et al.* (2017) employed this improved net CO_2 assimilation rate with the BBC-type equation, and performed latent heat flux for both C3 and C4 grassland well. Thus, the key to improving the BB-type equation is to improve the photosynthesis mechanism. However, the formulation of the net CO_2 assimilation rate is still being developed, to include the drought effect on photosynthesis. Some studies demonstrate that the net CO_2 assimilation rate decreases with a reduction in soil moisture (e.g. Ronda *et al.*, 2001; Kowalczyk *et al.*, 2006), but this effect is not clear in other studies (e.g. Bonan *et al.*, 2014; Ran *et al.*, 2017). Thus, the employment of drought effect on photosynthesis is considered differently from study to study. The use of vapor pressure deficit (Aphalo & Jarvis, 1993; Leuning, 1995) or relative humidity

(Collatz *et al.*, 1991; Mott & Parkhurst, 1991) in the BB-type equation is also still debated. Moreover, the physiological parameters in the BB-type can be changed for specific plants (e.g. Sulis *et al.*, 2015), Therefore, the BB-type equation can also be regarded as a dynamic equation based on the photosynthesis mechanism.

In our results, the JS-type reproduced better results than the BB-type with the original physiological parameter set, and the BB-type with an updated physiological parameter set reproduced even better simulation results than the JS-type. The BB-type can be better or worse than the JS-type depending on the chosen parameters for the BB-type, hence the comparison between the two dynamic equations, the JS- and the BB-type, is unreasonable. For decades, there has been a research question out there regarding which stomatal conductance equation is the best? Since vegetation schemes are not solved by the first principles, multiple solutions can exist. Based on the results of different stomatal conductance equations for different plant types at different sites in different years, we propose that the BB-type and the JS-type are two different ways to approach the real world (**Figure 4.31**), and both

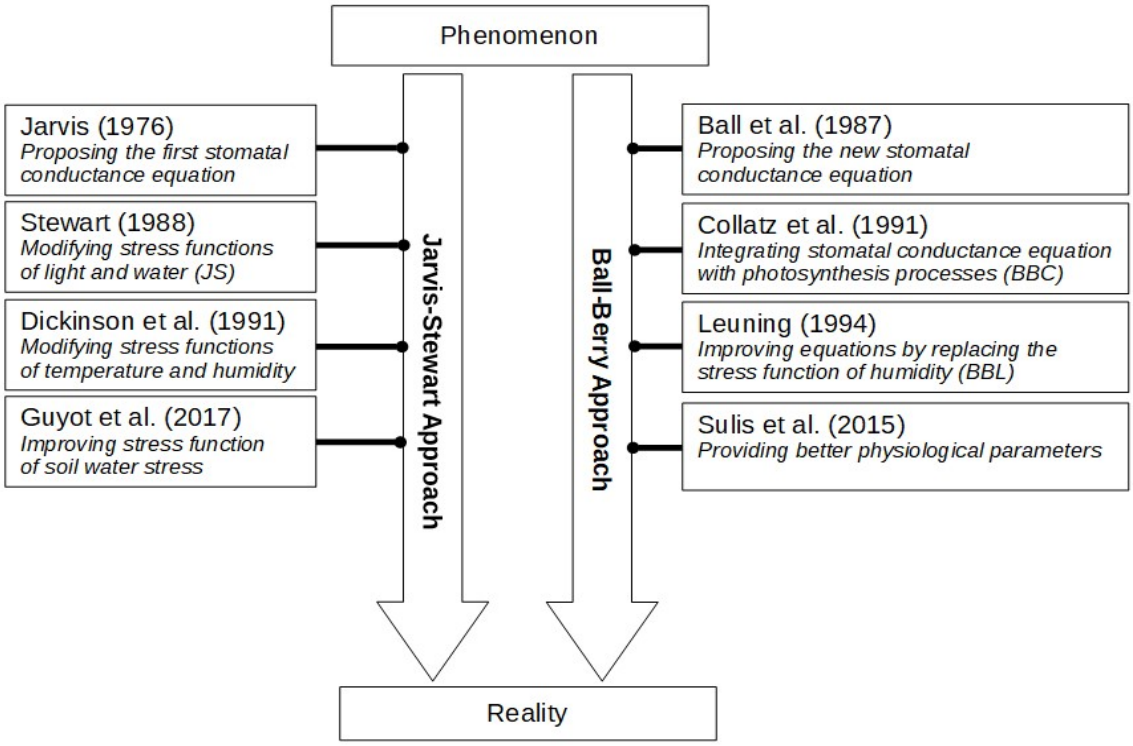

Figure 4.31. The concept of improvement of stomatal conductance equations

do it well. We classify the JS-type and the BB-type as the top-down and bottom-up approaches respectively. Using the concept of Feddes *et al.* (2001), a top-down approach, the JS-type, is a parameterization based on large scale observations or experimental data, which can be calibrated easily. Thus, the employment of the JS-type equation depends on the right choice of parameters and fittings. However, the top-down approach does not help to understand the physiological mechanism, i.e. vegetation responses to terrestrial systems. A bottom-up approach, the BB-type, is based on the understanding of physiological mechanisms, which requires a complete understanding of the mechanism. Hence, the employment of the BB-type equation depends on the accuracy of the photosynthesis mechanism. Instead of asking which equation is the best, we shall ask how to approach the real world using the BB-/JS-type to reduce the vegetation uncertainty in the land-atmosphere interaction.

Chapter 5

Impact of vegetation uncertainties on LSM and groundwater

The second part of the study analyzes the impact of the different simulation modes on the relation between the fluxes and the groundwater table depth (WTD) via its influence on the near-surface soil moisture. We expect different behaviour because the different canopy conductance equations depend differently on the simulated soil moisture. For this study the CLM3.5 is coupled to the Parflow (PF-CLM3.5), which now simulates the three-dimensional soil and groundwater flow instead of the 1D formulation used in CLM3.5. The 3D nature of Parflow requires meteorological forcing data for the whole Rur catchment, which we obtain from reanalysis data of German Weather Service used for weather prediction (Section 3.3). These data differ from the forcing data used in Chapter 4, which are meteorological variables measured directly at the four flux stations. The PF-CLM3.5 simulations are performed for both the years 2012 and 2013; but we discuss only results for January and July, which are considered to represent typical winter and summer time conditions.

We first analyze the impact of soil moisture on stomatal conductance by the soil water limitation factor in Section 5.1. Then the simulations using the six CLM3.5 simulation modes (different stomatal conductance equations and different LAI input types) are investigated in Section 5.2. Section 5.3 includes of propagation of vegetation uncertainty in the coupled model including its feedback on the ground water, and the feedback on latent heat flux, sensible heat flux, and net radiation.

5.1 The soil water limitation factor

Parflow within PF-CLM3.5 simulates 3D water flow in the saturated and unsaturated zone. The predicted soil water content (θ_w, soil moisture in the unsaturated zone) impacts the transfer of water from the soil to the vegetation via roots and to the atmosphere; this impact is formalized by the soil water limitation factor β_t (Equation 2.48). The water table depth (WTD) is defined as the upper surface of the saturated zone (**Figure 1.3**). WTD is zero at land surface, increases downwards and is negative above the surface. In the saturated zone, θ_w is equal to the saturated soil water content θ_{sat}. As discussed in Section 1.3, the ranges of the energy limited zone and the water limited zone depend on the soil water content. In the energy limited zone, WTD is small, and the soil water limitation factor approaches 1. In the transition zone the soil water limitation factor strongly decreases with increasing WTD until it does not vary anymore with increasing WTD in the water-limited zone.

Over the Rur catchment model area plant types and soil vary between the 500m x 500m grid columns as do the weather conditions, which results in variable relations between the soil water limitation factor β_t and the WTD as seen in **Figure 5.1** for July 2013. Before conducting the PF-CLM3.5 results, the PF-CLM3.5 simulation employs the spin-up process to reach its equilibrium state (Shrestha *et al.*, 2014; Rahman *et al.*, 2014). Each simulation modes applies different spin-up period to reach equilibrium state (e.g. the BBC-MO takes 3 year cycles, and JS-TL takes 11 year cycles), and therefore the state of soil moisture is different from each modes. Shao & Henderson-Sellers (1996) indicates that different land surface model has different required cycles to reach equilibrium state, and thus the different equilibrium state of soil water content is reached by different vegetation schemes in our result. In the energy limited zone (WTD < 1.7m), the soil water limitation factor (about 1) is not affected by weather condition and geographical condition significantly. In the transition zone and in the water limited zone, the soil water limitation factor depends on the particular simulation mode and on the local soil, vegetation, and weather conditions. The JS-type combined with the simple LAI model (TLAI) predicts the largest range for the soil water limitation factor, which is caused by its large canopy conductance (compared to the other equations, see section 4.3) which in turn results in larger transpiration E_T and thus higher root water uptake (Equation 2.46) and lower soil moisture (see also Section 4.4). As discussed in Section 4.3, the canopy conductance for forests is smaller than for the grass and crop sites; hence the soil water limitation factor is

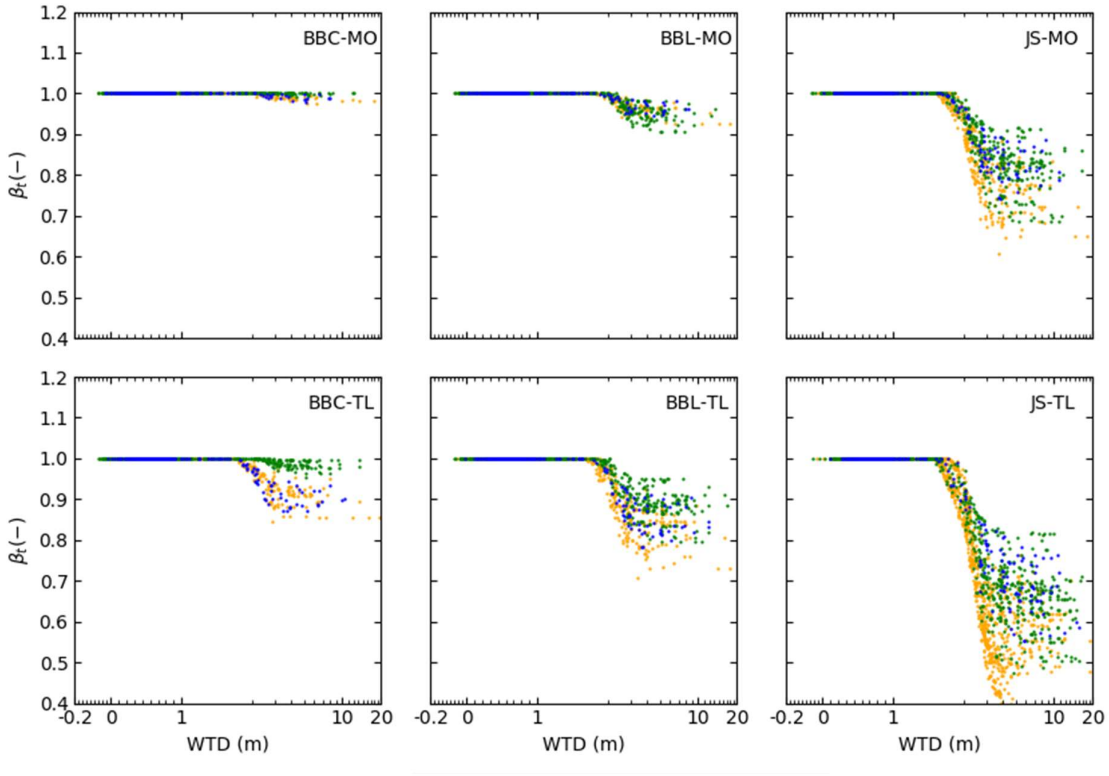

Figure 5.1. The scatter plots of the monthly average soil water limitation factor against water table depth (WTD) by six simulation modes in July, 2013. Each dot represents a grid on the model surface, and the yellow, blue, and green dots represent the crop, grass, and (needle-leaf evergreen) forest types, respectively.

larger (not experience dry condition) at forest sites in the simulation results of PF-CLM3.5.

The catchment-averaged July precipitation was 167.3mm in 2012 and only 33.7mm in 2013, with average incoming solar radiation of 197 W m^{-2} and 243 W m^{-2}, respectively. Thus July 2012 was considerably wetter and cooler than July 2013. Compared to dry July 2013, the soil water limitation factor does not decrease significantly from 1 with WTD in the wet July 2012 anywhere in the catchment (not shown). Thus, the soil water content in the unsaturated zone never reaches its critical point. The same holds for the winter in both 2012 and 2013 (not shown).

5.2 Variation of stomatal conductance and LAI with WTD

The monthly averaged stomatal conductance at each grid point for July 2013 for the different simulation modes are consistent with the results from CLM3.5 (discussed in Chapter 4) and shown in **Figure 5.2**. Values simulated by the JS-type are larger than those of the BB-type in the energy limited zone with the forest (needle-leaf evergreen tree) leading to the smallest values. The JS-type connects with the groundwater via Equation 2.32 with the stress function of soil water $f(\theta_w)$ replaced by the soil water limitation factor β_t (discussed in Section 3.4.1). In the BB-type the soil water limitation factor affects the stomatal conductance via its impact on the net CO_2 assimilation rate (A_{net}). As shown in **Figure 5.2**, the stomatal conductance from the JS-type changes with WTD, as opposed to the BB-type. Obviously the BB-type require drier soil condition in order to achieve a water-limited status, which is not reached in our simulation but was reached in the simulations employing the BBC-type over more semi-arid climates by

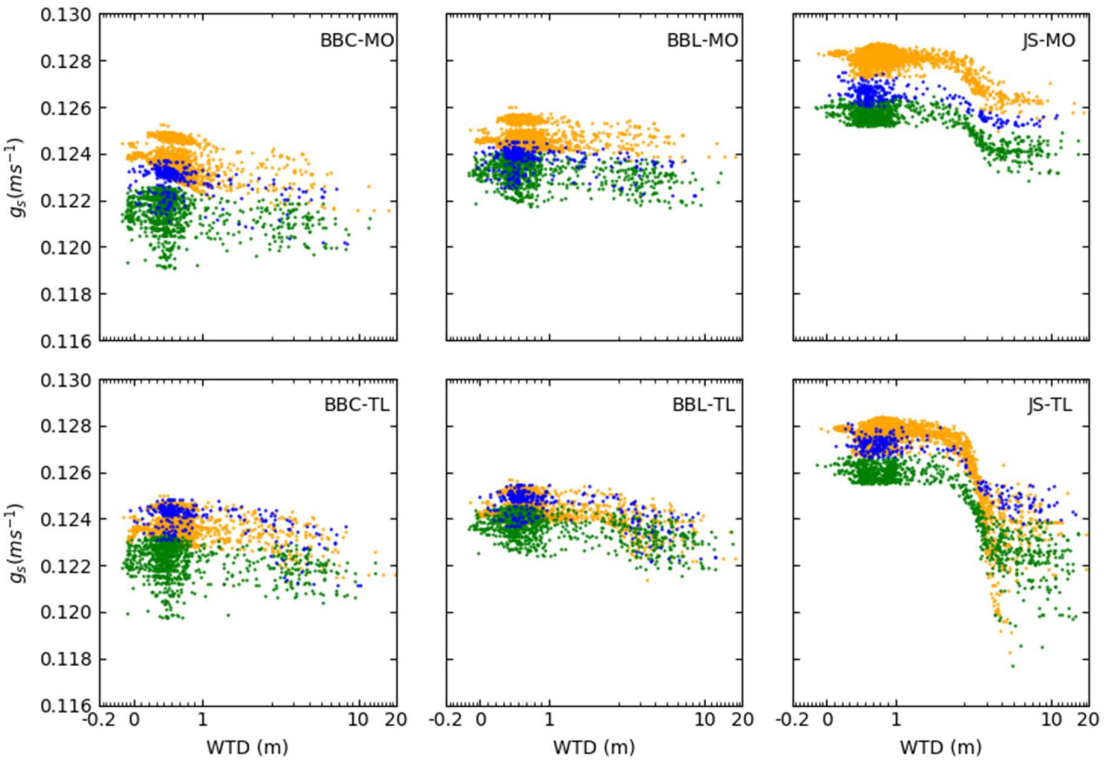

Figure 5.2. The scatter plots of the monthly average stomatal conductance g_s against water table depth (WTD) by six simulation modes in July, 2013. Each dot represents a grid on the model surface, and the yellow, blue, and green dots represent the crop, grass, and (needle-leaf evergreen) forest types, respectively.

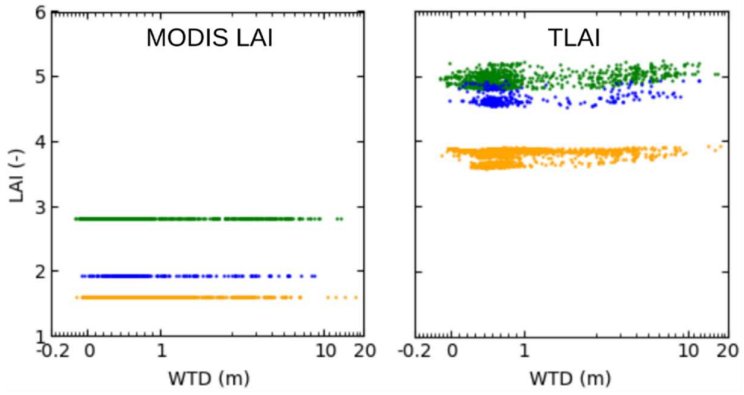

Figure 5.3. The scatter plots of MODIS LAI and TLAI against water table depth (WTD) in July, 2013. Both LAI results are calculated with the BBL-type stomatal conductance equation, and the simulation results by the other two stomatal conductance equations are similar. Each dot represents a grid on the model surface, and the yellow, blue, and green dots represent the crop, grass, and (needle-leaf evergreen) forest types, respectively.

Kollet & Maxwell (2008) and Rihani *et al.* (2010).

As discussed in Section 3.6, the MODIS-derived LAI is a monthly average and thus kept constant for each vegetation types for one month (**Figure 5.3**) in contrast to the simple dynamic LAI (TLAI), which depends on the ground temperature following Equation 2.42. Only the results from the BBL-type are shown since the results for the BBC- and the JS-types are similar. TLAI is also independent of the WTD, and the variation range of TLAI at the same WTD is affected by ground temperature, which is affected by different weather condition.

5.3 Variation of heat fluxes and net radiation with WTD

Figure 5.4 illustrates for July 2013 the relations between monthly averaged latent heat fluxes and water table depth. To investigate how vegetation scheme affects the latent heat flux, the components of latent heat flux are discussed firstly. The latent heat flux is the sum of the latent heat fluxes from the ground λE_G, the transpiration from the leaves λE_T and the evaporation of intercepted water from the leaves λE_C (Eq. 2.10). λE_G decreases with the increasing WTD due to a decreasing capillary rise from the ground water until a critical depth below which λE_G approaches a minimum (**Figure 5.5**) when groundwater can not provide water to the unsaturated soil (Kollet & Maxwell, 2008; Maxwell & Condon, 2016). Then λE_G depends on the soil water content, which is determined by the weather forcing and not by WTD. As

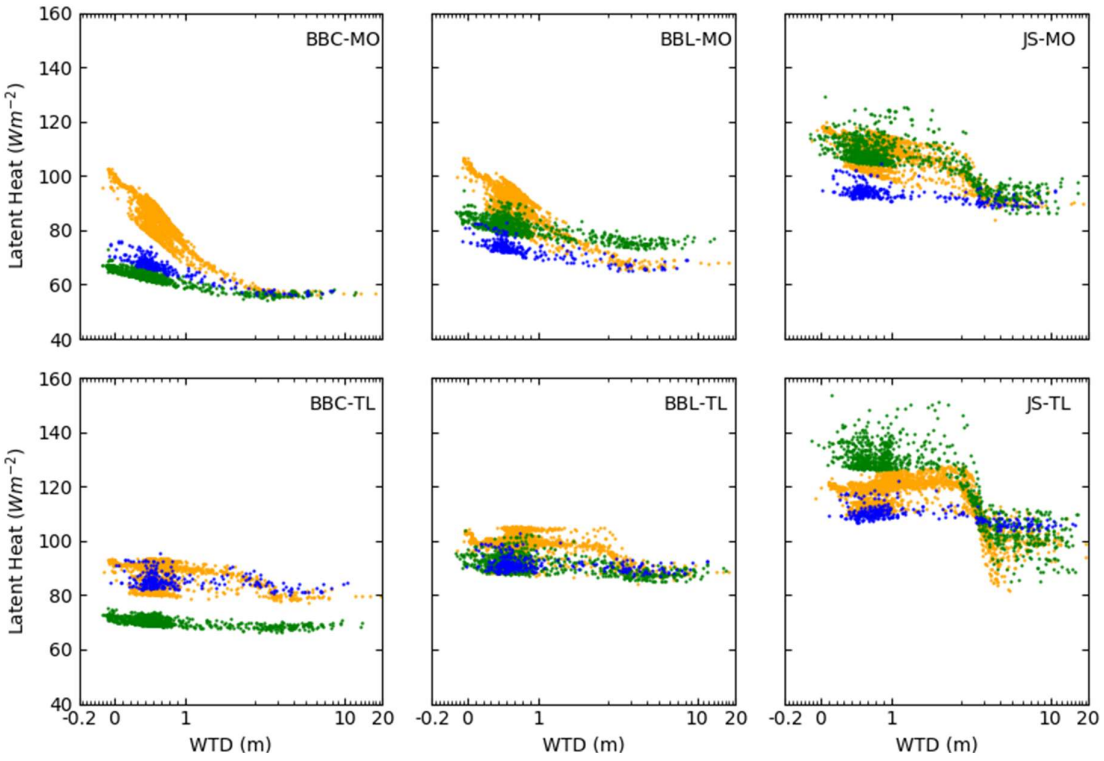

Figure 5.4. The scatter plots of the monthly average latent heat λE against water table depth (WTD) by six simulation modes in July, 2013. Each dot represents a grid on the model surface, and the yellow, blue, and green dots represent the crop, grass, and (needle-leaf evergreen) forest types, respectively.

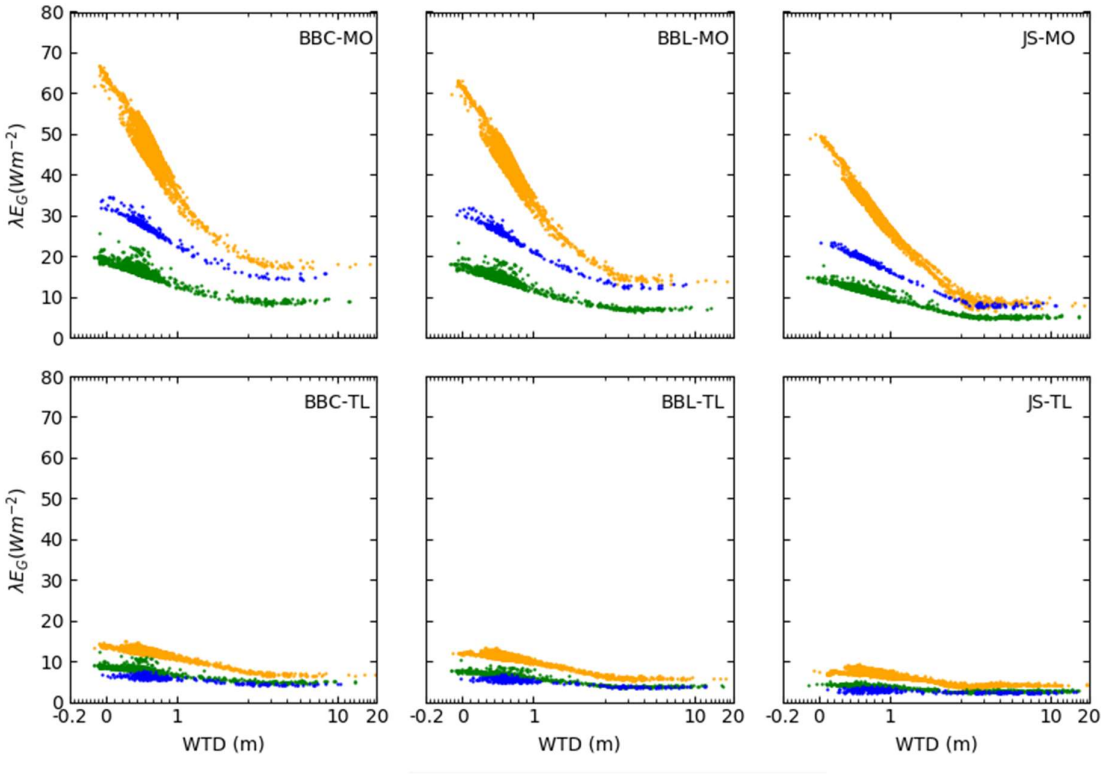

Figure 5.5. The scatter plots of the monthly average latent heat flux on the ground λE_G against water table depth (WTD) by six simulation modes in July, 2013. Each dot represents a grid on the model surface, and the yellow, blue, and green dots represent the crop, grass, and (needle-leaf evergreen) forest types, respectively.

discussed in Section 4.3, λE_G is affected by canopy conductance as also observed in **Figure 5.5** that higher g_c results lower λE_G, i.e. λE_G(JS) < λE_G(BBL) < λE_G(BBC). According to **Figure 5.2** and **Figure 5.3**, the difference between the stomatal conductance equations is small while the two LAI input types differ largely. Hence, λE_G predicted by the different stomatal conductance equations differs only slightly while the different LAI inputs lead to larger discrepancies: larger LAIs lead to smaller λE_G as discussed in Section 4.3. Hence λE_G under forests (**Figure 5.5**) is smaller than at other sites. In the simulation using the simple dynamic LAI (TLAI) the difference between the plant functional sites are small because λE_G approaches a minimum when the LAI reaches a critical point, which is reported by Granier *et al* (2000). When leaf area covers the land surface, the absorbed energy on the ground is limited and hence less water evaporated from the ground surface.

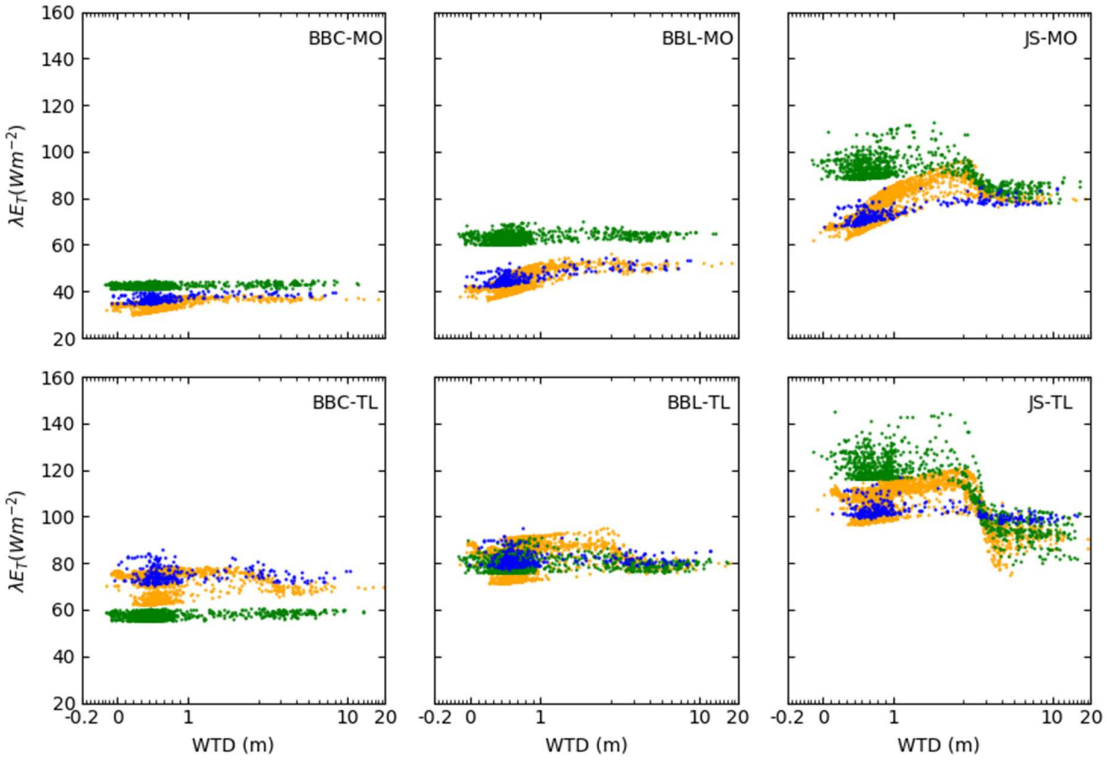

Figure 5.6. The scatter plots of monthly average transpiration λE_T against water table depth (WTD) by six simulation modes in July, 2013. Each dot represents a grid on the model surface, and the yellow, blue, and green dots represent the crop, grass, and (needle-leaf evergreen) forest types, respectively.

Plant transpiration λE_T is controlled by canopy conductance g_c (Section 4.3). **Figure 5.2** shows that the transition zone for g_s is only clearly reached by the JS-type (**Figure 5.6**). The distribution of λE_G with WTD depends more on soil moisture than on the soil water limitation factor. However, λE_T depends on the soil water limitation factor; WTDs below the critical depth do not impact its variation as opposed to λE_G and λE_T (Maxwell and Condon 2016). As discussed in Section 4.3, the impact of λE_C on λE is small and depends on the LAI, as also seen in **Figure 5.7**, which either depend on WTD (**Figure 5.3**).

Based on the previous discussion, λE_C is very small, and hence λE mainly consists of λE_T and λE_G. In the results with the simple dynamic LAI (TLAI), λE is dominated by λE_T; hence only λE_T(JS-TL) changes with WTD significantly following the behaviour of β_t against WTD. In the results with the MODIS LAI, λE_T and λE_G dominate the behaviour of λE. λE_T(BBC-MO)

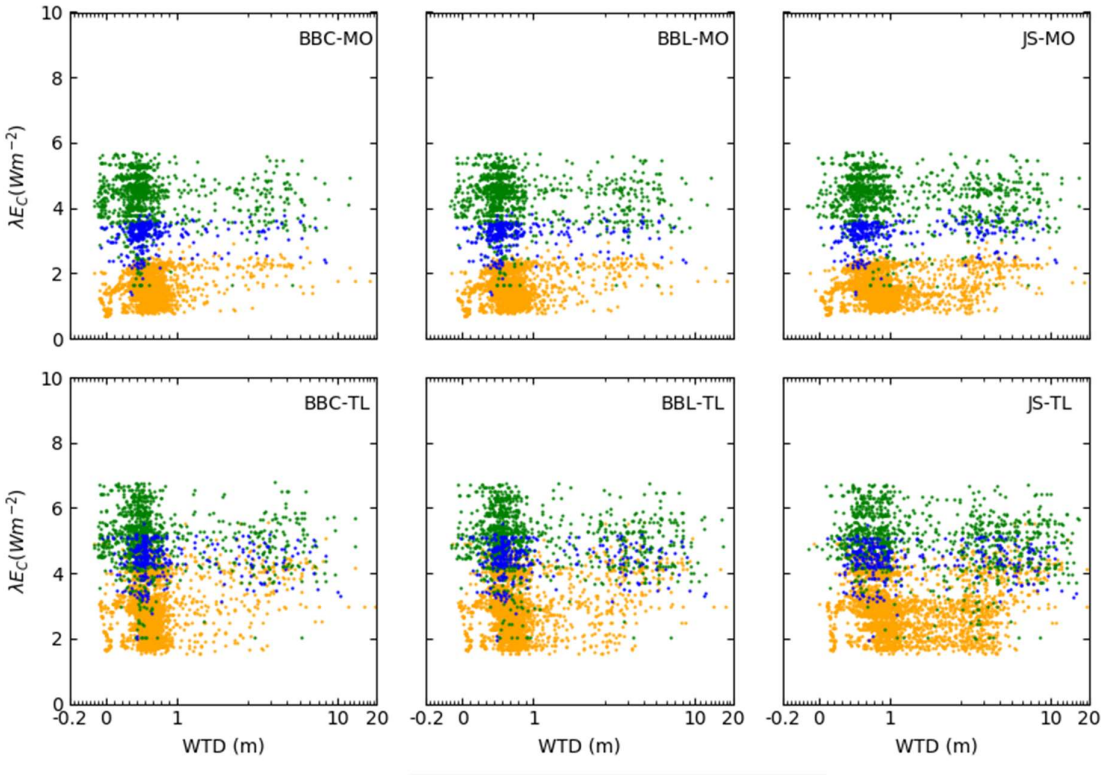

Figure 5.7. The scatter plots of monthly average latent heat on the vegetative canopy λE_C against water table depth (WTD) by six simulation modes in July, 2013. Each dot represents a grid on the model surface, and the yellow, blue, and green dots represent the crop, grass, and (needle-leaf evergreen) forest types, respectively.

and λE_T(BBL-MO) do not change significantly with WTD, but λE_G(BBC-MO) and λE_G(BBL-MO) do. Hence the behaviour of λE(BBC-MO) and λE(BBL-MO) against WTD follows the behaviour of λE_G. λE(JS-MO) follows the behaviour of λE_T(JS-MO) and λE_G(JS-MO) with λE_T(JS-MO) dominating. Both λE(JS-MO) and λE(JS-TL) are impacted most by λE_T hence both follow the behaviour of β_t. The effect of WTD on latent heat flux over the grass is unclear, which is also reported by Maxwell and Kollet (2008) and Rihani *et al.* (2010). Rihani *et al.* (2010) proposed a reason that λE_G is greater than $\lambda E_T + \lambda E_C$ causing by the way how grass and plant resistance being parameterized. We do not observe the greater λE_G in the simulation, but we also observe the phenomenon that λE by grass is insensitive to WTD.

To understand the different relations between sensible heat fluxes with WTD for the six

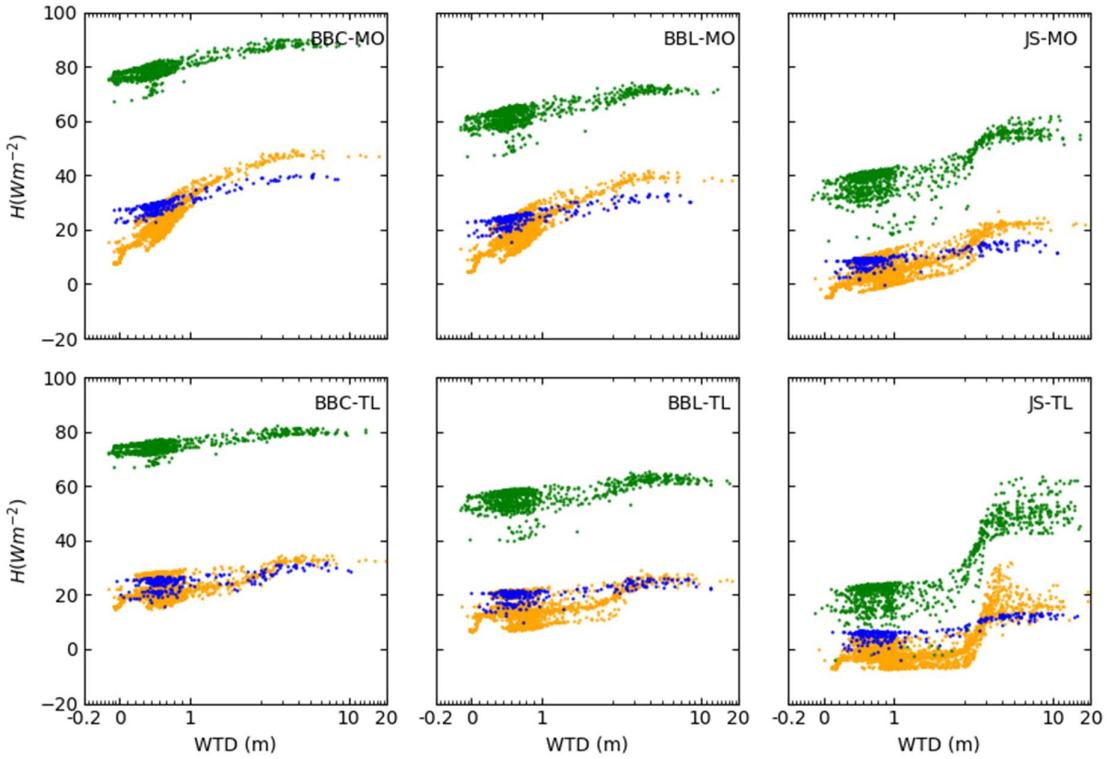

Figure 5.8. The scatter plots of monthly average sensible heat flux H against water table depth (WTD) by six simulation modes in July, 2013. Each dot represents a grid on the model surface, and the yellow, blue, and green dots represent the crop, grass, and (needle-leaf evergreen) forest types, respectively.

simulation modes shown in **Figure 5.8,** we analyze the behaviour of its components (see Equation 2.10): sensible heat from the vegetation canopy H_V and from the ground H_G (**Figure 5.9** and **Figure 5.10**, respectively. H_V is affected more by the stomatal conductance than by the LAI (**Figure 5.9**) because the stomatal conductance affects the aerodynamic resistance to heat flux on vegetation via aerodynamic resistance formulation. As for the latent heat flux only for the JS-type, H_V shows clearly the typical step function behaviour with WTD: no change with WTD in the energy limited zone followed by an increase when the soil moisture exceeds a critical level until it reaches a plateau. In the water-limited zone, the moisture supply from the groundwater stops and hence the WTD dynamics no longer affects surface heat fluxes. Similar to the results by CLM3.5 (Section 4.3) H_G depends more on the LAI input type than on the different stomatal conductance equations (**Figure 5.10**). Accordingly, H_G is lowest at

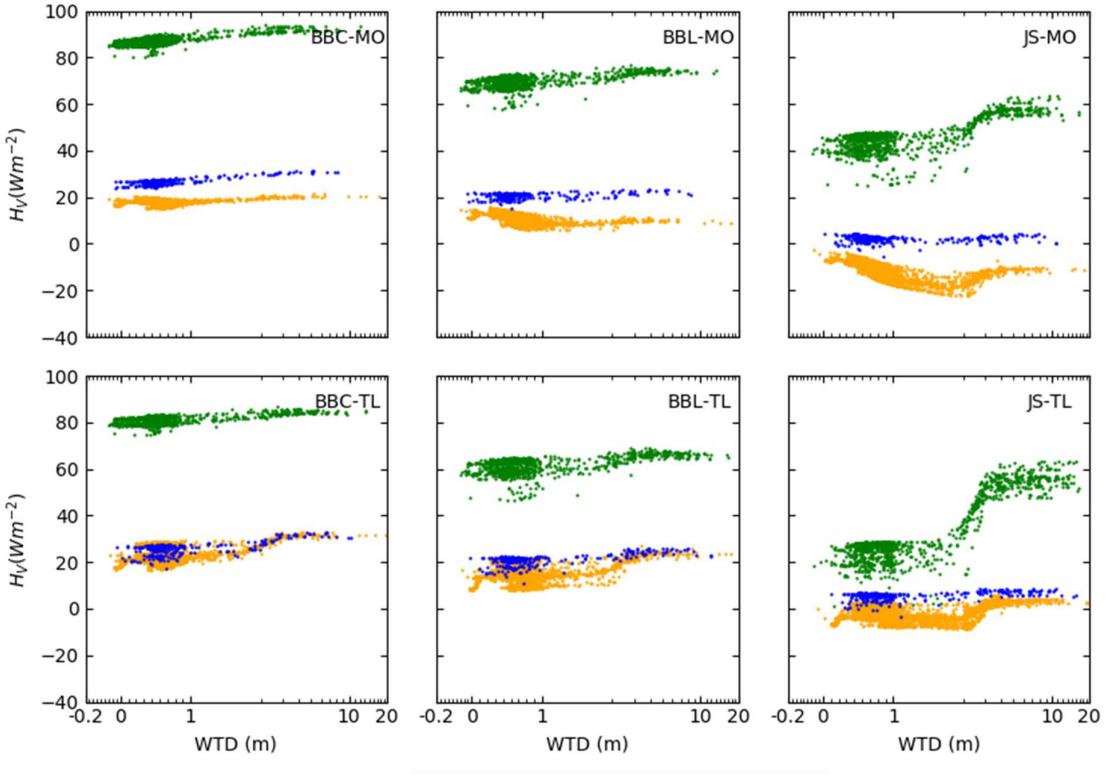

Figure 5.9. The scatter plots of monthly average sensible heat flux from vegetative cover H_V against water table depth (WTD) by six simulation modes in July, 2013. Each dot represents a grid on the model surface, and the yellow, blue, and green dots represent the crop, grass, and (needle-leaf evergreen) forest types, respectively.

forests with their large LAI and highest over crops. Soil moisture affects the ground temperature, which increases with drier soil and thus also H_G. When soil moisture approaches its minimum (no further supply by groundwater), H_G no longer varies with WTD. With the simulation modes with the (higher) dynamic LAI (TLAI), less radiation reaches the ground, hence H_G is very small.

The transition zone of sensible heat flux is only observed by the JS-type (Figure 5.8), which can be explained by the composition of H. For the JS-type, both H_V and H_G show the transition zone, but not for the BB-type. For the BB-type, the behaviour of H is determined by

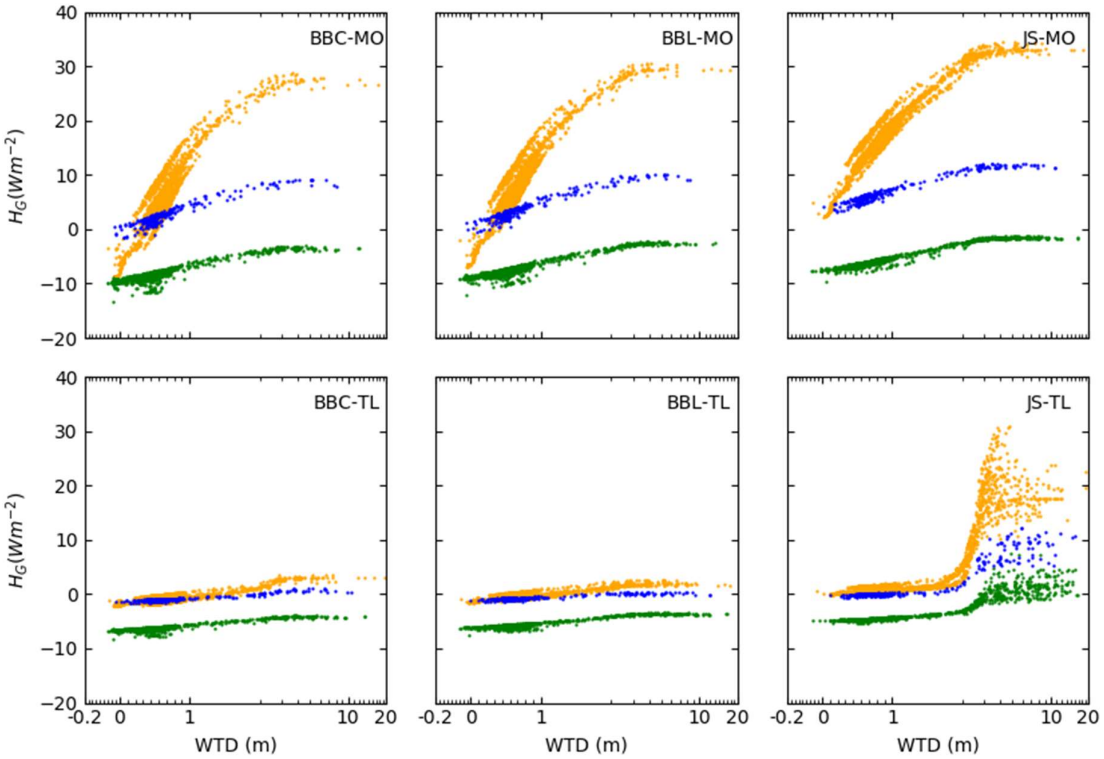

Figure 5.10. The scatter plots of monthly average sensible heat flux from the ground H_G against water table depth (WTD) by six simulation modes in July, 2013. Each dot represents a grid on the model surface, and the yellow, blue, and green dots represent the crop, grass, and (needle-leaf evergreen) forest types, respectively.

H_G, which varies with WTD by the MO simulation mode but not for the TL simulation mode.

The Bowen Ratio represents the moisture condition at a site (**Figure 5.11**). Generally, the Bowen Ratio increase with the increase of WTD, which indicates the site condition is drier with the higher WTD. The transition zone of Bowen Ratio is not observed in the results employing the BB-type equations but is observed in the results employing the JS-type equation. The uncertainty of vegetation scheme also propagates to Bowen Ratio.

Net radiation does not vary significantly between all six simulation modes as discussed in Section 4.3 (**Figure 5.12**). Different LAI values results different energy absorbed by leaf surface (Equation 2.4), and hence net radiation increases slightly by grass type, which has a significant increase of LAI from 1.9 to 4.6.

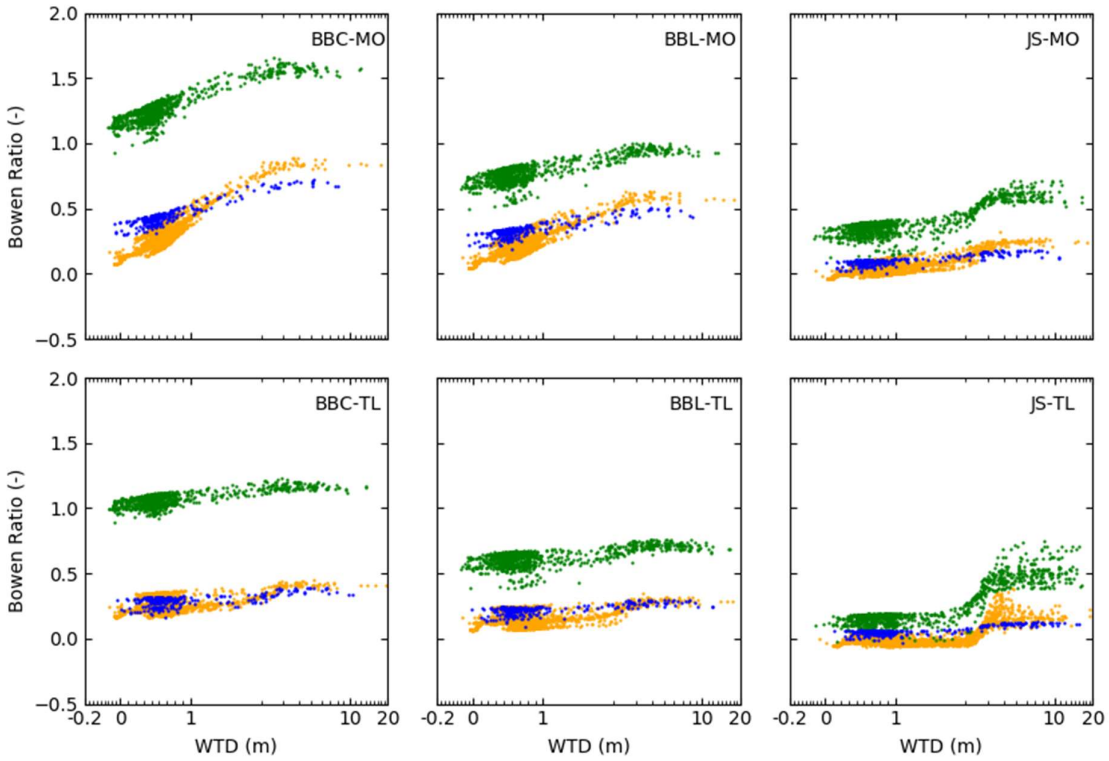

Figure 5.11. The scatter plots of monthly average Bowen Ratio against water table depth (WTD) by six simulation modes in July, 2013. Each dot represents a grid on the model surface, and the yellow, blue, and green dots represent the crop, grass, and (needle-leaf evergreen) forest types, respectively.

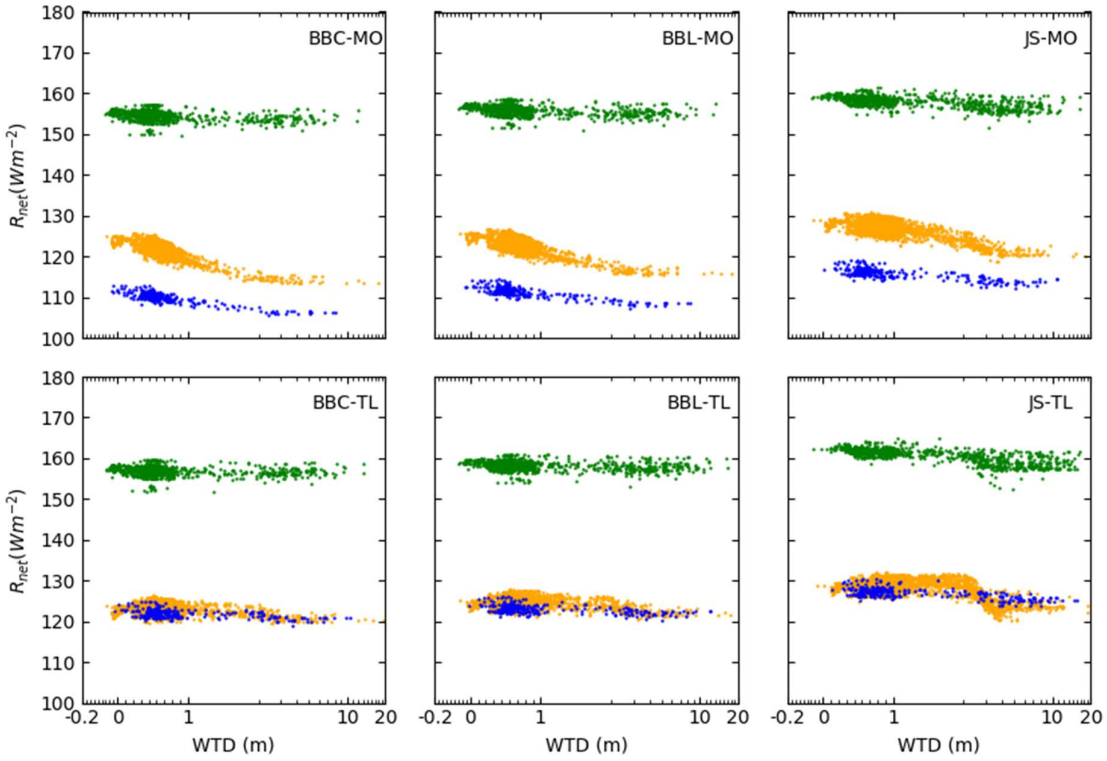

Figure 5.12. The scatter plots of monthly average net radiation R_{net} against water table depth (WTD) by six simulation modes in July, 2013. Each dot represents a grid on the model surface, and the yellow, blue, and green dots represent the crop, grass, and (needle-leaf evergreen) forest types, respectively.

5.4 Discussion

In this chapter, we extend the propagation from the land surface demonstrated in the previous chapter, to the subsurface using a coupled model system, which includes a land surface model and a groundwater model. Using this coupled model, we can study how the change in the depth of the water (WTD) affects heat fluxes, and demonstrate that the key vegetation uncertainty propagation is the soil moisture limitation factor. In the water-unlimited and water-limited zones, the heat fluxes do not change with WTD since soil water is sufficient and insufficient respectively, for water transportation from the subsurface. Within the transition zone, located between the water-unlimited and water-limited zones of the subsurface, the heat fluxes change strongly with the change in WTD. Therefore, we can successfully analyze how heat fluxes are affected by WTD in the coupled system.

The soil water limitation factor is determined by the soil moisture and root distribution, which has uncertainty in its formulation. Niu *et al.* (2011) demonstrated that root distribution employed by Noah-MP performs better latent heat flux than that employed by CLM3.5, and showed that latent heat flux is affected by root distribution uncertainty. Condon & Maxwell (2016) also observed that transpiration interacts with WTD in a deeper depth than evaporation (latent heat flux on the ground). The mechanisms of transpiration and evaporation in the transition zone are different. Evaporation depends on the depth to the surface (i.e. water escapes from the surface), and transpiration depends on the depth to the deeper depth, or the root zone (i.e. water transport by root uptake). The root zone is also controlled by root distribution, and therefore we can see how the root distribution uncertainty affects transpiration. Vegetation uncertainty propagates to the coupled system through the soil water limitation factor, which is controlled by root distribution uncertainty.

In 2012 the Rur catchment is in wet condition, and the results show that the soil water limitation factor equals one, i.e. an only water-unlimited condition in this system. Therefore, the heat fluxes do not change with WTD. In 2013, the Rur catchment is in a dry condition, and the soil water changes from unlimited condition to limited condition. Hence evaporation and transpiration affected by soil water change with WTD, and then heat fluxes also change with WTD in the transition zone. Kollet & Maxwell (2008) and Rihani *et al.* (2010) simulate the coupled model system under a semi-arid condition, and observe that heat fluxes are affected

by WTD. Therefore, the effect of WTD on heat fluxes in the unlimited, and limited water, and the transitional condition is observed more in the dry condition. In our case, the Rur catchment in 2013 is in a binary condition, a wet condition for the BB-type and a dry condition for the JS-type. The soil moisture by the JS-type reaches water-limited condition and a clear relation of latent heat flux with WTD is shown. For the BB-type, the soil moisture does not reach the water-limited condition and thus the relation is not clear. In a semi-arid climate condition, which causes a drier soil moisture condition, both Kollet & Maxwell (2008) and Rihani *et al.* (2010) simulate the coupled model system with the BB-type and observe a clear relation between heat flux with WTD in the transition zone. Therefore, if the BB-type is employed, the effect of WTD on latent heat flux requires a drier soil moisture condition. The JS-type stomatal conductance reproduces higher transpiration and results in lower soil moisture. Thus, the soil moisture reaches a water-limited condition and shows a clear relation between latent heat flux and WTD.

Pitman (2003) indicates that where a root scheme is not fully developed, it causes uncertainty in LSMs. To overcome this uncertainty, the formulation of a root distribution may be improved by employing a simple dynamic root distribution as a function of biomass (Arora & Boer, 2003). Schenk & Jackson (2002) also show that root depth and root size are correlated with precipitation and potential evapotranspiration by different vegetation types. However, both improvements in root distribution were not applicable until now, and most LSMs still employ the simplified root distribution formulation.

Chapter 6

Conclusions and outlook

The parameterization of vegetation in land-atmosphere models creates a large source of uncertainty in the exchange of heat, water and momentum in coupled terrestrial models used for weather prediction and climate projections. The land surface model CLM3.5 and its coupled model to the groundwater model Parflow, Parflow-CLM3.5 (PF-CLM3.5), are employed to quantify this uncertainty by performing simulations with three commonly used stomatal conductance equations and two LAI input types. The three considered stomatal conductance equations are the Jarvis-Stewart (JS) type and the two versions of the Ball-Berry-type (BB-type), including the Ball-Berry-Collatz (BBC) type and the Ball-Berry-Leuning (BBL) type. The two considered LAI input types are the observation-based MODIS LAI and the results of a simple dynamic LAI equation based mainly on the simulated ground temperature.

First the uncertainties are evaluated for the 1D CLM3.5 model over four sites with different vegetation cover: the grass site Rollesbroich (RO), the two crop sites Merzenhausen and Selhausen (MZ and SE), and the forest site Wüstebach (WU) in the Rur catchment close to the western border of Germany. The results of the simulations driven with observed meteorological forcing data for the years 2012 (wet year) and 2013 (dry year) are also compared to observations to estimate the realism of the schemes. Then simulations with the coupled model PF-CLM3.5, which includes a 3D hydrological model, are performed over the whole Rur Catchment to study the impact of the vegetation uncertainty on the state of the subsurface and its repercussions on the exchange fluxes.

Before the evaluation of the six variations of CLM3.5 the effects of both the original and updated (Sulis *et al.*, 2015) physiological parameter sets are compared in the framework of the first study, which clearly suggest the use of the updated ones. The employment of both

parameter sets result in comparably good simulated ground temperature and net radiation, the updated parameter set leads to largely improved latent heat flux predictions at the expense of very slightly deteriorated sensible heat flux predictions when compared to observations. The difference between the results by the BBC- and the BBL-type equations are comparatively small.

Overall, the first study shows that the simulated net radiation and ground temperatures do not differ significantly between the six simulation modes. They also do not differ much concerning the simulation of soil moisture, although clear biases are observed between the simulations and the observations. Latent heat flux varies significantly between the simulation modes with comparatively small repercussions on the simulation of the sensible heat flux.

The Taylor diagrams show that the uncertainty of vegetation schemes affects standard deviation rather than correlation. The BBL-type and the JS-type show a better simulation performance of heat fluxes. The JS-type reproduces better results at grass site, and the BBL-type produces better results at crop site. At forest site, the JS-type and the BBL-type perform better for latent heat flux and sensible heat flux, respectively. The simple dynamic LAI also performs better than MODIS LAI. The IoA, as a measure of the compliance of the simulations with the observations (IoA=1 for exact compliance and IoA=0 for no skill) varies for latent heat fluxes between the worst and best result from 0.39 to 0.86; for sensible heat fluxes the IoA ranges only between 0.05 to 0.32. Generally, the JS-type coupled with the simple dynamic LAI (JS-TL) performs best for latent heat flux, while none of the six modes consistently performs best for sensible heat flux. Results are clearest for the grass site in Rollesbroich, while more variable results are obtained for the crop sites in Selhausen and Merzenhausen, where sowing and harvesting of winter wheat and potatoes are not accurately reproduced by the two LAI simulation modes. At the forested Wüstebach site the BBL and JS simulations modes result in similar values of the IoA around 0.5 for both turbulent fluxes, which is almost independent of the LAI input. Overall, the JS-type performs better than the BBL-type formulation, but not under all weather conditions.

In the second study, we extent the propagation from the land surface to the subsurface by the coupled model system, Parflow-CLM3.5. We also demonstrate that the key of vegetation uncertainty propagating to the subsurface is the soil water limitation factor, which is determined by root distribution and soil moisture. The different results of simulation modes

depend differently on the simulated soil moisture. the Rur catchment in 2013 is a binary soil moisture condition, a wet condition for the BB-type and a dry condition for the JS-type. The stomatal conductance of the BB-type does not change with WTD in the year 2013 because the simulated soil moistures remain in soil moisture-unlimited conditions. The same soil moistures partially reach already soil moisture-limited conditions for the JS-type resulting in the typical WTD – latent heat flux relations when crossing from soil water-unlimited to the soil water-limited states. Overall, this part of the study clearly shows that the uncertainty of vegetation schemes generated by the different stomatal conductance equations and their reaction to atmospheric and soil moisture propagates into the coupled terrestrial system and also feeds back to the soil water content.

In this thesis, we demonstrate that both stomatal conductance equations and LAI input types affect the LSM calculation significantly, but the stomatal conductance equations have more impact on the LSM than LAI. Multiple solutions can exist since vegetation scheme are not solved by the first principle. Based on our results and numerous past studies, we propose that the BB-type and the JS-type are two different approaching ways to the real world. The JS-type and BB-type are top-down and bottom-up approaches, respectively, and both of them can well approach the real world. However, both formulations are dynamic, and the comparison between the BB-type and the JS-type is unreasonable. Instead of judging which equation is the best, we shall ask how to approach the real world by the two well-accepted stomatal conductance equations to reduce the vegetation uncertainty in the land-atmosphere interaction.

We also demonstrate that, via groundwater model Parflow, the simulation of 3D land model is achieved by the connection between land surface and the subsurface processes. However, a comprehensive measurement of 3D groundwater and eddy covariance measurement are needed as a future work. The comparison between observation and simulation is valuable to understand and to improve the accuracy of simulation of land-atmospheric interaction in the terrestrial system.

Reference

Abbott MB., Bathurst JC., Cunge JA., O'Connell PE., Rasmussen J. 1986. An introduction to the European Hydrological System – Systeme Hydrologique Europeen, "SHE", 1: History and philosophy of a physically-based, distributed modelling system. **87**:45–59.

Addington RN., Mitchell RJ., Oren R., Donovan LA. 2004. Stomatal sensitivity to vapor pressure deficit and its relationship to hydraulic conductance in Pinus palustris. *Tree Physiol.* **24**:561–569.

Allen RG., Pruitt WO., Wright JL., Howell TA., Ventura F., Snyder R., Itenfisu D., Steduto P., Berengena J., Yrisarry JB., Smith M., Pereira LS., Raes D., Perrier A., Alves I., Walter I., Elliott R. 2006. A recommendation on standardized surface resistance for hourly calculation of reference ETo by the FAO56 Penman-Monteith method. **81**:1–22.

Anderson DB. 1936. Relative humidity or vapor pressure deficit. *Ecology* **17**:277–282.

Aphalo PJ., Jarvis PG. 1993. An Analysis of Ball's Empirical Model of Stomatal Conductance. *Ann. Bot.* **72**:321–327.

Arora V. 2002. Modeling Vegetation as a Dynamic Component in Soil-Vegetation-Atmosphere Transfer Schemes and HyHydrologic Models. *Rev Geophys* **40**:1006–.

Arora VK., Boer GJ. 2003. A Representation of Variable Root Distribution in Dynamic Vegetation Models. *Earth Interact* **7**:1–19.

Ashby SF., Falgout RD. 1996. A parallel multigrid preconditioned conjugate gradient algorithm for groundwater flow simulations. *Nucl Sci Eng* **124(1)**:145–159.

Baldauf M., Seifert A., Förstner J., Majewski D., Raschendorfer M., Reinhardt T. 2011. Operational Convective-Scale Numerical Weather Prediction with the COSMO Model: Description and Sensitivities. *Mon Wea Rev* **139**:3887–3905.

Ball JT., Woodrow IE., Berry JA. 1987. A model predicting stomatal conductance and its contribution to the control of photosynthesis under different environmental conditions. In: *Progress in photosynthesis research*. Springer, 221–224.

Barradas VL., Fanjul L. 1986. Microclimatic chacterization of shaded and open-grown coffee (Coffea arabica L.) plantations in Mexico. **38**:101–112.

Beerling DJ. 2015. Gas valves, forests and global change: a commentary on Jarvis (1976) "The interpretation of the variations in leaf water potential and stomatal conductance found in canopies in the field." *Philos Trans R Soc Lond B Biol Sci* **370**.

Berg A., Findell K., Lintner B., Giannini A., Seneviratne SI., van den Hurk B., Lorenz R., Pitman A., Hagemann S., Meier A., Cheruy F., Ducharne A., Malyshev S., Milly PCD. 2016. Land-atmosphere feedbacks amplify aridity increase over land under global warming. *Nat. Clim Change* **6**:869–874.

Best MJ., Abramowitz G., Johnson HR., Pitman AJ., Balsamo G., Boone A., Cuntz M., Decharme B., Dirmeyer PA., Dong J., Ek M., Guo Z., Haverd V., van den Hurk BJJ., Nearing GS., Pak B., Peters-Lidard C., Santanello JA., Stevens L., Vuichard N. 2015. The Plumbing of Land Surface Models: Benchmarking Model Performance. *J Hydrometeor* **16**:1425–1442.

Best MJ., Pryor M., Clark DB., Rooney GG., Essery RLH., Ménard CB., Edwards JM., Hendry MA., Porson A., Gedney N., Mercado LM., Sitch S., Blyth E., Boucher O., Cox PM., Grimmond CSB., Harding RJ. 2011. The Joint UK Land Environment Simulator (JULES), model description - Part 1: Energy and water fluxes. *Geosci Model Dev* **4**:677–699.

Bonan GB. 1996. *Land surface model (LSM version 1.0) for ecological, hydrological, and atmospheric studies: Technical description and users guide. Technical note*. National Center for Atmospheric Research, Boulder, CO (United States). Climate and Global Dynamics Div.

Bonan GB. 2008. Forests and Climate Change: Forcings, Feedbacks, and the Climate Benefits of Forests. *Science* **320**:1444–1449.

Bonan GB., Williams M., Fisher RA., Oleson KW. 2014. Modeling stomatal conductance in the earth system: linking leaf water-use efficiency and water transport along the soil-plant-atmosphere continuum. *Geosci Model Dev* **7**:2193–2222.

Boone A., Habets F., Noilhan J., Clark D., Dirmeyer P., Fox S., Gusev Y., Haddeland I., Koster R., Lohmann D. 2004. The Rhone-Aggregation land surface scheme intercomparison project: An overview. *J. Clim.* **17**:187–208.

Brut A., Rüdiger C., Lafont S., Roujean J-L., Calvet J-C., Jarlan L., Gibelin A-L., Albergel C., Le Moigne P., Soussana J-F., Klumpp K., Guyon D., Wigneron J-P., Ceschia E. 2009. Modelling LAI at a regional scale with ISBA-A-gs: comparison with satellite-derived LAI over southwestern France. *Biogeosciences* **6**:1389–1404.

Buckingham E. 1907. Studies on the movement of soil moisture.

Cai X., Yang Z-L., David CH., Niu G-Y., Rodell M. 2014. Hydrological evaluation of the Noah-MP land surface model for the Mississippi River Basin. *J Geophys Res Atmos* **119**:23–38.

Chen JM., Rich PM., Gower ST., Norman JM., Plummer S. 1997. Leaf area index of boreal forests: Theory, techniques, and measurements. *J Geophys Res* **102**:29429–29443.

Clapp RB., Hornberger GM. 1978. Empirical equations for some soil hydraulic properties. *Water Resour Res* **14**:601–604.

Clark DB., Mercado LM., Sitch S., Jones CD., Gedney N., Best MJ., Pryor M., Rooney GG., Essery RLH., Blyth E., Boucher O., Harding RJ., Huntingford C., Cox PM. 2011. The Joint UK Land Environment Simulator (JULES), model description - Part 2: Carbon fluxes and vegetation dynamics. *Geosci Model Dev* **4**:701–722.

Collatz GJ., Ball JT., Grivet C., Berry JA. 1991. Physiological and environmental regulation of stomatal conductance, photosynthesis and transpiration: a model that includes a laminar boundary layer. *Agric. For. Meteorol.* **54**:107–136.

Cosby BJ., Hornberger GM., Clapp RB., Ginn TR. 1984. A Statistical Exploration of the Relationships of Soil Moisture Characteristics to the Physical Properties of Soils. *Water Resour Res* **20**:682–690.

Cox PM., Huntingford C., Harding RJ. 1998. A canopy conductance and photosynthesis model for use in a GCM land surface scheme. **212–213**:79–94.

Cuenca RH., Ek M., Mahrt L. 1996. Impact of soil water property parameterization on atmospheric boundary layer simulation. *J Geophys Res* **101**:7269–7277.

Cuntz M., Mai J., Samaniego L., Clark M., Wulfmeyer V., Attinger S., Thober S. 2016. Impact of

the hard-coded parameters on the hydrologic fluxes of the land surface model Noah-MP. In: *EGU General Assembly Conference Abstracts*. 5899.

Dai Y., Zeng Q. 1997. A land surface model (IAP94) for climate studies part I: Formulation and validation in off-line experiments. *Adv. Atmospheric Sci.* **14**:433–460.

Dai Y., Zeng X., Dickinson RE., Baker I., Bonan GB., Bosilovich MG., Denning AS., Dirmeyer PA., Houser PR., Niu G. 2003. The common land model. *Bull. Am. Meteorol. Soc.* **84**.

Damour G., Simonneau T., Cochard H., Urban L. 2010. An overview of models of stomatal conductance at the leaf level. *Plant Cell Environ.* **33**:1419–1438.

Desborough CE. 1997. The Impact of Root Weighting on the Response of Transpiration to Moisture Stress in Land Surface Schemes. *Mon Wea Rev* **125**:1920–1930.

Dickinson RE. 1983. Land Surface Processes and Climate–Surface Albedos and Energy Balance. In: Saltzman B ed. *Advances in Geophysics*. Elsevier, 305–353.

Dickinson RE., Henderson-Sellers A. 1988. Modelling tropical deforestation: A study of GCM land-surface parametrizations. *QJR Meteorol Soc* **114**:439–462.

Dickinson RE., Henderson-Sellers A., Rosenzweig C., Sellers PJ. 1991. Evapotranspiration models with canopy resistance for use in climate models, a review. **54**:373–388.

Dickinson RE., Kennedy P., Henderson-Sellers A. 1993a. *Biosphere-atmosphere transfer scheme (BATS) version 1e as coupled to the NCAR community climate model*. National Center for Atmospheric Research, Climate and Global Dynamics Division.

Dickinson RE., Kennedy PJ., Henderson-Sellers A. 1993b. *Biosphere-atmosphere transfer scheme (BATS) version 1e as coupled to the NCAR community climate model*. National Center for Atmospheric Research, Climate and Global Dynamics Division.

Dickinson RE., Shaikh M., Bryant R., Graumlich L. 1998. Interactive Canopies for a Climate Model. *J Clim.* **11**:2823–2836.

Ek MB., Mitchell KE., Lin Y., Rogers E., Grunmann P., Koren V., Gayno G., Tarpley JD. 2003. Implementation of Noah land surface model advances in the National Centers for Environmental Prediction operational mesoscale Eta model. *J Geophys Res* **108**:8851–.

Ewert F. 2004. Modelling Plant Responses to Elevated CO2: How Important is Leaf Area Index? *Ann. Bot.* **93**:619–627.

Farquhar GD., von Caemmerer S., Berry JA. 1980. A biochemical model of photosynthetic CO2 assimilation in leaves of C3 species. *Planta* **149**:78–90.

Farquhar GD., von Caemmerer S., Berry JA. 2001. Models of Photosynthesis. *Plant Physiol.* **125**:42–45.

Feddes RA., Hoff H., Bruen M., Dawson T., de Rosnay P., Dirmeyer P., Jackson RB., Kabat P., Kleidon A., Lilly A., Pitman AJ. 2001. Modeling Root Water Uptake in Hydrological and Climate Models. *Bull Amer Meteor Soc* **82**:2797–2809.

Foken T. 2006. 50 years of the Monin-Obukhov similarity theory. *Bound.-Layer Meteorol.* **119**:431–447.

Foley JA., Prentice IC., Ramankutty N., Levis S., Pollard D., Sitch S., Haxeltine A. 1996. An integrated biosphere model of land surface processes, terrestrial carbon balance, and

vegetation dynamics. *Glob. Biogeochem Cycles* **10**:603–628.

Garratt JR. 1993. Sensitivity of Climate Simulations to Land-Surface and Atmospheric Boundary-Layer Treatments-A Review. *J Clim.* **6**:419–448.

Garrett AJ. 1982. A Parameter Study of Interactions Between Convective Clouds, the Convective Boundary Layer, and a Forested Surface. *Mon Wea Rev* **110**:1041–1059.

Garrigues S., Lacaze R., Baret F., Morisette JT., Weiss M., Nickeson JE., Fernandes R., Plummer S., Shabanov NV., Myneni RB., Knyazikhin Y., Yang W. 2008. Validation and intercomparison of global Leaf Area Index products derived from remote sensing data. *J Geophys Res* **113**:G02028–.

Gasper F., Goergen K., Shrestha P., Sulis M., Rihani J., Geimer M., Kollet S. 2014. Implementation and scaling of the fully coupled Terrestrial Systems Modeling Platform (TerrSysMP v1.0) in a massively parallel supercomputing environment - a case study on JUQUEEN (IBM Blue Gene/Q). *Geosci Model Dev* **7**:2531–2543.

Gleeson T., Smith L., Moosdorf N., Hartmann J., Dürr HH., Manning AH., van Beek LPH., Jellinek AM. 2011. Mapping permeability over the surface of the Earth. *Geophys Res Lett* **38**:n/a–n/a.

Gower ST., Kucharik CJ., Norman JM. 1999. Direct and Indirect Estimation of Leaf Area Index, fAPAR, and Net Primary Production of Terrestrial Ecosystems. **70**:29–51.

Graf A., Bogena HR., Drüe C., Hardelauf H., Pütz T., Heinemann G., Vereecken H. 2014. Spatiotemporal relations between water budget components and soil water content in a forested tributary catchment. *Water Resour Res* **50**:4837–4857.

Granier A., Loustau D., Bréda N. 2000. A generic model of forest canopy conductance dependent on climate, soil water availability and leaf area index. *Ann Sci* **57**:755–765.

Graßelt R. 2009. *Validation of the COSMO Land-Surface Parameterization TERRA-ML with discharge measurements*. Germany: Universitäts-und Landesbibliothek Bonn.

Haxeltine A., Prentice IC., Creswell ID. 1996. A coupled carbon and water flux model to predict vegetation structure. *J. Veg. Sci.* **7**:651–666.

Hetherington AM., Woodward FI. 2003. The role of stomata in sensing and driving environmental change. *Nature* **424**:901–908.

Hoshika Y., Fares S., Savi F., Gruening C., Goded I., De Marco A., Sicard P., Paoletti E. 2017. Stomatal conductance models for ozone risk assessment at canopy level in two Mediterranean evergreen forests. *Agric. For. Meteorol.* **234**:212–221.

Hou Z., Huang M., Leung LR., Lin G., Ricciuto DM. 2012. Sensitivity of surface flux simulations to hydrologic parameters based on an uncertainty quantification framework applied to the Community Land Model. *J Geophys Res* **117**:D15108.

Jacquemin B., Noilhan J. 1990. Sensitivity study and validation of a land surface parameterization using the HAPEX-MOBILHY data set. *Bound.-Layer Meteorol.* **52**:93–134.

Jarvis PG. 1976. The Interpretation of the Variations in Leaf Water Potential and Stomatal Conductance Found in Canopies in the Field. *Philos. Trans. R. Soc. Lond. B Biol. Sci.* **273**:593–610.

Jefferson JL., Gilbert JM., Constantine PG., Maxwell RM. 2015. Active subspaces for sensitivity

analysis and dimension reduction of an integrated hydrologic model. **83**:127–138.

Jiang X., Niu G-Y., Yang Z-L. 2009. Impacts of vegetation and groundwater dynamics on warm season precipitation over the Central United States. *J Geophys Res* **114**:D06109.

Jonckheere I., Fleck S., Nackaerts K., Muys B., Coppin P., Weiss M., Baret F. 2004. Review of methods for in situ leaf area index determination: Part I. Theories, sensors and hemispherical photography. *Agric. For. Meteorol.* **121**:19–35.

Jones JE., Woodward CS. 2001. Newton-Krylov-multigrid solvers for large-scale, highly heterogeneous, variably saturated flow problems. **24**:763–774.

Jung M., Reichstein M., Ciais P., Seneviratne SI., Sheffield J., Goulden ML., Bonan G., Cescatti A., Chen J., de Jeu R., Dolman AJ., Eugster W., Gerten D., Gianelle D., Gobron N., Heinke J., Kimball J., Law BE., Montagnani L., Mu Q., Mueller B., Oleson K., Papale D., Richardson AD., Roupsard O., Running S., Tomelleri E., Viovy N., Weber U., Williams C., Wood E., Zaehle S., Zhang K. 2010. Recent decline in the global land evapotranspiration trend due to limited moisture supply. *Nature* **467**:951–954.

Kauwe D., M. G., Kala J., Lin Y-S., Pitman AJ., Medlyn BE., Duursma RA., Abramowitz G., Wang Y-P., Miralles DG. 2015. A test of an optimal stomatal conductance scheme within the CABLE land surface model. *Geosci Model Dev* **8**:431–452.

Kergoat L. 1998. A model for hydrological equilibrium of leaf area index on a global scale. **212**–**213**:268–286.

Kollet SJ., Maxwell RM. 2006. Integrated surface-groundwater flow modeling: A free-surface overland flow boundary condition in a parallel groundwater flow model. **29**:945–958.

Kollet SJ., Maxwell RM. 2008. Capturing the influence of groundwater dynamics on land surface processes using an integrated, distributed watershed model. *Water Resour Res* **44**:W02402.

Kowalczyk EA., Wang YP., Law RM., Davies HL., McGregor JL., Abramowitz G. 2006. *The CSIRO Atmosphere Biosphere Land Exchange (CABLE) model for use in climate models and as an offline model*. CSIRO Marine and Atmospheric Research.

Krishnan P., Black TA., Grant NJ., Barr AG., Hogg E (Ted) H., Jassal RS., Morgenstern K. 2006. Impact of changing soil moisture distribution on net ecosystem productivity of a boreal aspen forest during and following drought. **139**:208–223.

Lam A., Karssenberg D., van den Hurk BJJM., Bierkens MFP. 2011. Spatial and temporal connections in groundwater contribution to evaporation. *Hydrol. Earth Syst. Sci. Discuss.* **8**:1541–1568.

Langensiepen M., Fuchs M., Bergamaschi H., Moreshet S., Cohen Y., Wolff P., Jutzi SC., Cohen S., Rosa LMG., Li Y., Fricke T. 2009. Quantifying the uncertainties of transpiration calculations with the Penman-Monteith equation under different climate and optimum water supply conditions. **149**:1063–1072.

Lawrence PJ., Chase TN. 2007. Representing a new MODIS consistent land surface in the Community Land Model (CLM 3.0). *J Geophys Res* **112**:n/a–n/a.

Legates DR., McCabe GJ. 1999. Evaluating the use of “goodness-of-fit” Measures in hydrologic and hydroclimatic model validation. *Water Resour Res* **35**:233–241.

Leuning R. 1995. A critical appraisal of a combined stomatal-photosynthesis model for C3 plants. *Plant Cell Environ.* **18**:339–355.

Levis S., Bonan GB., Vertenstein M., Oleson KW. 2004. The Community Land Model's dynamic global vegetation model (CLM-DGVM): Technical description and user's guide. *NCAR Tech Note TN-459 IA* **50**.

Li S-G., Lai C-T., Lee G., Shimoda S., Yokoyama T., Higuchi A., Oikawa T. 2005. Evapotranspiration from a wet temperate grassland and its sensitivity to microenvironmental variables. *Hydrol Process* **19**:517–532.

Liang X., Lettenmaier DP., Wood EF., Burges SJ. 1994. A simple hydrologically based model of land surface water and energy fluxes for general circulation models. *J Geophys Res* **99**:14415–14428.

Lin Y-S., Medlyn BE., Duursma RA., Prentice IC., Wang H., Baig S., Eamus D., de Dios VR., Mitchell P., Ellsworth DS., de Beeck MO., Wallin G., Uddling J., Tarvainen L., Linderson M-L., Cernusak LA., Nippert JB., Ocheltree TW., Tissue DT., Martin-StPaul NK., Rogers A., Warren JM., De Angelis P., Hikosaka K., Han Q., Onoda Y., Gimeno TE., Barton CVM., Bennie J., Bonal D., Bosc A., Low M., Macinins-Ng C., Rey A., Rowland L., Setterfield SA., Tausz-Posch S., Zaragoza-Castells J., Broadmeadow MSJ., Drake JE., Freeman M., Ghannoum O., Hutley LB., Kelly JW., Kikuzawa K., Kolari P., Koyama K., Limousin J-M., Meir P., Lola da Costa AC., Mikkelsen TN., Salinas N., Sun W., Wingate L. 2015. Optimal stomatal behaviour around the world. *Nat. Clim Change* **5**:459–464.

Liu S. 1997. A new model for the prediction of rainfall interception in forest canopies. **99**:151–159.

Lohammar T., Larsson S., Linder S., Falk SO. 1980. FAST: Simulation models of gaseous exchange in Scots pine. *Ecol. Bull.*:505–523.

Mai J., Thober S., Samaniego L., Branch O., Wulfmeyer V., Clark M., Attinger S., Kumar R., Cuntz M. 2015. Sensitivity Analysis of the Land Surface Model NOAH-MP for Different Model Fluxes. In: *EGU General Assembly Conference Abstracts*. 6536.

Manabe S. 1969. CLIMATE AND THE OCEAN CIRCULATION 1: I. THE ATMOSPHERIC CIRCULATION AND THE HYDROLOGY OF THE EARTH'S SURFACE. *Mon. Weather Rev.* **97**:739–774.

Martin P. 1993. Vegetation responses and feedbacks to climate: a review of models and processes. *Clim. Dyn.* **8**:201–210.

Maxwell RM., Condon LE. 2016. Connections between groundwater flow and transpiration partitioning. *Science* **353**:377–380.

Maxwell RM., Miller NL. 2005. Development of a Coupled Land Surface and Groundwater Model. *J Hydrometeor* **6**:233–247.

McMichael CE., Hope AS., Loaiciga HA. 2006. Distributed hydrological modelling in California semi-arid shrublands: MIKE SHE model calibration and uncertainty estimation. **317**:307–324.

Monin AS., Obukhov AMF. 1954. Basic laws of turbulent mixing in the surface layer of the atmosphere. *Contrib Geophys Inst Acad Sci USSR* **151**:e187.

Monteith JL. 1995. A reinterpretation of stomatal responses to humidity. *Plant Cell Environ.* **18**:357–364.

Mott KA., Parkhurst DF. 1991. Stomatal responses to humidity in air and helox. *Plant Cell Environ.* **14**:509–515.

Myneni RB. 2002. Global products of vegetation leaf area and fraction absorbed PAR from one year of MODIS data. *Remote Sens Env.* **83**:214–231.

Niu G-Y., Yang Z-L., Mitchell KE., Chen F., Ek MB., Barlage M., Kumar A., Manning K., Niyogi D., Rosero E., Tewari M., Xia Y. 2011. The community Noah land surface model with multiparameterization options (Noah-MP): 1. Model description and evaluation with local-scale measurements. *J Geophys Res* **116**:D12109.

Niyogi DS., Raman S. 1997. Comparison of Four Different Stomatal Resistance Schemes Using FIFE Observations. *J. Appl. Meteorol.* **36**:903–917.

Noilhan J., Planton S. 1989. A Simple Parameterization of Land Surface Processes for Meteorological Models. *Mon Wea Rev* **117**:536–549.

Oleson KW., Y. Dai., G. Bonan M., Bosilovich., R. Dickinson., al PD et. 2004a. Technical description on of the Community Land Model (CLM). *NCAR Tech Note 461 Natl. Cent. Atmospheric Res. Boulder CO*.

Oleson KW., Y. Dai., G. Bonan M., Bosilovich., R. Dickinson., al PD et. 2004b. Technical description on of the Community Land Model (CLM). *NCAR Tech Note 461 Natl. Cent. Atmospheric Res. Boulder CO*.

Oren R., Sperry JS., Katul GG., Pataki DE., Ewers BE., Phillips N., Schäfer KVR. 1999. Survey and synthesis of intra- and interspecific variation in stomatal sensitivity to vapour pressure deficit. *Plant Cell Environ.* **22**:1515–1526.

Pitman AJ. 2003. The evolution of, and revolution in, land surface schemes designed for climate models. *Int J Clim.* **23**:479–510.

Pitman AJ., Henderson-Sellers A., Desborough CE., Yang Z-L., Abramopoulos F., Boone A., Dickinson RE., Gedney N., Koster R., Kowalczyk E., Lettenmaier D., Liang X., Mahfouf J-F., Noilhan J., Polcher J., Qu W., Robock A., Rosenzweig C., Schlosser CA., Shmakin AB., Smith J., Suarez M., Verseghy D., Wetzel P., Wood E., Xue Y. 1999. Key results and implications from phase 1(c) of the Project for Intercomparison of Land-surface Parametrization Schemes. *Clim. Dyn.* **15**:673–684.

Pollard D., Thompson SL. 1995. Use of a land-surface-transfer scheme (LSX) in a global climate model: the response to doubling stomatal resistance. *Results Model Eval. Consort. Clim. Assess.* **10**:129–161.

Rahman M., Sulis M., Kollet SJ. 2014. The concept of dual-boundary forcing in land surface-subsurface interactions of the terrestrial hydrologic and energy cycles. *Water Resour Res* **50**:8531–8548.

Ran L., Pleim J., Song C., Band L., Walker JT., Binkowski FS. 2017. A photosynthesis-based two-leaf canopy stomatal conductance model for meteorology and air quality modeling with WRF/CMAQ PX LSM. *J Geophys Res Atmos* **122**:1930–1952.

Rana G., Katerji N., Mastrorilli M. 1998. Canopy resistance modelling for crops in contrasting water conditions. *Phys. Chem. Earth* **23**:433–438.

Reichenau TG., Korres W., Montzka C., Fiener P., Wilken F., Stadler A., Waldhoff G., Schneider

K. 2016. Spatial Heterogeneity of Leaf Area Index (LAI) and Its Temporal Course on Arable Land: Combining Field Measurements, Remote Sensing and Simulation in a Comprehensive Data Analysis Approach (CDAA). *PLoS ONE* **11**:e0158451–.

Richards LA. 1931. Capillary conduction of liquids through porous mediums. *Physics* **1**:318–333.

Rihani JF., Maxwell RM., Chow FK. 2010. Coupling groundwater and land surface processes: Idealized simulations to identify effects of terrain and subsurface heterogeneity on land surface energy fluxes. *Water Resour Res* **46**:W12523.

Ronda RJ., de Bruin HAR., Holtslag AAM. 2001. Representation of the Canopy Conductance in Modeling the Surface Energy Budget for Low Vegetation. *J Appl Meteor* **40**:1431–1444.

Rosero E., Yang Z-L., Gulden LE., Niu G-Y., Gochis DJ. 2009. Evaluating Enhanced Hydrological Representations in Noah LSM over Transition Zones: Implications for Model Development. *J Hydrometeor* **10**:600–622.

Running SW., Coughlan JC. 1988. A general model of forest ecosystem processes for regional applications I. Hydrologic balance, canopy gas exchange and primary production processes. **42**:125–154.

Running SW., Nemani RR., Peterson DL., Band LE., Potts DF., Pierce LL., Spanner MA. 1989. Mapping Regional Forest Evapotranspiration and Photosynthesis by Coupling Satellite Data with Ecosystem Simulation. *Ecology* **70**:1090–1101.

Savenije HHG. 2004. The importance of interception and why we should delete the term evapotranspiration from our vocabulary. *Hydrol Process* **18**:1507–1511.

Schenk HJ., Jackson RB. 2002. Rooting depths, lateral root spreads and below-ground/above-ground allometries of plants in water-limited ecosystems. *J. Ecol.* **90**:480–494.

Schwinger J., Kollet SJ., Hoppe CM., Elbern H. 2010. Sensitivity of Latent Heat Fluxes to Initial Values and Parameters of a Land-Surface Model. *Vadose Zone J.* **9**:984–1001.

Sellers PJ., Dickinson RE., Randall DA., Betts AK., Hall FG., Berry JA., Collatz GJ., Denning AS., Mooney HA., Nobre CA., Sato N., Field CB., Henderson-Sellers A. 1997. Modeling the Exchanges of Energy, Water, and Carbon Between Continents and the Atmosphere. *Science* **275**:502–509.

Sellers P., Mintz Y., Sud Y e al., Dalcher A. 1986a. A simple biosphere model (SiB) for use within general circulation models. *J. Atmospheric Sci.* **43**:505–531.

Sellers PJ., Mintz YCSY., Sud YC e al., Dalcher A. 1986b. A simple biosphere model (SiB) for use within general circulation models. *J. Atmospheric Sci.* **43**:505–531.

Sellers PJ., Tucker CJ., Collatz GJ., Los SO., Justice CO., Dazlich DA., Randall DA. 1996. A Revised Land Surface Parameterization (SiB2) for Atmospheric GCMS. Part II: The Generation of Global Fields of Terrestrial Biophysical Parameters from Satellite Data. *J. Clim.* **9**:706–737.

Shao Y., Henderson-Sellers A. 1996. Modeling soil moisture: A Project for Intercomparison of Land Surface Parameterization Schemes Phase 2(b). *J Geophys Res* **101**:7227–7250.

Shrestha P., Sulis M., Masbou M., Kollet S., Simmer C. 2014. A Scale-Consistent Terrestrial Systems Modeling Platform Based on COSMO, CLM, and ParFlow. *Mon Wea Rev* **142**:3466–3483.

Shrestha P., Sulis M., Simmer C., Kollet S. 2015. Impacts of grid resolution on surface energy fluxes simulated with an integrated surface-groundwater flow model. *Hydrol Earth Syst Sci* **19**:4317–4326.

Shukla J., Mintz Y. 1982. Influence of Land-Surface Evapotranspiration on the Earth's Climate. *Science* **215**:1498–1501.

Simmer C., Thiele-Eich I., Masbou M., Amelung W., Bogena H., Crewell S., Diekkrüger B., Ewert F., Hendricks Franssen H-J., Huisman JA., Kemna A., Klitzsch N., Kollet S., Langensiepen M., Löhnert U., Rahman ASMM., Rascher U., Schneider K., Schween J., Shao Y., Shrestha P., Stiebler M., Sulis M., Vanderborght J., Vereecken H., van der Kruk J., Waldhoff G., Zerenner T. 2015. Monitoring and Modeling the Terrestrial System from Pores to Catchments: The Transregional Collaborative Research Center on Patterns in the Soil-Vegetation-Atmosphere System. *Bull Amer Meteor Soc* **96**:1765–1787.

Sitch S., Smith B., Prentice IC., Arneth A., Bondeau A., Cramer W., Kaplan JO., Levis S., Lucht W., Sykes MT., Thonicke K., Venevsky S. 2003. Evaluation of ecosystem dynamics, plant geography and terrestrial carbon cycling in the LPJ dynamic global vegetation model. *Glob. Change Biol.* **9**:161–185.

Steduto P., Hsiao TC. 1998. Maize canopies under two soil water regimes: II. Seasonal trends of evapotranspiration, carbon dioxide assimilation and canopy conductance, and as related to leaf area index. **89**:185–200.

Steppeler J., Doms G., Schättler U., Bitzer HW., Gassmann A., Damrath U., Gregoric G. 2003. Meso-gamma scale forecasts using the nonhydrostatic model LM. *Meteorol. Atmospheric Phys.* **82**:75–96.

Stewart JB. 1988. Modelling surface conductance of pine forest. **43**:19–35.

Stewart JB., Verma SB. 1992. Comparison of surface fluxes and conductances at two contrasting sites within the FIFE area. *J Geophys Res* **97**:18623–18628.

Sulis M., Langensiepen M., Shrestha P., Schickling A., Simmer C., Kollet SJ. 2015. Evaluating the Influence of Plant-Specific Physiological Parameterizations on the Partitioning of Land Surface Energy Fluxes. *J Hydrometeor* **16**:517–533.

Taylor KE. 2001. Summarizing multiple aspects of model performance in a single diagram. *J Geophys Res* **106**:7183–7192.

Thornton PE., Rosenbloom NA. 2005. Ecosystem model spin-up: Estimating steady state conditions in a coupled terrestrial carbon and nitrogen cycle model. **189**:25–48.

Tian Y., Dickinson RE., Zhou L., Zeng X., Dai Y., Myneni RB., Knyazikhin Y., Zhang X., Friedl M., Yu H., Wu W., Shaikh M. 2004. Comparison of seasonal and spatial variations of leaf area index and fraction of absorbed photosynthetically active radiation from Moderate Resolution Imaging Spectroradiometer (MODIS) and Common Land Model. *J Geophys Res* **109**:D01103–.

Tian W., Li X., Cheng G-D., Wang X-S., Hu BX. 2012. Coupling a groundwater model with a land surface model to improve water and energy cycle simulation. *Hydrol Earth Syst Sci* **16**:4707–4723.

Troen IB., Mahrt L. 1986. A simple model of the atmospheric boundary layer; sensitivity to

surface evaporation. *Bound.-Layer Meteorol.* **37**:129–148.

Valcke S. 2013. The OASIS3 coupler: a European climate modelling community software. *Geosci Model Dev* **6**:373–388.

van Genuchten. 1980. A closed-form equation for predicting the hydraulic conductivity of unsaturated soils. *Soil Sci Soc Am J* **44**:892–898.

Van Wijk MT., Dekker SC., Bouten W., Bosveld FC., Kohsiek W., Kramer K., Mohren GMJ. 2000. Modeling daily gas exchange of a Douglas-fir forest: comparison of three stomatal conductance models with and without a soil water stress function. *Tree Physiol.* **20**:115–122.

Vereecken H., Kollet S., Simmer C. 2010. Patterns in Soil-Vegetation-Atmosphere Systems: Monitoring, Modeling, and Data Assimilation All rights reserved. No part of this periodical may be reproduced or transmitted in any form or by any means, electronic or mechanical, including photocopying, recording, or any information storage and retrieval system, without permission in writing from the publisher. *Vadose Zone J.* **9**:821–827.

Wang Y-P., Leuning R. 1998. A two-leaf model for canopy conductance, photosynthesis and partitioning of available energy I:: Model description and comparison with a multi-layered model. **91**:89–111.

Xiu A., Pleim JE. 2001. Development of a Land Surface Model. Part I: Application in a Mesoscale Meteorological Model. *J Appl Meteor* **40**:192–209.

Yang Z-L., Dickinson RE., Henderson-Sellers A., Pitman AJ. 1995. Preliminary study of spin-up processes in land surface models with the first stage data of Project for Intercomparison of Land Surface Parameterization Schemes Phase 1(a). *J Geophys Res* **100**:16553–16578.

Yin X., Schapendonk AHCM., Kropff MJ., van Oijen M., Bindraban PS. 2000. A Generic Equation for Nitrogen-limited Leaf Area Index and its Application in Crop Growth Models for Predicting Leaf Senescence. *Ann. Bot.* **85**:579–585.

York JP., Person M., Gutowski WJ., Winter TC. 2002. Putting aquifers into atmospheric simulation models: an example from the Mill Creek Watershed, northeastern Kansas. *Adv. Water Resour.* **25**:221–238.

Zeng X. 2001. Global Vegetation Root Distribution for Land Modeling. *J Hydrometeor* **2**:525–530.

List of Figures

List of Tables

Appendix I

Namelist of Land Surface Model

LSM Abbreviation	Full Name	Reference
	First Generation LSM	
Manabe LSM	-	(Manabe, 1969)
	Second Generation LSM	
OSU LSM	**O**regon **S**tate **U**niversity **LSM**	(Troen & Mahrt, 1986)
SiB	**S**imple **B**iosphere **M**odel	(Sellers *et al.*, 1986a)
FOREST-BGC	**Forest**-**B**io**G**eochemical **C**ycles	(Running & Coughlan, 1988)
BATS	**B**iosphere-**A**tmosphere **T**ransfer **S**cheme	(Dickinson *et al.*, 1984)
SHE	**S**ysteme **H**ydrologique **E**uropeen	(Abbott *et al.*, 1986)
VIC	**V**ariable **I**nfiltration **C**apacity	(Liang *et al.*, 1994)
Bonan LSM	-	(Bonan, 1996)
IAP94	Chinese Academy of Science **I**nstitute of **A**tmospheric **P**hysics LSM (19**94**)	(Dai & Zeng, 1997)
LSX	**L**and-**S**urface Transfer Model	(Pollard & Thompson, 1995)
OSU-CAPS	**OSU C**oupled **A**tmosphere-**P**lant-**S**oil	(Cuenca *et al.*, 1996)

Third Generation LSM

IBIS	**I**ntegrated **B**iosphere **S**imulator	(Foley *et al.*, 1996)
SiB2	**Si**mple **B**iosphere (with new parameterization)	(Sellers *et al.*, 1996)
PX-LSM	**P**leim & **X**iu's LSM	(Xiu & Pleim, 2001)
Noah	Joint Model of NCEP LSM and OSU LSM	(Ek *et al.*, 2003)
CABLE	**C**SIRO **A**tmosphere **B**iosphere **L**and **E**xchange	(Kowalczyk *et al.*, 2006)
CoLM	**Co**mmon **L**and **M**odel	(Dai *et al.*, 2003)
CLM3.5	**C**ommunity **L**and **M**odel Version **3.5**	(Oleson *et al.*, 2004)
JULES	**J**oint **U**K **L**and **E**nvironment **S**imulator	(Best *et al.*, 2011)
Noah-MP	**Noah** LSM with optional **M**ultiple **P**hysical scheme	(Niu *et al.*, 2011)

BONNER METEOROLOGISCHE ABHANDLUNGEN

Herausgegeben vom Meteorologischen Institut der Universität Bonn durch Prof. Dr. H. FLOHN (Hefte 1-25), Prof. Dr. M. HANTEL (Hefte 26-35), Prof. Dr. H.-D. SCHILLING (Hefte 36-39), Prof. Dr. H. KRAUS (Hefte 40-49), ab Heft 50 durch Prof. Dr. A. HENSE.

Heft 1-63: siehe `http://www.meteo.uni-bonn.de/bibliothek/bma`

64-77: open access, verfügbar unter `https://uni-bn.de/kpSDaQffe1`

Heft 64: ***Michael Weniger***: Stochastic parameterization: a rigorous approach to stochastic three-dimensional primitive equations, 2014, 148 S. + XV.

Heft 65: ***Andreas Röpnack***: Bayesian model verification: predictability of convective conditions based on EPS forecasts and observations, 2014, 152 S. + VI.

Heft 66: ***Thorsten Simon***: Statistical and Dynamical Downscaling of Numerical Climate Simulations: Enhancement and Evaluation for East Asia, 2014, 48 S. + VII. + Anhänge

Heft 67: ***Elham Rahmani***: The Effect of Climate Change on Wheat in Iran, 2014, [erschienen] 2015, 96 S. + XIII.

Heft 68: ***Pablo A. Saavedra Garfias***: Retrieval of Cloud and Rainwater from Ground-Based Passive Microwave Observations with the Multi-frequency Dual-polarized Radiometer ADMIRARI, 2014, [erschienen] 2015, 168 S. + XIII.

Heft 69: ***Christoph Bollmeyer***: A high-resolution regional reanalysis for Europe and Germany - Creation and Verification with a special focus on the moisture budget, 2015, 103 S. + IX.

Heft 70: ***A S M Mostaquimur Rahman***: Influence of subsurface hydrodynamics on the lower atmosphere at the catchment scale, 2015, 98 S. + XVI.

Heft 71: ***Sabrina Wahl***: Uncertainty in mesoscale numerical weather prediction: probabilistic forecasting of precipitation, 2015, 108 S.

Heft 72: ***Markus Übel***: Simulation of mesoscale patterns and diurnal variations of atmospheric CO_2 mixing ratios with the model system TerrSysMP-CO_2, 2015, [erschienen] 2016, 158 S. + II

Heft 73: ***Christian Bernardus Maria Weijenborg***: Characteristics of Potential Vorticity anomalies associated with mesoscale extremes in the extratropical troposphere, 2015, [erschienen] 2016, 151 S. + XI

Heft 74: ***Muhammad Kaleem***: A sensitivity study of decadal climate prediction to aerosol variability using ECHAM6-HAM (GCM), 2016, 98 S. + XII

Heft 75: ***Theresa Bick***: 3D Radar reflectivity assimilation with an ensemble Kalman filter on the convective scale, 2016, [erschienen] 2017, 96 S. + IX

Heft 76: ***Zied Ben Bouallegue***: Verification and post-processing of ensemble weather forecasts for renewable energy applications, 2017, 119 S.

Heft 77: ***Julia Lutz***: Improvements and application of the STatistical Analogue Resampling Scheme STARS, 2016, [erschienen] 2017, 103 S.

Heft 78: ***Benno Michael Thoma***: Palaeoclimate Reconstruction in the Levant and on the Balkans, 2016, [erschienen] 2017, XVI, 266 S.

Heft 79: ***Ieda Pscheidt***: Generating high resolution precipitation conditional on rainfall observations and satellite data, 2017, V, 173 S.

Heft 80: ***Tanja Zerenner***: Atmospheric downscaling using multi-objective genetic programming, 2016, [erschienen] 2017, X, 191 S.

Heft 81: ***Sophie Stolzenberger***: On the probabilistic evaluation of decadal and paleoclimate model predictions, 2017, IV, 122 S.

Heft 82: ***Insa Thiele-Eich***: Flooding in Dhaka, Bangladesh, and the challenge of climate change, 2017, V, 158 S.

Heft 83: ***Liselotte Bach***: Towards a probabilistic regional reanalysis for Europe, 2017 [erschienen] 2018, VI, 114 S.

Heft 84: ***Yen-Sen Lu***: Propagation of land surface model uncertainties in terrestrial system states, 2017, [erschienen] 2018, X, 120 S.

METEOROLOGISCHES INSTITUT
MATHEMATISCH NATURWISSENSCHAFTLICHE FAKULTÄT
UNIVERSITÄT BONN

Meteorologisches Institut
Universität Bonn